Fast Response of Boundary Layer Clouds to Climate Change

INAUGURAL-DISSERTATION

zur

Erlangung des Doktorgrades

der Mathematisch-Naturwissenschaftlichen Fakultät

der Universität zu Köln

vorgelegt von

Stephanie C. Reilly

aus

Westmeath

Irland

Köln 2020

Berichterstatter:

Prof. Dr. Roel A.J. Neggers
Prof. Dr. Susanne Crewell

Tag der letzten mündlichen Prüfung:

14 May 2020

"If you use your imagination,
you can see lots of things in the cloud formations."

-Charles M. Schulz

Contents

Abstract

Boundary layer clouds make up a large part of the total cloud cover across the world. These clouds play an important role in the vertical transport of heat, moisture, and momentum from the surface through the boundary layer. Thus these clouds have a significant impact on the vertical structure of the boundary layer. They not only have an impact on the vertical structure, but also have a significant impact on the Earth's radiation budget. Normally boundary layer clouds generally have a higher albedo compared to the surface below them and as a result there is an increased reflectance of solar radiation. Due to these strong impacts on the atmospheric conditions it is important that these boundary layer clouds and their processes are taken into account when simulating (future) climates.

One of the largest uncertainties in climate projections is related to the uncertainty in how boundary layer clouds respond to climate change. This uncertainty in cloud feedback is primarily related to the use of general circulation models (GCMs) in climate projections. As GCMs have a very coarse resolution they require parameterizations to represent boundary layer processes and clouds. These parameterizations are imperfect and therefore the GCMs have difficulties in representing the radiative effects of clouds. Therefore high resolution models such as large-eddy simulations (LESs), which require less parameterizations are used to study boundary layer processes and clouds.

Several LES studies have been conducted on climate projections, where a perturbation of a future climate is applied to the model. These perturbations include increases in sea surface temperature and/or the concentration of CO_2. In future climates it is anticipated that the atmosphere will become warmer and therefore it can contain a much larger concentration of moisture. This increased moisture can lead to the presence of very humid layers above the boundary layer, known as elevated moisture layers, which have already been observed in nature. This thesis investigates the response of boundary layer clouds to the presence of an elevated moisture layer, based on observed conditions during research flight 4 of the first Next Generation-aircraft Remote-sensing (NARVAL) campaign. This study is divided into three main sections. The first and second parts of the analysis focus on comparing the LES to observations recorded during the campaign in order to test the representativeness of the model. Following this the response of boundary layer clouds to an elevated moisture layer perturbation is investigated.

To this purpose, LESs are initially generated at the locations of the 11 dropsondes launched during the fourth research flight of the NARVAL campaign, which took place on December 14^{th} 2013. Initial comparisons indicate the LES shows good ability in representing the atmospheric conditions observed, showing a strong evolution of the boundary layer over time which has previously been observed at the Barbados Cloud Observatory. The results from the simulations also indicate that the LES has an ability to capture the height of the boundary layer inversion. There are some limitations in capturing the strength of the inversion, which is potentially related to the extremely dry conditions observed above the boundary layer.

The LES is then compared to retrievals from the High Altitude and Long Range Aircraft (HALO) Microwave Package (HAMP) instrument. In order to take the flight path into account the mean large-scale profiles, from the locations of 9 dropsondes, are used to derive a composite case. The aim of using the composite case was to investigate whether the LES has the ability to capture the large variability in the integrated water vapor and liquid water path retrieved throughout the flight path. Using a large domain LES, with horizontal extent reaching 51.2 km^2 the variability in integrated water vapor and liquid water path does approach the retrieved values, while domains with a smaller domains have a larger underestimation of the variability. The simulations indicate a correlation between the degree of organization, I_{org} and the precipitation flux, variability in integrated water vapor, and variability in liquid water path. A similar slope of dependency between the variability in integrated water vapor and I_{org} is found, across all simulations. In comparison the slopes of dependency between the I_{org} and both the variability in liquid water path and precipitation flux values differ between each of the simulations. This suggests that there are different structures in the clouds between simulations and that the I_{org} is highly controlled by the water vapor distribution.

These studies give confidence that the LES has the ability to capture observed conditions, which is important for simulating future climates. For the investigation into the impact of an elevated moisture layer and the corresponding response of the boundary layer clouds, two sets of simulations were generated on a 25.6 km^2 domain using the composite case setup from the HAMP comparison. These two sets of simulations include a control simulation and a set of 5 elevated moisture layer simulations with varying elevated moisture layer depth. While the elevated moisture layer has a significant impact on the atmospheric conditions in the free troposphere, while the largest impact in the boundary layer occurs in the cloud fraction. A decrease in the cloud layer depth is found with increasing elevated moisture layer depth. The impact is not however limited to the vertical structure of the clouds with a significant impact also found in the radiative fluxes throughout the lower troposphere. In order to determine the response of the boundary layer clouds to a change in climate, represented here by the elevated moisture layer, the cloud radiative effect is calculated at the top of the cloud layer. The results indicate there is a positive feedback from the boundary layer clouds produced in response to the elevated moisture layer, which indicates that these clouds have a warming effect on the boundary layer.

Zusammenfassung

Grenzschichtwolken machen einen großen Teil des Gesamtbedeckungsgrads auf der ganzen Welt aus. Diese Wolken spielen eine bedeutende Rolle beim vertikalen Transport von Wärme, Feuchtigkeits und Impuls von der Oberfläche durch die Grenzschicht. Somit haben diese Wolken einen signifikanten Einfluss auf die vertikale Struktur der Grenzschicht. Neben diesem Einfluss auf die vertikale Struktur, haben sie auch einen großen Einfluss auf das Strahlungsbudget der Erde. Üblicherweise haben Grenzschichtwolken eine höhere Albedo als die Erdberfläche darunter und infolgedessen ist das Reflexionsvermögen für Sonnenstrahlung erhöht. Aufgrund dieser starken Auswirkungen auf die atmosphärischen Bedingungen ist es wichtig, dass Grenzschichtwolken und dazugehörige Prozesse bei der Simulation (zukünftiger) Klimaszenarien berücksichtigt werden.

Eine der größten Unsicherheiten bei Klimaprojektionen hängt zusammen mit der Unsicherheit, wie Grenzschichtwolken auf den Klimawandel reagieren. Diese Unsicherheit bezüglich des Feedbacks von Wolken ist hauptsächlich mit der Verwendung allgemeiner Zirkulationsmodelle (GCMs) für Klimaprojektionen verbunden. Da GCMs eine sehr grobe Auflösung haben, erfordern sie Parametrisierungen, um Grenzschichtprozesse und Wolken darzustellen. Diese Parametrisierungen sind nicht perfekt, weshalb GCMs Schwierigkeiten haben die Strahlungseffekte von Wolken darzustellen. Daher benutzt man hochauflösende Modelle wie Large-Eddy-Simulationen (LESs), die weniger Parametrisierungen benötigen, um Grenzschichtprozesse und Wolken zu untersuchen.

Einige Untersuchungen zu Klimaprojektionen wurden mit LES Modellen durchgeführt, bei denen eine Störung auf das Modell zur Simulation eines möglichen zukünftigen Klimasaufgeprägt wird. Solche Störungen beinhalten eine Erhöhung der Meeresoberflächentemperatur und/oder der CO_2-Konzentration. Unter zukünftigen Klimabedingungen wird erwartet, dass die Atmosphäre wärmer ist und daher eine größere Menge Feuchtigkeit enthalten kann.

Diese erhöhte Feuchtigkeit kann zu sehr feuchter Schichten über der Grenzschicht führen, die als “elevated moisture layers” bekannt sind und in der Natur bereits beobachtet wurden. Diese Arbeit untersucht die Reaktion von Grenzschichtwolken auf das Vorhandensein einer “elevated moisture layer” basierend auf den beobachteten Bedingungen während des Forschungsfluges 4 der ersten NARVAL-Kampagne (Next Generation-Aircraft Remote Sensing). Diese Studie ist in drei Abschnitte unterteilt. Der erste und zweite Teil der Analyse konzentrieren sich auf den Vergleich des LES mit Beobachtungen, die während der Kampagne gewonnen wurden, um die Repräsentativität des Modells zu testen. Anschließend wird die Reaktion von Grenzschichtwolken auf eine Änderung des “elevated moisure layer” untersucht.

Zu diesem Zweck werden zunächst LESs an den Standorten der 11 Fallsonden generiert, die während des vierten Forschungsfluges der NARVAL-Kampagne gestartet wurden, welcher am 14. Dezember stattfand. Erste Ergebnisse zeigen, dass das LES die beobachteten atmosphärischen Bedingungen gut darstellt und ein starkes Anwachsen der Grenzschicht mit

der Zeit zeigt, die zuvor am Barbados Cloud Observatory beobachtet wurde. Die Ergebnisse der Simulationen deuten darauf hin, dass das LES die Höhe der Grenzschichtinversion erfassen kann. Einige Einschränkungen gibt es bei der Erfassung der Stärke der Inversion, was möglicherweise damit zusammenhängt, dass extrem trockene Bedingungen über der Grenzschicht beobachtet wurden.

Anschließend wird das LES mit Retrievals des HALO (High Altitude and Long Range Aircraft) Microwave Package (HAMP) verglichen. Um die Flugbahn zu berücksichtigen, werden die mittleren großräumigen Profile von den Positionen der 9 Fallsonden verwendet, um einen zusammengesetzten, repräsentation Fall. Das Ziel der Verwendung dieses Falls bestand darin, zu untersuchen, ob das LES in der Lage ist, die große Variabilität des integrierten Wasserdampf- und Flüssigwasserpfads zu erfassen, der über den Flugweg hinweg ermittelt wurde. Bei Verwendung eines LES mit einem großem Simulationsgebiet von einer horizontalen Ausdehnung von 51,2 km^2 nähert sich die Variabilität des integrierten Wasserdampf- und Flüssigwasserpfads den beobachteten Werten an, während bei kleineren Simulationsgebieten die Variabilität stärker unterschätzt wird. Die Simulationen zeigen eine Korrelation zwischen dem Organisationsgrad, I_{org}, und dem Niederschlagsfluss, der Variabilität des integrierten Wasserdampfs, sowie der Variabilität des Flüssigkeitswasserpfads. Die Steigung der Abhängigkeit zwischen der Variabilität des integrierten Wasserdampfs und I_{org} ist in allen Simulationen ähnlich groß. Hingegen unterscheiden sich die Steigungen der Abhängigkeit zwischen I_{org} und sowohl der Variabilität des Flüssigkeitswasserweges als auch der Niederschlagsflusswerte zwischen den einzelnen Simulationen. Dies deutet darauf hin, dass sich die Simulationen durch unterschiedliche Strukturen in den Wolken unterscheiden und dass I_{org} stark von der Wasserdampfverteilung gesteuert wird.

Diese Studien deuten darauf hin, dass das LES in der Lage ist, beobachtete Bedingungen zu erfassen, was für die Simulation zukünftiger Klimaszenarien relevant ist. Für die Untersuchung des Einflusses einer "elevated moisture layer" und der entsprechenden Reaktion der Grenzschichtwolken wurden zwei Ensemble von Simulationen mit einem 25,6 km^2 -Simulationsgebiets mit Verwendung des gleichen Fall-Setups wie bei dem HAMP-Vergleich erzeugt. Die beiden Simulationssätze umfassen eine Kontrollsimulation und 5 Simulationen mit einer "elevated moisture layer" bei variierender vertikaler Ausdehnung der Feuchtigkeitsschicht. Während das "elevated moisture layer" einen signifikanten Einfluss auf die atmosphärischen Bedingungen in der freien Troposphäre hat, tritt der größte Einfluss in der Grenzschicht in dem Wolkenanteil auf. Eine Abnahme der Dicke der Wolkenschicht wird mit zunehmender Ausdehnung die "elevated moisture layer" festgestellt. Der Einfluß ist jedoch nicht auf die vertikale Struktur der Wolken beschränkt, sondern es wird auch ein bedeutender Einfluß auf die Strahlungsflüsse in der gesamten unteren Troposphäre deutlich. Zur Bestimmung der Reaktion der Grenzschichtwolken auf ein verändertes Klima, welches hier durch die Schicht mit erhöhter Feuchtigkeit dargestellt wird, wird der Wolkenstrahlungseffekt am Oberrand der Wolkenschicht berechnet. Die Ergebnisse zeigen, dass es eine positive Rückkopplung durch die Grenzschichtwolken als Reaktion auf die "elevated moisture layer" gibt, was darauf hinweist, dass diese Wolken einen wärmenden Effekt auf die Grenzschicht haben.

Chapter 1

Introduction

1.1 Boundary Layer Clouds

Clouds play an important role in the atmospheric conditions across the world. They can have both a warming and a cooling effect on the atmosphere due to their response on incoming and outgoing radiation (Ackerman et al., 2009; Mitchell and Finnegan, 2009). Clouds cover almost two thirds of the Earth, in particular there tends to be more clouds over the ocean compared to over land. Clouds are usually categorized into three types: low level, mid-level, and high level clouds, depending on the altitude at which they persist.

This study focuses on the boundary layer region of the atmosphere. The atmospheric boundary layer is in the lowest level of the troposphere, and is therefore in direct contact with the surface. The clouds that form in this region, boundary layer clouds, are therefore

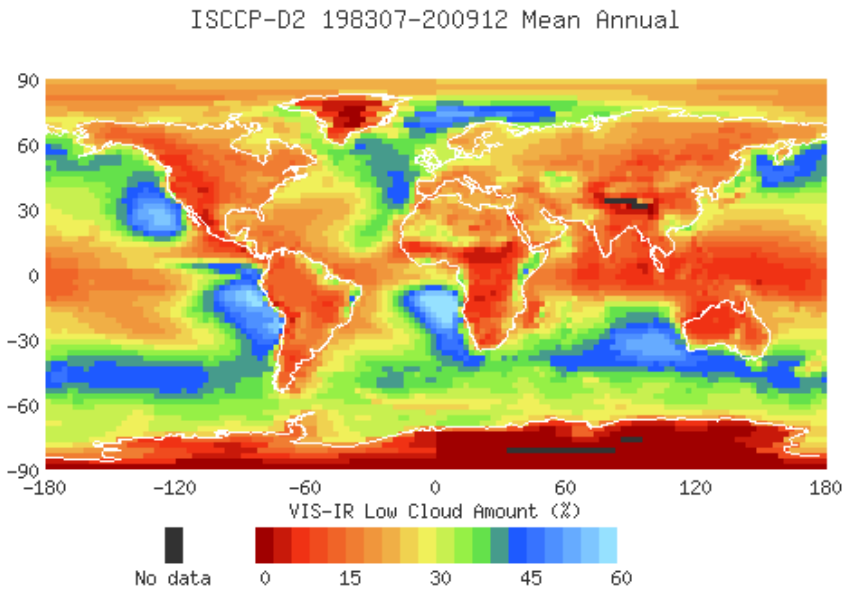

Figure 1.1: Mean low-level cloud cover from the International Satellite Cloud Climatology Project D2 Dataset, https://isccp.giss.nasa.gov/products/browsed2.html, downloaded on February 14, 2020, additional information on the development of the datasets can be found in (Rossow and Schiffer, 1999)

Figure 1.2: Stratus clouds that have developed in a mountainous region. Photo credit: Jan Chylík

Figure 1.3: A stratocumulus cloud, in the Arctic. Photo credit: Jan Chylík

classified as low level clouds. Boundary layer clouds make up a large portion of the cloud cover across the world, particularly over the ocean as shown in Fig. 1.1. Usually most low level clouds are made up of water droplets, but depending on the latitude and the temperature of the atmosphere where the cloud is present they can contain some ice crystals. Boundary layer clouds include stratus, stratocumulus, and cumulus clouds and are defined by their formation and horizontal extent.

Stratus clouds, known for their sheet like features, are usually either white or gray in color, and are found in stratified air. One feature in stratus clouds that separates them from stratocumulus and cumulus clouds is the fibrous cloud base, meaning that the exact altitude of cloud base can be difficult to define. Stratus clouds usually consist of water droplets, but on rare occasions can contain some ice crystals. In most cases these clouds do not precipitate, however under the right conditions it is possible that some drizzle is formed (American Meteorological Society, cited 2020a).

Similar to stratus clouds, stratocumulus clouds also very rarely produce precipitation. If

Figure 1.4: The detached and noticeable individual cumulus cloud, with the bright cloud top and a gray dark cloud base. Photo credit: Jan Chylík

precipitation is generated within the stratocumulus cloud it is usually in the form of drizzle. Stratocumulus are often easily confused with stratus clouds, primarily due to their large-scale horizontal extent. However, there are a several differences between the structures of these two clouds. Stratocumulus clouds are defined by their flat cloud tops and non fibrous cloud base, which means that the cloud base is easier to determine compared to a fibrous cloud, and they also have a distinctive variation in color, with some of the patches being white while others are gray. While stratus clouds are defined by their continuous cloud sheet, stratocumulus is seen to have patches of clear sky surrounded by cloud (American Meteorological Society, cited 2020b). Stratocumulus clouds are the most common low-level cloud types seen across the world, with the average cloud cover over the ocean, between 1954 and 2008, being 22 % and over land, between 1971 and 1996, being 12 % (Hahn and Warren, 2007; Eastman et al., 2011).

While shallow cumulus clouds are relatively similar in structure to stratocumulus clouds, in that they have non-fibrous cloud edges. Unlike stratocumulus clouds, shallow cumulus clouds have a relatively small horizontal extent. Shallow cumulus clouds are defined by their tower like structures, which on occasion can begin to take the shape of a cauliflower, with a bright white cloud top and a dark gray cloud base (Organization, 1975). Similar to stratus clouds, shallow cumulus clouds also have a diurnal cycle, which highly depends on whether the clouds are located above a land or ocean surface. Above land the maximum shallow cumulus cloud cover generally occurs in the afternoon, while over the ocean it generally occurs in early morning. Shallow cumulus clouds generally give an indication of fair weather conditions (American Meteorological Society, cited 2020c). Following stratocumulus clouds, shallow cumulus are one of the most common low-level cloud types occurring over the ocean, with an average cloud fraction of 13 % (Hahn and Warren, 2007; Eastman et al., 2011). They are particularly common in the trade-wind regions above the oceans (Joseph and Cahalan, 1990; Cuijpers and Duynkerke, 1993; Johnson et al., 1999; Bretherton et al., 2004; Siebert et al., 2013; Nuijens et al., 2014), e.g. off the west and northwest coasts of Barbados in the North Atlantic and off the coast of California in the Pacific.

1.2 Boundary Layer Clouds and Climate Change

Boundary layer clouds play an important role in the atmospheric conditions experienced. The vertical structure of the boundary layer is highly dependent on the processes resulting in the formation of these boundary layer clouds. For a convective boundary layer the heat, humidity, and momentum are transported rapidly from the surface to higher altitudes in the atmosphere (Tiedtke et al., 1988; Cess et al., 1995; Siebesma et al., 2003; Zhao and Austin, 2005; Markowski, 2007; Siebert et al., 2013; Albrecht et al., 2019). These convective conditions can result in the formation of some boundary layer clouds such as shallow cumulus clouds and stratocumulus clouds. The formation of these clouds can then further drive convective conditions. The convective transport causes in the boundary layer deepen and as a result has an impact on the large-scale conditions, including the climate of the region.

Cloud parameters, such as cloud cover, have a strong influence on not only the vertical structure of the boundary layer, but also on the Earth's radiation budget (Arking, 1991; Albrecht et al., 1995; Nuijens et al., 2014; Bony et al., 2015). This effect on the radiative budget by boundary layer clouds is referred to as the cloud radiative effect (CRE). Boundary layer clouds generally have a much higher albedo compared to the surface below them, this is particularly true for clouds over the oceans. Therefore the presence of boundary layer clouds can result in more solar radiation being reflected which reduces the amount of heat reaching the surface, which would have a cooling effect on the boundary layer. Depending on whether the boundary layer clouds are shallow or deep, longwave radiation emitted by the surface can either be transported through the cloud into the free atmosphere, which results in a cooling effect on the boundary layer, or it can absorbed and re-emitted back towards the surface (Schneider et al., 1978; Hartmann et al., 1992), which would result in a warming of the boundary layer.

The resulting impact of the clouds on the radiation budget causes a feedback loop, referred to as the cloud feedback, in which the change in the radiation budget then has a corresponding impact on the boundary layer clouds. With a change in climate there would be a change in the radiation budget and therefore a corresponding change in the boundary layer clouds. It is however uncertain how these clouds will respond to this change in the radiation budget.

In future climates, it is expected that the atmospheric conditions will change, temperatures are expected to rise and a potential increase in the moisture at higher altitudes. This leads to a change in the boundary layer clouds, and as a result a corresponding change in the cloud feedback. The change in the cloud feedback would indicate whether the clouds have a warming or cooling effect on the boundary layer. It is therefore important to be able to correctly simulate this cloud feedback in predictions of future climates.

1.3 Project Aims

General circulation models (GCMs) have been used to simulate climate predictions, however large uncertainties have been seen between GCM models simulations, with different models simulating various different potential future climates. One of the largest uncertainties in these climate predictions is related to the feedback of boundary layer clouds to a change in climate (Bony and Dufresne, 2005; Boucher et al., 2013; Vial et al., 2013; Blossey et al., 2016; Tan et al., 2016), in particular the feedback of marine boundary layer clouds. This uncertainty stems from the GCMs difficulty in simulating boundary layer clouds, due to the horizontal extent of the boundary layer clouds being smaller than the

resolution of a GCM domain. Therefore the GCMs require parameterization schemes in order to simulate boundary layer clouds. Over the years, high resolution models, such as large-eddy simulation (LES) models, have been used to simulate proxy future climate simulations in an effort to understand this cloud feedback Klein et al. (2017). In these cases perturbations of increases in CO_2 levels or sea surface temperatures have been used to gain an insight into how boundary layer clouds respond to a potential future climate.

This thesis investigates the possibility of using elevated moisture layers, which have already been observed in reality, as an additional method for studying how boundary layer clouds will respond to a change in climate, using an LES model. In order to investigate the response, it is first important to understand the model and to determine how accurate the LES model is at representing observed conditions, before generating a simulation with an elevated moisture layer. The results from these simulations will focused on answering the question:

How do boundary layer clouds respond to a change in climate, using an elevated moisture layer as a proxy for a potential future climate?

The thesis is made up of 7 chapters which are divided between background theory, and the analysis of the simulations, first focusing on determining the accuracy of the LES compared to observations, and then investigating the response of boundary layer clouds to an elevated moisture layer perturbation. Chapter 2 focuses on additional background theory of how boundary layer clouds form and their representation in observations and models. A detailed description of the observational campaign and model data used in the study is given in Chapter 3. Chapters 4 and 5 focus on comparing the LES model to the observational data, while Chapter 6 investigates the response of boundary layer clouds to the presence of an elevated moisture layer. Finally, the thesis concludes with Chapter 7 which includes the conclusions of the project and a future outlook.

Chapter 2

Boundary layer cloud formation and representation in observations and models

2.1 Formation of Boundary Layer Clouds

All clouds form when a parcel of air becomes saturated, which can occur as a result of increased moisture, decreasing temperature, or the introduction of mixing in the atmosphere, combined with available cloud condensation nuclei. As this air parcel rises through the boundary layer until it reaches its saturation level where it begins to cool and the water vapor begins to condensate onto cloud condensation nuclei, which consist of small aerosol particles (Seifert and Beheng, 2005). As the activated cloud droplets begin to grow they release latent heat. The manner in which these air parcels reach saturation differ between clouds, which in turn explains the general structure of the clouds seen in nature. Therefore the formation of a cloud is highly dependent on the atmospheric conditions in the region at the time of the cloud formation, which also include whether the boundary layer is in a stable or unstable state. Illustrative profiles of the mean virtual potential temperature for the cloud free stable boundary layer and an unstable boundary layer can be seen in Fig. 2.1a) and b) respectively.

Stratus clouds are layered clouds that primarily form due to moist air advecting over a slightly cooler surface in a stable boundary layer. A change in the orography of the surface or an advection of colder drier air below the moist air is required to lift the saturated layer forming a stratus cloud. This can occur particularly at coastal regions when warm moist air is advected over a cooler land surface which is at a higher altitude, or over a plain covered by fog. It is also possible for stratus clouds to form as a result of the dissipation of fog. Based on the close connection between stratus clouds and fog a diurnal cycle of the stratus clouds is seen, with a maximum cloud cover occurring late at night and into the early morning (American Meteorological Society, cited 2020a).

Straocumulus clouds, also a layered cloud, form through different mechanisms compared to stratus clouds. While it is possible for a stratocumulus clouds to be present in either stable and unstable atmospheric boundary layer conditions, they do require some convection to form. This convection can act in several ways to produce a stratocumulus cloud. One method is by the convective transformation of a stratus cloud layer, resulting in the stratus cloud layer breaking up and patches of clear sky forming between cloudy regions. A second method, by which stratocumulus clouds can form, is by the convective lifting of a parcel

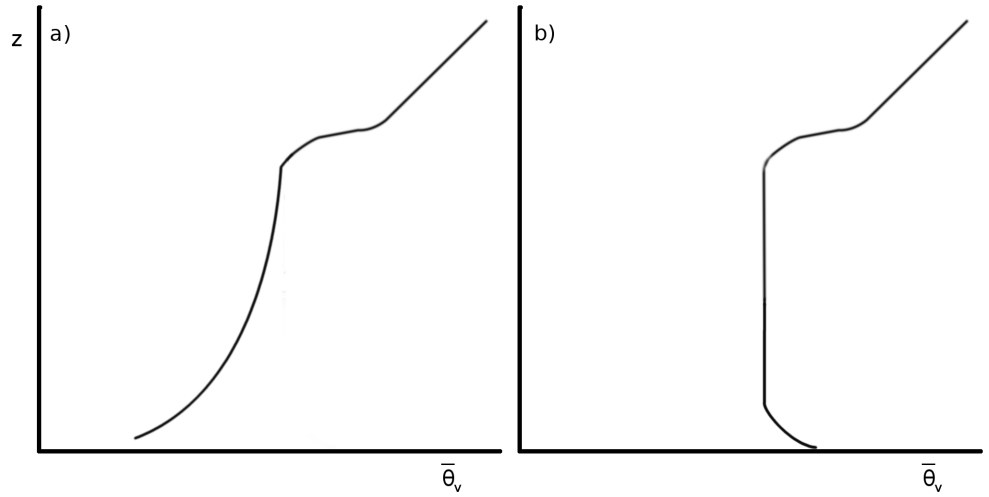

Figure 2.1: An illustration of the mean virtual potential temperature profiles in a a) stable and b) unstable atmospheric boundary layer.

of moist air through an unstable boundary layer. When this rising parcel of air reaches a strong inversion, the cloudy air continues moving in horizontal directions.

Similar to stratocumulus clouds, cumulus clouds also require convection to form. This means that the atmospheric boundary layer is in an unstable state. If the a parcel of air at the surface is moist and warm enough, and thus less dense than the air around it, the convection in the atmosphere can cause it to lift. As the parcel of air begins to rise and continues to rise throughout the boundary layer it has a positive buoyancy. This release of latent heat increases the buoyancy of the air parcel (Lohmann et al., 2016) beyond the buoyancy of the air above the inversion, which allows the cloud to continue forming and increasing in altitude.

2.2 Observations of Boundary Layer Clouds

For over 50 years there have been numerous campaigns conduced to study the atmospheric conditions over the ocean. The aims of each of the individual observational campaigns conduced have varied, for example investigating interactions between the ocean surface and the atmosphere (Davidson, 1968), or studying the initiation and impact of precipitation in marine shallow cumulus clouds (Rauber et al., 2007b). The method of obtaining the observational measurements also varied from campaign to campaign, with several campaigns employing the use of instruments onboard research ships (e.g. Augstein et al., 1973), buoys, or instruments onboard aircrafts (Rauber et al., 2007b). Two of the pioneering campaigns, the Atlantic Tradewind Experiment (ATEX) (Augstein et al., 1973) and the Barbados Oceanographic and Meteorological Experiment (BOMEX) (Nitta and Esbensen, 1974), took place in 1969 and were both primarily based in tbe North Atlantic trade-wind region, where boundary layer clouds are a common feature as indicated in Fig. 1.1.

The ATEX campaign, which took place in February 1969, was divided into two observational periods. Through the first period four research ships: Research Vessel Meteor, Research Vessel Planet, Research Vessel Discoverer, and the HMS Hydra, took part in the measurement campaign, while for the second period the HMS Hydra was not present. The three research vessels were positioned at the corners of an equilateral triangle and were

then allowed to drift along the flow of the trade winds. Throughout this period of observations there was very little precipitation present, with only one ship the Meteor observing a few showers of rain. The observations recorded during the ATEX campaign indicated that when the region has reduced convective activity and the trade-wind conditions are normally well developed a trade inversion develops which results in a separation between the divergent layer in the boundary layer and a convergent layer in the free troposphere (Augstein et al., 1973).

Several research ships took part in the BOMEX campaign, which was divided into four periods during May, June, and July of 1969. During this campaign a total of five research ships: the Rainier, Mount Mitchell, Discoverer, and the Oceanographer were positioned at the corners of a square separated by 500 km, with the Rockaway located at the center of the square (Davidson, 1968; Kuettner and Holland, 1969; Holland, 1970; Holland and Rasmusson, 1973; Nitta and Esbensen, 1974). The BOMEX was not limited to a research ships. An aircraft flew around the perimeter of the square defined by the locations of the research ships. The main study of the BOMEX campaign investigated the differences in the fluxes in momentum, heat, and water vapor between the ocean and the atmosphere (Holland, 1970). Based on results from the campaign it was indicated that the fluxes between the ocean and the atmosphere that were calculated, and the results of the subgrid-scale fluxes, could be of benefit in the development of eddy diffusion coefficients for models. Overall it is stated that this campaign was a success.

Following the success of these pioneering campaigns, several additional campaigns took place in years between then and now. From June to September in 1974 a large campaign covering ocean and land stations took place as part of the Global Atmospheric Research Programme (GARP), the GARP Atlantic Tropical Experiment (GATE). This campaign made use of up to 39 ship based sites and 13 research aircrafts which generally flew from near Dakar out over the ocean towards the ship based sites in the region (Mason, 1975). Studies based on this campaign included investigations into the fair weather boundary layer including boundary layer clouds (Nicholls and Lemone, 1980).

The focus on studying boundary layer clouds from observations continued with the international Atlantic Stratocumulus Transition Experiment (ASTEX) (Albrecht et al., 1995). The aim of the ASTEX campaign was to study and gain an understanding of the different processes that result in stratocumulus clouds transforming into a broken cloud. A second aim of the study was to investigate the processes that result in the formation of different types of clouds and the resulting cloud cover. It was aimed that the observations of these processes could lead to development of different parameterizations in models and also help with the development of the algorithms for satellites. The ASTEX campaign took place in June 1992 and was based off the coast of the Azores and Maderia Islands. A combination of measurements from aircrafts, ship, land based sites, and satellite were taken into account during the campaign. A vast dataset was obtained throughout the campaign, with approximately 600 soundings recorded during the campaign being assimilated into the ECMWF analyses data (Albrecht et al., 1995).

Since 2000, there has been an increase in the number of campaigns based in the tropical and subtropical trade wind regions. Between November 2004 and January 2005, the Rain in Shallow Cumulus over the Ocean (RICO) campaign was conducted off the coast of the Caribbean islands, primarily off the coast of Antigua and Barbuda. The primary reason for the development of the RICO campaign was to investigate atmospheric processes, based on observations, to study the initiation and development of precipitation. Observational measurements were recorded at four mobile sites: three research aircrafts and one research vessel, and one stationary site located at Spanish Point on the island of Barbuda. Each of the sites had several instruments in operation throughout the campaign. These instru-

Figure 2.2: The convective clouds observed at 16:29 UTC during research flight 4 of the first NARVAL campaign. Photo credit: Bjorn Stevens

ments included for example: several radar instruments recording at different wavelengths, radiosondes, lidars, cloud radars, and microwave radiometers. Additional information on the instruments and sites at which they were operated is given in Rauber et al. (2007a). The RICO campaign was largely a success in that a large dataset was compiled giving insight into the development and level of precipitation produced in cumulus clouds within the trade-wind region. The datasets of observations recorded during the RICO campaign also give a base line for the conditions expected from weather and cloud resolving models (Rauber et al., 2007b).

Following the RICO campaign a permanent cloud observatory was constructed on the island of Barbados, the Barbados Cloud Observatory (BCO). The BCO consists of numerous instruments including an sky imager, water vapor DIAL, lidar, radiometer, two cloud radar, and a standard meteorological station to name a few (Stevens et al., 2016). The observations recorded at the BCO have complemented the more recent field campaigns that have taken place since its construction, including the Clouds, Aerosol, Radiation and turbulence in the trade-wind regime over Barbados (CARRIBA) (Siebert et al., 2013), the two Next-generation Aircraft Remote-sensing for Validation (NARVAL) campaigns (Stevens et al., 2019a), and the ongoing Elucidating the role of clouds-circulation coupling in climate (EUREC^{4}A) campaign (Bony et al., 2017).

As the observational dataset taken in to account in this study is from one of the research flights conducted during the first NARVAL campaign, a detailed description is found in Section 3.1, where convective clouds such as the ones seen in Fig. 2.2 were observed. Following the success of the first NARVAL campaign, a second campaign was conducted during the wet season in August 2016. The High Altitude and Long-range research aircraft (HALO) was used as a remote-sensing platform in both NARVAL campaigns (Klepp et al., 2014; Stevens et al., 2019a). A large number of dropsondes were launched in a circle during two of the research flights in the second NARVAL campaign to test the potential for measuring the large-scale vertical velocity based on observations (Stevens et al., 2019a). A total of 10 research flights took place as part of the second NARVAL campaign.

The work done as part of both NARVAL campaigns has been the building block for the currently ongoing EUREC^{4}A campaign. The aims of the EUREC^{4}A campaign are to study trade-wind cumulus clouds in relation to the large-scale conditions and to develop

a dataset that could be used to compare future simulations of cumulus conditions. The main measurement platforms for the EUREC^{4}A campaign consist of 3 research aircrafts: the German HALO aircraft, the French ATR-42, and the British Twin Otter aircraft, and 3 research vessels: the Maria S. Merian, the Meteor, and the L'Atalante (EURECA, 2020). A corresponding campaign, the Atlantic Tradewind Ocean-Atmosphere Mesoscale Interaction Campaign (ATOMIC) (NOAA, 2020), from the National Oceanic and Atmospheric Administration (NOAA) is also being conducted as part of the EUREC^{4}A. As part of the ATOMIC campaign, a fourth aircraft, the WP-3D aircraft, and a fourth ship, the Ronald H. Brown, are added to the EUREC^{4}A campaign.

2.3 Modeling Boundary layer clouds

2.3.1 General Circulation Models

General circulation models (GCMs) allow for simulating the climate systems around the world, and in general can be useful for determining potential impacts as a result of climate change. Over the years there have been several GCMs developed with slightly different setups, however when predictions for future climate are generated a number of uncertainties into how the climate will change are seen. A large portion of these uncertainties have been associated with uncertainties in how boundary layer clouds will respond to a change in the climate (Bony and Dufresne, 2005; Boucher et al., 2013; Vial et al., 2013; Blossey et al., 2016; Tan et al., 2016, 2017). This is related not only to problems arising as boundary layer clouds, particularly shallow cumulus clouds, are generally only a fraction of the size compared to the dimension of the the GCM column, but there are also issues relating to the interactions and relationships between these clouds and the environment on a larger scale (Nuijens et al., 2014). As a result GCMs tend to have difficulties in representing and determining the radiative effects of these clouds (Nuijens et al., 2014), the vertical structure of the boundary layer particularly when boundary layer clouds are present, and the general cloud fraction within the domain (McGibbon and Bretherton, 2017).

In order to take the boundary layer conditions and in particular the presence of boundary layer clouds into account, GCMs require parameterizations and will continue to require them in the near future (Siebesma et al., 2003; Abel and Shipway, 2007). These parameterizations were designed in order to represent the effects on boundary layer clouds on a subgrid scale (Betts, 1986). These parameterizations are generally divided into two main topics: 1) understanding the transport of moisture, heat, and momentum using a vertical turbulent mixing parameterization, and 2) a cloud parameterization (Siebesma et al., 2003). These can be then further divided, with the vertical turbulent mixing parameterization being subdivided into an eddy diffusivity parameterization, a moist adjustment scheme, and a parameterization developed based on a mass flux scheme (Bretherton et al., 2004).

One of eddy diffusivity schemes, that is applied in numerous GCMs and some single-column models, is described by Tiedtke et al. (1988). In an eddy diffusivity scheme the sensible heat flux, the moisture turbulent flux, and the liquid cloud water are parameterized. This scheme takes into account the transport of the sensible heat and moisture, due to convection, within the cloud layer. Also within this particular scheme it is assumed that the eddy diffusivity coefficient is constant within an active cloud layer, while for passive cloud layers the eddy diffusion coefficient relies on the moisture distribution (Tiedtke et al., 1988).

A second common parameterization of the vertical transport in GCMs is the moist adjustment scheme approach. This parameterization is applied in an effort to reproduce the

moisture in the GCMs or large-scale models as realistically as possible. This method of parameterizing was proposed by Betts (1986) and then applied to datasets from a number of observational campaigns in Betts and Miller (1986). In this scheme the temperature and moisture structure is adjusted towards reference profiles determined by the large-scale advective processes and the large-scale radiative processes. The cloud top is determined using a moist adiabat profile throughout the lower levels of the atmosphere, and therefore defines whether it is a shallow or deep convective system. For a shallow convective system the condensation, and therefore the precipitation, when integrated throughout the cloud layer, are zero. Therefore for shallow convection it is set that there is no precipitation. For deep convection however the reference profiles are developed based on the total enthalpy.

Over the years there have been several different methods used to parameterize the liquid water in models and the cloud fraction in GCMs. Two methods of cloud parameterizations are a prognostic cloud scheme and a statistical cloud scheme. The prognostic scheme involves the inclusion of additional prognostic equations particularly for the cloud fraction and the liquid water. The statistical cloud scheme on the other hand is based on the potential to derive the values of the cloud fraction and liquid water. However this method only works if the subgrid scale values of the variability in both the temperature and the moisture are defined (Siebesma et al., 2003).

While the ability of parameterizations in GCMs have increased over the years, a number of weaknesses that contribute to the an uncertainty in climate prediction continue to exist (Bretherton, 2015). However there is hope that with the help of high resolution models, such as large-eddy simulation (LES) models, the understanding of the cloud effect can be expanded. While LES models do require some parameterization schemes, the variability on the subgrid scale is less complicated, as it is explicitly resolved. LES can also help with the developments and the evaluations of parameterization schemes that can be implemented into GCMs (e.g Siebesma and Holtslag, 1996; Siebesma et al., 2003; Neggers et al., 2009; Matheou et al., 2011).

2.3.2 Large-Eddy Simulation Models

Since their application to atmospheric research over 50 years ago, LES models have been a huge benefit in studying atmospheric processes, in particular boundary layer processes. LES models are on a level between direct numerical simulations and GCMs, which means the methods they use are in between direct simulations of the turbulent flow and the results of Reynolds-averaging equations (Piomelli, 1999). As their name suggests LES have the ability to explicitly model larger turbulent eddies, while the small eddies in the turbulent cascade require parameterizations (Mason, 1994). Even though LES models do contain some parameterizations the dependence on these parameterization is to a much lower extent when compared to large-scale models such as GCMs (Heus et al., 2010).

Over the years, there have been several developments adding to the representation of processes in the lower troposphere including for example cloud microphysics (Seifert and Beheng, 2005), radiation, and the treatment of the surface. A variety of LES models have been developed over the years, for example the University of California Los Angeles LES (UCLA-LES), the MetOffice large-eddy model (MetOffice LEM), the Icosahedral Nonhydrostatic LEM (ICON LEM), and the Dutch Atmospheric Large-Eddy Simulation (DALES) model. As DALES is used in this study a description of the model can be found in Chapter 3 Section 3.2.

LES models were initially used for gaining an understanding of the turbulent transport in the atmospheric boundary layer in studies by Lilly (1966), Deardorff (1972b) and Deardorff

(1972a). It was not long after these initial experiments, using LES models, that one of the first studies on a boundary layer with clouds was conducted by Sommeria (1976). For the study by Sommeria (1976) the model described in Deardorff (1972b) was used with slight modifications.

Ever since these pioneering studies of boundary layer clouds, there have been numerous studies on the different aspects of the boundary layer conditions (Beare et al., 2006a), including boundary layer cloud types (e.g Cuijpers and Duynkerke, 1993; Brown et al., 2002). The LES models ability to reproduce boundary layer clouds has been tested by generating simulations over locations where observations have been recorded. These observations are based on either stationary observational measurement sites, such as Cabauw in the Netherlands (Schalkwijk et al., 2015) and the Atmospheric Radiation Measurement Southern Great Plains (ARM SGP) site (Zhang et al., 2017), or based on observational field campaigns, such as BOMEX (e.g Siebesma and Cuijpers, 1995; Jiang and Cotton, 2000; Neggers et al., 2006) and RICO (vanZanten et al., 2011; Seifert and Heus, 2013). These comparisons have given confidence in the ability of LES in reproducing observed conditions, particularly with the developments on the microphysics schemes, which allow for the development of precipitation to be represented within the domain.

Intercomparison studies of LES models have been performed in order to compare different LES codes to each other and to observations, in order to determine the strengths and weaknesses of different LES codes in regards to representing observed conditions (Heus et al., 2010). There have been both large and small scale projects in this field. Some of the larger general projects include studies completed under the Global Energy and Water Cycle Experiment's (GEWEX's) Atmospheric Boundary Layer Study (GABLS) (Beare et al., 2006b) and the GEWEX Cloud System Study (GCSS) (Duynkerke et al., 1999, 2004; Stevens et al., 2001; Siebesma et al., 2003; vanZanten et al., 2011).

In recent years some of the focus of LES studies have been directed towards studying the feedback from boundary layer clouds due to perturbations in the climate. These studies are divided between intercomparison studies, such as the Cloud Feedback Model Intercomparison Project's (CFMIP) Global Atmospheric System Studies (GASS) Intercomparison of Large-Eddy and Single-Column Models (CGILS) (Blossey et al., 2013; Zhang et al., 2013; Blossey et al., 2016), and studies employing the use of a single LES model (e.g Xu et al., 2010; Rieck et al., 2012; Bretherton and Blossey, 2014). In each of these studies a perturbation is applied to a set of simulations. This perturbation is used to represent a potential future climate, e.g. an increased concentration of CO_2 or an increase in the sea surface temperature.

Chapter 3

Observation and model datasets

3.1 Observations from the NARVAL Campaign

The main observational dataset used in this study is from the first Next Generation Aircraft Remote-sensing for Validation (NARVAL) Campaign. The NARVAL Campaign made use of HALO, as an airborne remote-sensing platform. The main aim of the NARVAL Campaign was to investigate the shallow convection cloud structures and presence of clouds, like those seen in Fig. 2.2 and 3.1, and precipitation over two climate regimes in the North Atlantic, NARVAL South and NARVAL North. NARVAL South took place in December 2013 and was aimed at studying the trade wind regime in the North Atlantic, while NARVAL North took place in January 2014 and was aimed at studying winter mid-latitude storm-tracks. For both parts of the campaign, HALO was equipped with a specialized payload, including the microwave package, lidar, and the dropsonde system, along with several other instruments (Klepp et al., 2014). In the case of this study observations and retrievals from the dropsonde system and the HALO microwave package (HAMP) are used to determine the representativeness of the simulations. The measurements from the HAMP instrument and the additional instrumentation, such as the dropsonde system, made the overall NARVAL Campaign a success.

Figure 3.1: Convective clouds observed at 17:30 UTC during research flight 4 of the NARVAL campaign. Photo credit: Bjorn Stevens

3.1.1 Dropsondes

The dropsonde measurements add to the HAMP data to give an insight into the thermodynamic conditions in the atmosphere during each research flight in the campaign. The dropsondes developed by Vaisala were launched from HALO at intervals throughout the flight, recording measurements of temperature, wind-speed, latitudes, longitudes, pressure, and the relative humidity throughout the atmosphere. The dropsonde system on board HALO during the campaign were global positioning system (GPS) dropsondes that were based on a dropwindsonde system described in Hock and Franklin (1999). The accuracy of these dropsonde measurements were relatively high with the pressure measurements accurate to within 0.5 mb, the relative humidity measurements had an accuracy of around 2 %, and wind speeds with an accuracy of 0.5 m s^{-1} to 2.0 m s^{-1} (Hock and Franklin, 1999). Throughout the entire campaign a total of 121 dropsondes were launched (Klepp et al., 2014).

3.1.2 HAMP

HAMP consists of three modules and is nadir pointing radiometer located in the bellypod of HALO. These three modules are divided into HALO KV, HALO 11990, and HALO 189. HALO KV consists of two packages that are independent of each other for the K and V bands. HALO 11990 is also dived into two antennas independent of each other, a single detection retriever at 90 GHz and a signal heterodyne receiver which consisted of four channels ranging centered around the O_2 line at 118 GHz. Finally HALO 189 consisted of a single heterodyne which retrieved signals over the H_2O line centered on the 183 GHz line. Therefore in total, HAMP consists of 26 channels between 22 GHz and 195 GHz (Mech et al., 2014; Konow et al., 2018; Jacob et al., 2019). Using seven of the 26 HAMP channels, Jacob et al. (2019) was able to accurately retrieve values of IWV and LWP from the HAMP database.

3.1.3 Research Flights

A total of 13 research flights and two transfer flights were conducted over the North Atlantic during NARVAL. Eight of these research flights took place during NARVAL South and the remaining 5 research flights took place during NARVAL North. For NARVAL South four of the eight research flights were return trips between Oberpfaffenhofen in Germany and Barbados, while the other four research flights were local flights out of Barbados. In three of the four local flights, the aircraft traveled more than half way across the Atlantic.

In this study, the focus is on research flight 4 which took place during NARVAL South. While research flight 4 was a local flight, in that it left and returned to Barbados, it covered a large distance across the Atlantic. The flight track, shown in Fig. 3.2, shows that after leaving Barbados, HALO traveled approximately half way across the Atlantic to the location at which an overpass by CloudSat was performed. For this HALO turned and traveled south, before returning back to the original flight track and then back to Barbados. A total of 11 dropsondes were launched throughout the flight, the locations of which can be seen by the circles marked in Fig. 3.2.

During research flight 4, the large-scale thermodynamic conditions were generally homogeneous, with some variations occurring at the beginning and ending of the flight. In the area around the Caribbean Islands a relatively deep convective system was present, which produced precipitation, during the day. This convection also resulted in the presence of a large humid layer at elevated altitudes of around 8 - 10 km. This elevated layer dissipated

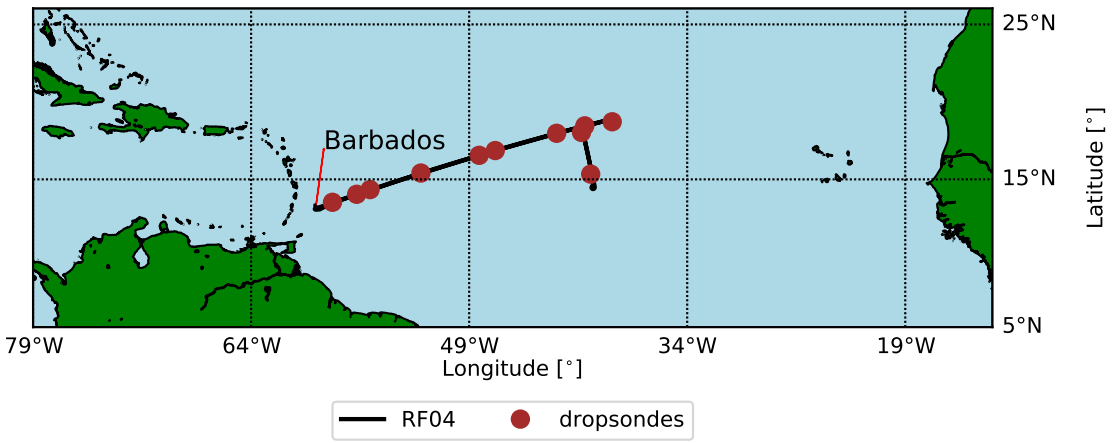

Figure 3.2: Flight track of research flight four, including the locations of each of the dropsondes that were launched throughout the flight. Modified version of the flight track to that seen in Klepp et al. (2014) and Reilly et al. (2019)

slightly as HALO traveled out across the Atlantic, where very dry conditions were observed above 2 km (Klepp et al., 2014). Upon returning to Barbados a deep convective system had developed resulting in an increase in the magnitude of the elevated humid layer and an increased depth of the boundary layer (Stevens et al., 2016).

3.2 The Dutch Atmospheric Large-Eddy Simulation Model (DALES)

This study makes use of the Dutch Atmospheric Large-Eddy Simulation (DALES) model. The code for the DALES model, previously known at the KNMI large eddy simulation model, that is currently used is based on the model used by Wyngaard and Brost (1984) and Nieuwstadt and Brost (1986). The governing equations in DALES can be based on either the Boussinesq approximation, where the reference state variables are set to equal the value of the variables at the surface, or an anelastic approximation. The DALES setup used in this study uses the Boussinesq approximation for the governing equations.

Over the years DALES has been involved in many intercomparison studies investigating the representativeness of LES compared to observed conditions. Some of these intercomparisons include simulations generated for observational campaigns such as the Atlantic Tradewide Experiment (ATEX) where DALES is referred to as the KNMI simulations (Stevens et al., 2001), and the Rain in Shallow Cumulus over the Ocean Campaign (RICO) (vanZanten et al., 2011). DALES is not however limited to intercomparison studies, it has also been used to study different atmospheric condition. These atmospheric conditions include convective boundary layers, which were first studied using DALES by Cuijpers and Duynkerke (1993).

Over the years since the study by Cuijpers and Duynkerke (1993), DALES has benefited from its open source platform. Having the open source platform for DALES allows users to download, modify and exchange information on the code, depending on the research topics. As a result of this DALES has been significantly modified since the study by Cuijpers and Duynkerke (1993). Some of these modifications are the inclusion of a number of schemes into the DALES setup, for example updated microphysics schemes and radiation schemes.

3.2.1 General Description of DALES

DALES requires at least three prognostic variables to be run, these are liquid water potential temperature (Θ_l), the velocity components, and the subgrid-scale turbulent kinetic energy (E) that are either calculated in the model or provided in the large-scale forcings. Additional prognostic variables such as total water specific humidity (q_t), rain droplet number concentration (N_r), and rain water specific humidity (q_r), along with additional scalars can also be included (Heus et al., 2010). Large-scale forcing could also be applied for each prognostic variable with the exception of E.

3.2.2 Setup of DALES

One file required for using DALES is the namoptions file, which contains the settings for the simulations including the length of the simulation, the domain size and the resolution of the horizontal and vertical grids. Within the namoptions file it is also possible to set how often the large-scale field is output as initialization profiles, which allows the model to be rerun beginning at different time-points throughout the simulation using the warmstart function. Using the warmstart function can be beneficial when running simulations with a large-domain and high resolution over a long time period, as it allows the simulation to be produced in smaller sections.

Forcing the LES back towards the large-scale state throughout the simulation, referred to nudging, can be applied to prevent drift in the model. This nudging, similar to the initialization and forcing of the LES, can be applied to either all prognostic variables, with the exception of E, that are provided by the large-scale variables, or individually specified prognostic variables. The nudging can also be applied over the entire profile or over a set range of altitudes. In order to switch nudging on in DALES, the ltestbed and ltb_nudge variables need to be set to true in the namoptions file. Following this the strength of the nudging (τ), referred to as tb_taunudge in the namoptions file, needs to be set to the length of time, in seconds, between the time-points at which DALES is nudged back to the large-scale reference state. The strength of the nudging is important, particularly when applying it to the entire profile, as when the nudging is too strong the turbulence in the boundary layer cannot develop. A detailed description of the nudging in DALES can be found in van Laar et al. (2019).

The DALES code uses a subgrid-scale scheme in order to determine the eddy diffusivity coefficients. Similar to the microphysics schemes, there are two main subgrid-scale schemes that can be employed by DALES. These subgrid-scale schemes are a subfilter-scale turbulent kinetic energy (SFS-TKE) (Deardorff, 1973) and the Smagorinsky schemes (Smagorinsky, 1963). There are some similarities and differences between the two subgrid-scale schemes in DALES. Both schemes use the three velocity component prognostic variables on a resolved case. There are however some differences between the two schemes. While both schemes take into account the velocity component prognostic variables, the SFS-TKE subgrid-scale scheme also includes an additional prognostic equation which results in storing the prognostic variable of the subgrid turbulent kinetic energy. The Smagorinsky scheme on the other hand, does not include this prognostic equation. The Smagorinsky scheme does use the Smagorinsky theory which takes into account the stability and viscosity of the air.

3.2.3 Microphysics Scheme

There are two main microphysics schemes that can be employed by DALES, both of which are the bulk microphysics scheme. A bulk microphysics scheme is defined as a scheme in

which the drop size distributions follow a theoretical probability distribution. The droplet size distribution is assumed to follow a prescribed probability density function. The exact size distribution in each cell is then specified by values of the main moments, such as the mean. The two possible bulk microphysics schemes in DALES are the Khairoutinov and Kogan scheme (Khairoutdinov and Kogan, 2000) and the Seifert and Beheng two moment microcphysics scheme (Seifert and Beheng, 2001). The formation of rain is dependent on the type of microphysics scheme used for the individual simulations.

The scheme by Khairoutdinov and Kogan (2000) was developed for representing marine stratocumulus clouds in LES models. It was constructed based on results from a fine bin microphysics simulation (Heus et al., 2010). Within this microphysics scheme a series of prognostic variables are defined based on a number of settings, for example the initialization of cloud droplets is influenced by the population of the cloud droplets. The droplet size is determined based on the the droplet concentration at specific liquid water content value.

While the Khairoutdinov and Kogan microphysics scheme is primarily used for stratocumulus cloud cases, the microphysics scheme by Seifert and Beheng (2001) and Seifert and Beheng (2005) is primarily for clouds which produce large amounts of precipitation. The microphysics scheme by Seifert and Beheng (2001) is developed by integrating the stochastic collection equation in order to determine the microphysical variables (Heus et al., 2010). This microphysics scheme calculates autoconversion and accretion rates as the cloud begins to develop, and are used to ensure that the transformation of cloud water into rain water is considered.

3.2.4 Radiation Scheme

DALES can be run using different radiation calculations depending on the aim of the study. The type of radiation calculation used is defined in the namoptions file before the simulation begins. There are five main radiation calculations currently used in DALES. These are no radiation calculations, a parameterized radiation calculation, a full radiation calculation, a rapid radiative model, and a user defined radiation calculation. Switching off the radiation calculation in DALES also results in the diurnal cycle in the simulation being switched off as it is driven by the radiation scheme. For the user defined radiation calculation, the user modifies one of the radiation fortran scripts before building the DALES code to be used in the simulation. The remaining radiation calculations, involves using two different radiation parameterization schemes, a longwave parameterization and a shortwave parameterization scheme.

The parameterization scheme for the longwave radiative transfer is the Global Energy and Water Cycle Experiment (GEWEX) Cloud System Study (GCSS) parameterization, which links the longwave radiative flux to the liquid water path. This is done using an analytic formula, which allows the simulation to be less computationally expensive (Larson et al., 2007). The shortwave radiative flux is calculated using the Delta-Eddington Model (Joseph et al., 1976). The Delta-Eddington Model calculates an asymmetrical phase function using a Dirac-delta function along side a two-term extension of a phase function (Joseph et al., 1976; Heus et al., 2010).

A rapid radiative transfer model has also been introduced to the DALES setup in recent years. This model also uses a Spectral Integration method, however it varies from the Monte Carlo Spectral Integration Model used by Pincus and Stevens (2009). Details of this rapid radiative transfer model are found in Mlawer et al. (1997). Finally, in the last 10 years, a fully interactive radiation scheme, the Monte Carlo Spectral Integration (Pincus and Stevens, 2009), has also been introduced into the DALES setup. This radiation model

is based on the k-distribution described in Fu and Liou (1992) and Fu et al. (1997). The benefit of the full radiation scheme is that the radiative flux is determined for every grid point at each time-step in the LES. This radiative flux is calculated by either a part of a waveband where the absorption coefficients are relatively similar, or by taking into account the full waveband that was randomly chosen. The use of the Monte Carlo Spectral Integration model for the full radiation scheme keeps computational costs reduced.

3.3 Large-scale Forcing Dataset

In order to run simulations using DALES, large-scale profiles are required. These profiles are used to initialize simulations and when required act as reference state profiles towards which the LES can be nudged. Large-scale forcings can be derived from GCM output, on the condition that they contain the prognostic variables required by the LES. Two examples of GCM data from which the large-scale profiles can be derived, are the Reanalysis and the Integrated Forecasting System (IFS) datasets from the European Center for Medium-range Weather Forecasts (ECMWF). The ECMWF Reanalysis dataset is a global dataset with information on the atmospheric conditions and surface conditions, and is produced as a result of running forecasting systems using observational data. The ECMWF IFS dataset on the other hand is forecast produced using an integrated computer software system. These datasets have been used in many studies over the years, with ECMWF Reanalysis being used by Neggers et al. (2006) and Blossey et al. (2013). The ECMWF IFS dataset has been also used in several recent studies, for example studies by Neggers et al. (2012), Dal Gesso and Neggers (2018) and van Laar et al. (2019).

This study makes use of large-scale forcing profiles derived from a ECMWF IFS dataset. These large-scale forcings, derived from the IFS dataset, are based on 12 hour datasets that are complemented by short-range weather forecasts. This provides large-scale profiles at a temporal resolution three hours. Having this temporal resolution of three hours, can be of benefit particularly when nudging is applied by the LES back towards the large-scale forcings. DALES takes the profiles of the atmospheric state variables, such as the total water specific humidity (q_t), the liquid water potential temperature (Θ_l) and the wind velocity components in the u and v direction, into account when initializing, forcing, and applying nudging.

The profiles of these atmospheric state variables are provided as averages over a 0.5 ° x 0.5 ° region around the area where the simulation is based. The vertical resolution of the derived large-scale forcing profiles is relatively coarse. With a vertical height of 70 km and a total of 91 vertical levels, the vertical resolution decreases with increasing altitude. This means that the region of the atmosphere with the highest resolution is within the boundary layer. A detailed description of the large-scale forcings, similar to those used throughout this study, is given by van Laar et al. (2019).

Throughout this study, datasets derived from the ECMWF IFS model are used to initialize DALES and are used as reference profiles towards which DALES is nudged either over the full atmospheric profile or over a range of altitudes above the boundary layer. Initially 11 large-scale forcing datasets where derived from ECMWF IFS output, for the regions around the locations of the 11 dropsondes launched during Research Flight 4 of NARVAL South. These datasets can be used to run individual simulations, as will be seen in Chapter 4, or run a composite case, as seen in Chapter 5 and Chapter 6.

3.4 Experimental Setup

Over the course of this study a number of different simulations with DALES have been generated. While they are different simulations there are a number of similarities between each of the them. All simulations, generated as part of this study, make use of the Seifert-Beheng bulk microphysics scheme and SFS-TKE subgrid scale scheme implemented in DALES. When the radiation in DALES is switched on, the fully interactive radiation scheme is used.

A summary of all the simulations generated throughout the project is given in Table 3.1. The elevated moisture layer simulations, referred to as EML Simulations in Table 3.1, cover the five elevated moisture layer simulations in total. This is done as to the only difference between the five simulations is the depth of the elevated moisture layer.

Table 3.1: Simulations generated throughout this project, with information on the different durations of the simulations, domain sizes, resolutions, radiation scheme,nudging strengths (τ), and nudging time windows (Δt).

Simulation Name	Run Length [hrs]	Domain Size [km^3]	Domain Resolution [m^3]	Scheme Radiation	Nudging Altitudes [km]	Nudging Variables	Nudging τ [hrs]	Nudging Δt [hrs]
Sim_Con (x11)	24	12.8x12.8x5.02	50x50x40	yes	0.0 - 5.02	q_t, Θ_l, u, v	3	6
Sim_DS (x11)	24	12.8x12.8x5.02	50x50x40	yes	0.0 - 5.02	q_t, Θ_l, u, v	3	6
Sim_Con/DS 1 hr	24	12.8x12.8x5.02	50x50x40	yes	0.0 - 5.02	q_t, Θ_l, u, v	1	6
Sim_Con/DS 2 hr	24	12.8x12.8x5.02	50x50x40	yes	0.0 - 5.02	q_t, Θ_l, u, v	2	6
Sim_Con/DS 4 hr	24	12.8x12.8x5.02	50x50x40	yes	0.0 - 5.02	q_t, Θ_l, u, v	4	6
Sim_Con/DS 5 hr	24	12.8x12.8x5.02	50x50x40	yes	0.0 - 5.02	q_t, Θ_l, u, v	5	6
Sim_Con/DS 6 hr	24	12.8x12.8x5.02	50x50x40	yes	0.0 - 5.02	q_t, Θ_l, u, v	6	6
Sim_DS Δt = 3 hr	24	12.8x12.8x5.02	50x50x40	yes	0.0 - 5.02	q_t, Θ_l, u, v	4	3
Sim_DS Δt = 12 hr	24	12.8x12.8x5.02	50x50x40	yes	0.0 - 5.02	q_t, Θ_l, u, v	5	12
Sim_DS 10 m	17	12.8x12.8x5.02	50x50x10	yes	0.0 - 5.02	q_t, Θ_l, u, v	4	6
Sim_DS 20 m	24	12.8x12.8x5.02	50x50x20	yes	0.0 - 5.02	q_t, Θ_l, u, v	5	6
NARVAL	48	51.2x51.2x5.02	100x100x40	yes	3.0 - 5.02	q_t, Θ_l, u, v	6	None
NARVAL Domain test 1	24	6.4x6.4x5.02	100x100x40	yes	3.0 - 5.02	q_t, Θ_l, u, v	6	None
NARVAL Domain test 2	24	12.8x12.8x5.02	100x100x40	yes	3.0 - 5.02	q_t, Θ_l, u, v	6	None
NARVAL Domain test 3	24	25.6x25.6x5.02	100x100x40	yes	3.0 - 5.02	q_t, Θ_l, u, v	6	None
NARVAL$_{norad}$	48	51.2x51.2x5.02	100x100x40	no	3.0 - 5.02	q_t, Θ_l, u, v	6	None
Control	24	25.6x25.6x7.02	100x100x40	yes	3.0 - 7.02	qt	1	None
EML Simulations	24	25.6x25.6x7.02	100x100x40	yes	3.0 - 7.02	qt	1	None

The differences between the simulations vary depending on the focus of the study and the testing different sensitivities of the LES, such as the impact of the domain size, resolution, or the strength of the nudging (τ). The length of the simulation duration is also varied in three simulations, where it is reduced to 17 hrs in the 10 m vertical resolution case to reduce computational costs, or increased to 48 hrs in the NARVAL simulations to limit the differences between the NARVAL simulation and a RICO simulation. The RICO simulation is performed using the University of California Los Angeles LES model (UCLA-LES) using an idealized setup on a 51.2 x 51.2 km^2 domain, described by Seifert and Heus (2013).

Chapter 4

Configuring LES based on dropsonde data in sparsely sampled areas in the subtropical Atlantic

This chapter is published as Stephanie Reilly, Roel Neggers, and Sara dal Gesso (2019) Configuring LES based on dropsonde data in sparsely sampled areas in the subtropical Atlantic, *Journal of Applied Meteorology and Climatology*, doi: 10.1175/jamc-d-19-0013.1

Abstract

This study explores the question of how field campaign data, gathered over a large area that is poorly sampled, can be used to make large-eddy simulation (LES) realizations more representative of the local conditions. To this purpose, dropsonde data recorded during the first Next-generation Aircraft Remote sensing for Validation Studies (NARVAL) South Campaign, in the marine subtropical North Atlantic, are blended into the forcing data. Control simulations are driven by time-dependent forcings derived from a combination of analyses and short-range weather forecasts, using weak nudging to prevent excessive model drift. A second set of simulations is driven by forcing data with dropsonde profiles included at the time-points of their release. Metrics are designed to i) quantify the impact on the boundary layer vertical profiles as a result of nudging towards the DS, and ii) use a probabilistic method to allow a fair comparison of the inversion strengths in the simulation and observation. The simulations show strong time-variation in the cloud layer depth on relatively short timescales, which is commensurate with recent observational studies in the area. Nudging towards dropsondes improves the representation of the atmospheric profiles throughout the depth of the boundary layer in all simulations. However, the impact on the inversion strength is less pronounced. All impacts persist for some time after the dropsonde time-point, depending on the intensity of the nudging and the nudging time-window. The sensitivity of the results to nudging details and vertical resolution is assessed.

4.1 Introduction

Subtropical marine trade-wind boundary layer (BL) clouds play a critical role in Earth's climate system given their strong impact on the vertical transport of heat, humidity, and momentum, and their significant impact on the radiative energy budget (Bony et al.,

2015). Uncertainties in predictions of future climate have been associated with poor representations of BL clouds in models through cloud-climate feedbacks that are still not fully understood (Bony and Dufresne, 2005; Tan et al., 2016; Blossey et al., 2016). A long-standing and continuing, scientific and practical, problem in atmospheric science is that BL clouds need to be parameterized in General Circulation Models (GCMs) (e.g Stocker, 2013).

High resolution models, such as Large-Eddy Simulation (LES) models, can be used to simulate BL clouds (Lilly, 1966; Deardorff, 1972a; Sommeria, 1976). The four-dimensional fields provided by LES give an insight into BL clouds and help improve their parameterization for GCMs. In an attempt to determine the strengths and weaknesses in LES models, many intercomparison studies have been carried out focusing on a variety of atmospheric conditions. Initially these intercomparison studies focused on stratocumulus clouds (e.g. Moeng et al., 1996; Duynkerke et al., 1999; Ackerman et al., 2009). More recent intercomparison studies have also included studying the representation of shallow cumulus cases (e.g. Brown et al., 2002; Siebesma et al., 2003; vanZanten et al., 2011). Studies over the past few years have focused on BL cloud responses to changes in climate (e.g. Bellon and Stevens, 2012; Rieck et al., 2012; Tan et al., 2016; Blossey et al., 2016).

While LES models have been shown to provide realistic realizations of BL cloud fields, the technique does have some well-known shortcomings. Those reported often include numerical and/or physical problems. Some examples include a lack of performance near strong inversions (e.g. Stevens et al., 1999; Gentine et al., 2015) or having a fully parameterized cloud microphysics scheme. A more practical difficulty is related to the configuration of LES experiments based on field campaign data (Stevens et al., 2001). Often such data is scarce over the oceans.

Recent field campaigns in the subtropical Atlantic, featuring state-of-the-art instrumentation, can provide observations that have the potential to fill this data gap. One example, the Rain In Cumulus over the Ocean (RICO) campaign (Rauber et al., 2007b) took place in 2004 and 2005 near Barbados. While RICO coincides geographically with the permanently operational Barbados Cloud Observatory (BCO) site, a more recent field campaign has taken place that was designed to start filling the data gap over the remote quarters of the subtropical Atlantic ocean. The Next-generation Aircraft Remote-sensing for Validation Studies (NARVAL) South campaign (Klepp et al., 2014) took place in December 2013 and featured the High Altitude and Long Range Research Aircraft (HALO) as its main instrument platform.

The NARVAL data complements the RICO/BCO dataset, by providing a more complete coverage of cumulus in the Trades. Most LES experiments of trade-wind cumulus have focused on the Barbados area (Siebesma et al., 2003; vanZanten et al., 2011; Seifert and Heus, 2013), with fewer experiments carried out for the upstream areas. There have been a few exceptions, for example Stevens et al. (2001). Unfortunately, the NARVAL dataset is much less extensive compared to the rich RICO/BCO datasets, with HALO only briefly present in areas of interest. This potentially complicates the ability to build an LES case. How to overcome this problem is an open research question and is applicable to all field campaigns similar to NARVAL. It is therefore scientifically attractive to build LES cases based on the dropsonde (DS) observations recorded during NARVAL.

This study aims to investigate the potential for using DS data, recorded during field campaigns, to make LES realizations more representative of the atmospheric conditions observed in the region. There is a focus on the BL deep structure in particular. In-situ DS data, as obtained during the NARVAL Campaign, is ideal for this study due to its relatively homogeneous large-scale conditions, in humidity and potential temperature, over a large area in the North-eastern Atlantic trade-wind subsidence regime. A second benefit

of using the NARVAL dataset are the additional cloud remote sensing datasets recorded with the HALO Microwave Package (HAMP), which complement the DS data.

Our main objective is to investigate to what extent it is possible to use limited DS data to build an LES realization that is realistic to a reasonable degree and subsequently useful for gaining insight into observed trade-wind cumulus cloud fields. To this purpose a total of 36 LES experiments were performed to coincide with dropsondes. These include a control series purely driven by the Integrated Forecasting System (IFS) data from the European Centre for Medium-Range Weather Forecasts (ECMWF), a second series in which DS data is merged in, and an additional series of sensitivity tests to investigate the impact of numerics and the nudging details.

The observations, LES model, and large-scale forcings used in this study are introduced in Section 4.2. Section 4.3 describes the general strategy, the setup of the model and the nudging, along with the details on the two main sets of simulations. The results are presented in Section 4.4, which documents the general behavior of the simulations while also investigating and quantifying the impact of including DSs in the nudging. The focus of the results lies on the BL deep structure and the inversion strength. In addition, the sensitivity to details in the nudging are assessed. Finally, Sections 4.5 and 4.6 summarizes the successes and shortcomings in the study followed by the main conclusions and outlook.

4.2 Observations and Models

4.2.1 NARVAL Campaign

The first NARVAL Campaign took place throughout December 2013 and January 2014, with HALO functioning as the main instrument platform. The campaign was divided into two parts: NARVAL-South, based off the coast of Barbados and focused on the North Atlantic trade-wind region, and NARVAL-North, based in Iceland and focused on the North Atlantic storm track (Klepp et al., 2014). This study focuses on NARVAL-South, which took place between December 10^{th} and December 22^{nd} 2013 and consisted of eight research flights. Four of these flights were transatlantic flights between Oberpfaffenhofen in Germany and Barbados. The four additional flights were local flights out of Barbados (Klepp et al., 2014; Schnitt et al., 2017).

The target area of NARVAL-South was the subtropical Atlantic trade-wind region, which in general is not routinely sampled by state-of-the-art meteorological instrumentation. The exception to this rule is the BCO on the island of Barbados (Stevens et al., 2016) and the Eastern North Atlantic (ENA) site (Lamer et al., 2015). Therefore, this campaign recorded important information on the atmospheric conditions in the North Atlantic trade-wind region.

Two observational datasets are used in this study. Vaisala DSs, which gathered in-situ measurements, and retrievals from HAMP. Over the course of the eight research flights, a total of 75 DSs were launched (Klepp et al., 2014; Schnitt et al., 2017). The DSs used during NARVAL-South contain a Global Positioning System (GPS), which was initially developed in the 1990's as a result of a collaboration between the National Center for Atmospheric Research (NCAR), the National Oceanic and Atmospheric Administration (NOAA), and the German Aerospace Research Establishment (DLR) (Hock and Franklin, 1999). These DSs record profiles for a variety of different atmospheric variables, including pressure with an accuracy of 0.5 mb, relative humidity (RH) with an accuracy of 2 %, specific humidity (q_v), potential temperature (Θ) and virtual potential temperature (Θ_v). The wind-speed in the West-East direction (u) and North-South direction (v) were recorded from the GPS

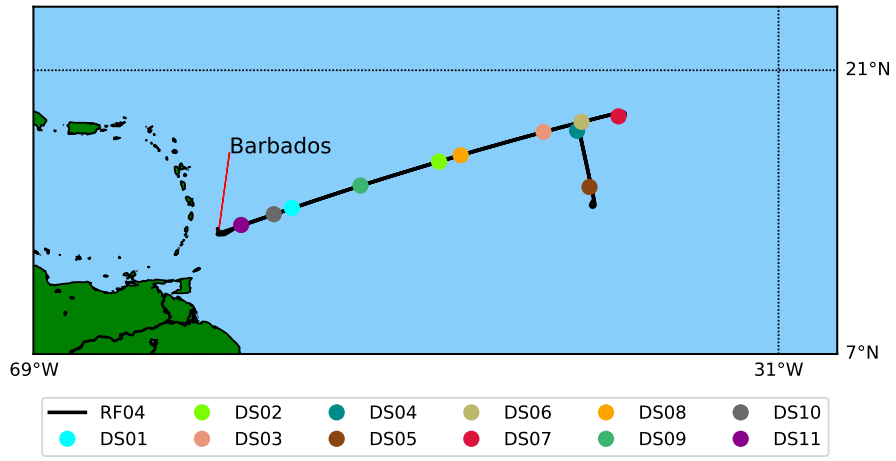

Figure 4.1: The locations of the 11 dropsondes (circles) launched during NARVAL South Campaign Research Flight 4 (RF04) are shown in different colors which will be used in profiles throughout in Figs. which contain more than 1 dropsonde per plot. RF04 traveled approximately 2000 km across the North Atlantic trade-wind region before returning to Barbados. The basis for the Fig. is credited to the NARVAL Campaign report by (Klepp et al., 2014)

system on the DS and have an accuracy of 0.5 - 2.0 m s^{-1}. The HAMP instrument is a microwave radiometer consisting of 26 channels between 22 GHz and 183.31 GHz (Mech et al., 2014; Konow et al., 2018; Jacob et al., 2019). The retrievals of Integrated Water Vapor (IWV) used in this study are obtained using the seven K-band channels along with the 90 GHz channel (Jacob et al., 2019).

This study focuses on Research Flight 4 (RF04), which took place on December 14^{th} 2013. RF04 left Barbados and flew approximately 2000 km across the North Atlantic before returning to Barbados. During this flight 11 DSs were launched, the details of which are given in Table 4.1. The flight path can be seen in Fig. 4.1, with the locations of each of the DS launched shown by the circles. RF04 was chosen due to the relatively steady state and uniform large-scale conditions (Stevens et al., 2016) and the presence of a well-defined convective BL including persistent fair-weather cumulus.

Table 4.1: Location and Time of the Dropsonde (DS) launches.

Simulation/DS	DS01	DS02	DS03	DS04	DS05	DS06	DS07	DS08	DS09	DS10	DS11
Launch Time (UTC)	14:08	15:04	15:46	16:00	16:22	17:06	17:24	18:27	19:09	19:47	20:01
Lat (°N)	14.3	16.6	18.0	18.1	15.4	18.4	18.8	16.9	15.4	14.0	13.5
Lon (°E)	304.2	311.7	317.0	318.7	319.4	319.0	320.8	312.8	307.7	303.3	301.6

In order understand the atmospheric conditions observed by the DSs the recorded profiles of Θ_v, q_v, and RH are shown in Fig. 4.2. Within the BL there is some variation in the profiles for Θ_v. However, all DSs record Θ_v within a 5 K range at the surface. The BL for each of the Θ_v profiles is capped by an inversion which occurs between 1.5 km and 2.5 km for nearly all DSs. Further aloft, the variation among the Θ_v profiles is much less pronounced. The lapse rate above the BL indicates relatively stable atmospheric conditions. The profiles of q_v and RH, shown in Figs. 4.2b) and c) respectively, are more variable in the BL compared to the Θ_v profiles. This is emphasized in the region of the capping inversion at the top of the BL.

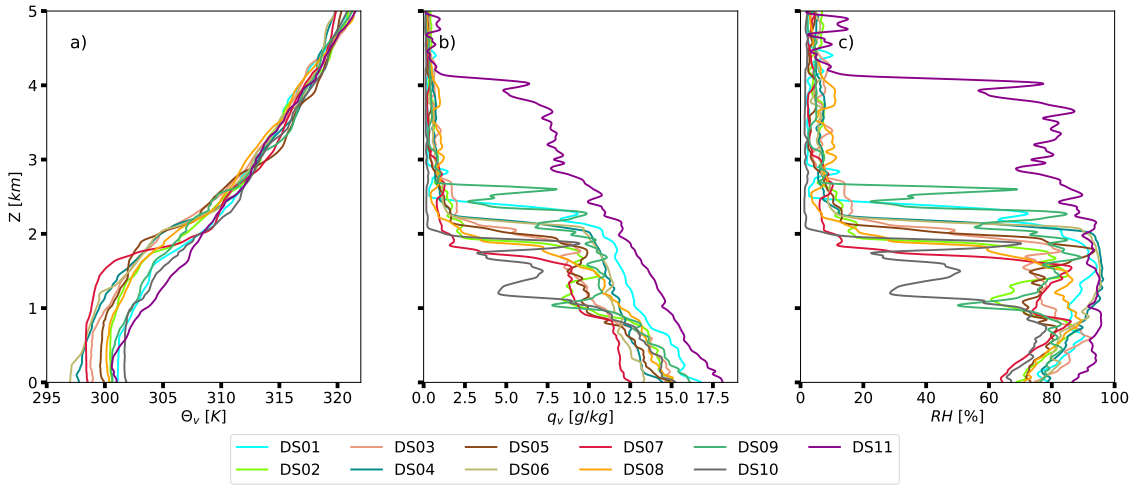

Figure 4.2: Profiles for a) virtual potential temperature (Θ_v), b) specific humidity (q_v) and c) relative humidity (RH) with respect to altitude, recorded for each of the dropsondes launched during RF04

For the individual DS profiles, the capping inversions are more pronounced in the humidity profiles compared to those in the Θ_v profiles. While the BL capping inversion in the Θ_v profiles occur at relatively similar altitudes for each DS, this is not the case in the humidity profiles. The capping inversions in the humidity profiles for predominantly occur between 0.7 km and 1.7 km. One outlying profile, DS11, has a capping inversion at approximately 4 km. This DS recorded a region of deep convection, which was also noted by Stevens et al. (2016).

One common trait between each of the DS humidity profiles is the extremely dry conditions above the BL, also observed by Stevens et al. (2016). The dry conditions can be seen in Fig. 4.2b) and c), where there appears to be little to no humidity present above the inversion.

4.2.2 LES Model

The Dutch Atmospheric Large Eddy Simulation (DALES) model, formerly known as the KNMI LES model, was used to run LESs over the locations of the DS launches. For the simulations in this study, DALES was run using the kappa scalar advection scheme recommended in Hundsdorfer et al. (1995) and also described in Heus et al. (2010). DALES can be run with either a two-moment microphysics scheme which is based on the Seifert Beheng scheme (Seifert and Beheng, 2005) or a scheme by Khairoutdinov and Kogan (2000). Similarly, there are two main sub-grid scale schemes in DALES, the sub-filter scale turbulence kinetic energy scheme and a Smagorinsky sub-filter scheme. Downward radiation at the top of the model is calculated using the GCM profiles above the model ceiling.

DALES has been successfully used to simulate trade-wind cumulus for scientific research, and has shown satisfactory skill in reproducing key features of this cloud regime based on various intercomparison studies such as BOMEX (Siebesma et al., 2003), RICO (vanZanten et al., 2011), ATEX (Stevens et al., 2001), transition cases (van der Dussen et al., 2013; Neggers et al., 2017) and continental cumulus (Brown et al., 2002). The DALES code allows continuous nudging of liquid water potential temperature (Θ_l), the total water mixing ratio (q_t), and u and v throughout the simulation. For a detailed description of the DALES model, including details on the schemes and processes included in the model we refer to

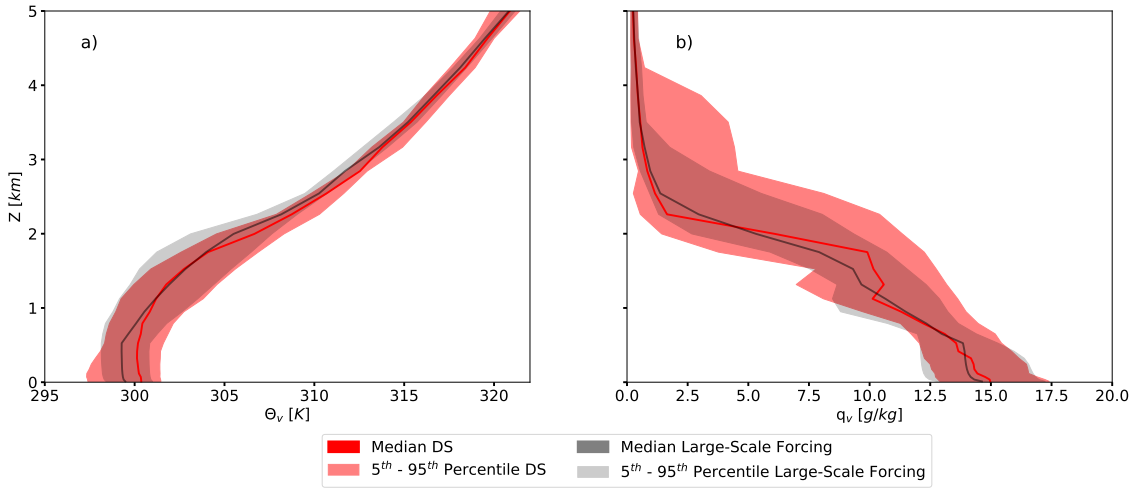

Figure 4.3: The profiles of a) virtual potential temperature (Θ_v), and b) specific humidity (q_v) for an ensemble of a) all the DS profiles (red) and all Integrate Forecasting System (IFS) data (gray) for the Sim_Con simulations. Solid lines represent the median profiles while the shaded region represents the area between the 5^{th} and 95^{th} percentiles of the ensembles.

Heus et al. (2010). DALES is an open access code which and is available to download from the DALES team on GitHub at https://github.com/dalesteam.

4.2.3 GCM Dataset

The method of using GCM data, from ECMWF, to derive the large-scale forcings for DALES has been previously used by Dal Gesso and Neggers (2018) and more recently by van Laar et al. (2019). We refer to the latter study for a detailed description of the forcing data and method. These large-scale forcings, from IFS weather analyses, are based on an average over a 0.5x0.5 degree domain centered over the DS location. The vertical resolution of the IFS dataset consists of 91 pressure levels with a high vertical resolution at the surface and a coarser resolution near the ceiling of the dataset. 12 hourly data from weather analyses is combined with short-range three-hourly forecasts, to fill up the time-points in between. This yields a continuous forcings dataset at a temporal-resolution of 3 hrs. IFS data from ECMWF has also been used in various other recent LES studies for calculating the large-scale forcings (e.g. Gustafson et al., 2017).

To investigate the difference between the IFS dataset at the time of each DS launch, the ensemble-mean profile for Θ_v and q_v across all IFS datasets is compared to the ensemble-mean DS profile across all DSs. Figure 4.3 shows the ensemble-mean Θ_v and q_v profiles for all DSs and IFS profiles. The median value of both ensembles at each altitude is represented by the solid line while the shaded region indicates the area between the 5^{th} and 95^{th} percentile. It should be noted that the median IFS Θ_v and q_v profiles are colder and drier at the surface. This indicates that the IFS slightly underestimates the temperature and humidity in the lowest layers of the BL. While there is a slightly greater variability in the DS profiles near the surface, in general the IFS is able to capture the basic observed thermodynamic structure of the trade-wind BL.

To gain more insight into the atmospheric conditions represented in the IFS dataset, the pressure velocity (ω) profiles are studied at the DS launch times, shown in Fig. 4.4. Figure 4.4a) indicates that there is large variation in the magnitude and vertical structure of ω

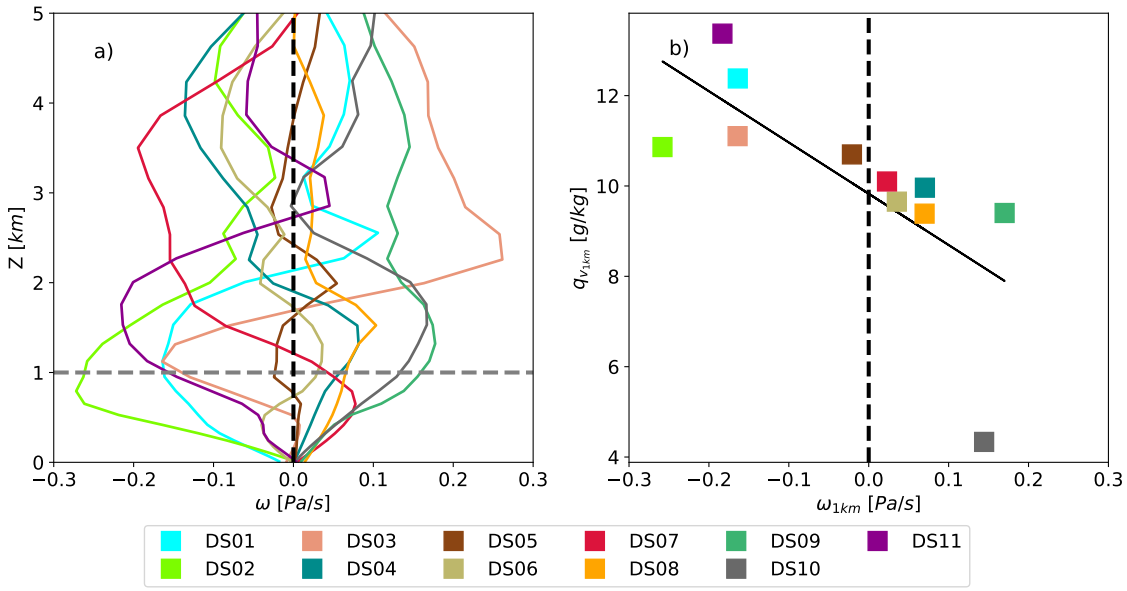

Figure 4.4: The IFS pressure velocity a) profiles (ω) for each DS location and time, with respect to altitude, and b) value at 1 km compared to the corresponding IFS q_v value at 1 km.

within the sampled area. From Fig. 4.4a) a relatively linear change is seen in ω within the lowest 1 km of the atmosphere. Therefore, the value of ω at 1 km for each DS time is compared to the corresponding IFS q_v value at 1 km, shown in Fig 4.4b). The large-scale convergence ($\omega < 0$), expressed by large-scale ascent, tends to be associated with higher low-level humidity, while large-scale divergence ($\omega > 0$), as expressed by descent, is associated with drier conditions. The expected association between ascent and high humidity values, and between descent and drier conditions is confirmed by the linear fit line in Fig. 4.4b).

4.3 Experimental Configuration

4.3.1 General Strategy

The novel approach used in this study is to directly blend the DS profiles into the forcing data as derived from a GCM in order to nudge the LES toward observed profiles. Simulations are then generated at the location of each DS launch. The aim is to investigate and understand the subsequent impact on the thermodynamic state in the LES near the time-point of the DS. There is a particular focus on the representation of the BL deep structure and the trade-wind inversion. Methods to fairly and optimally compare the observed inversion as derived from the point-sampled DS profiles to that of the three-dimensional LES domain are explored. The associated impact on clouds will be briefly documented, but their detailed analysis and evaluation against HALO data is for now considered an ongoing research topic.

4.3.2 DALES Setup

This study utilizes time-dependent large-scale forcing, including the application of prescribed advective tendencies and prescribed large-scale subsidence. Large-scale horizontal

advection is prescribed for all prognostic variables. The large-scale vertical advection tendency is interactive with model profiles by using prescribed subsidence. For wind, the geostrophic forcing is derived from the large-scale pressure field. The lower boundary conditions for these simulations include prescribed sea-surface temperature (SST), roughness length and interactive fluxes. The simulations are generated with an interactive radiation scheme and warm Seifert Beheng two moment bulk microphysics scheme (Seifert and Beheng, 2005).

Continuous nudging is applied towards a reference state at a slow, synoptic timescale of 3 hrs. The nudging in these simulations is applied in an effort to reduce the drift in the LES and involves nudging the simulation towards the large-scale forcing profiles in the IFS dataset. The nudging tendency towards the reference state is carried out using the following equation:

$$\left.\frac{\Delta\overline{\phi}}{\Delta t}\right|_{nudged(x,y,z)} = \frac{\overline{\phi}_n(z) - \overline{\phi}(z)}{\tau} \tag{4.1}$$

where Δt is the time between each of the large-scale forcings time-steps, and $\overline{\phi}_n(z)$ is the reference profile towards which the LES profile $\overline{\phi}(z)$ is nudged. The nudging tendency is the same for every grid cell, with $\overline{\phi}(z)$ linearly interpolated between the IFS time-steps. The nudging timescale is represented as τ, where large values of τ indicate weak nudging and small values of τ indicate tight nudging. The value of τ in this study is set to 3 hrs, which allows the simulation to take the large-scale data into account while also allowing the turbulence in the simulation to act freely. This method was demonstrated by Neggers et al. (2012) at the location of a permanent supersite, and more recently by van Laar et al. (2019).

The simulations are generated on a domain that was fixed in space (Eulerian) at each DS location. The domain size used in this study is 12.8 x 12.8 x 5.04 km^3 with a resolution of 50 x 50 x 40 m^3. The general details of resolution and nudging timescale for the two main sets of simulations are summarized in Table 4.2.

Table 4.2: Setup of simulations generated with the simulations analyzed in the initial experiments highlighted in bold.

Parameter		Value					
τ (hr)	Sim_Con	1	2	**3**	4	5	6
	Sim_DS	1	2	**3**	4	5	6
T (hr)	Sim_DS	3	**6**	12			
Δz (m)	Sim_DS	10	20	**40**			

4.3.3 Overview of Simulations

4.3.3.1 Control Simulations

A set of 11 control simulations were generated, referred to as *Sim_Con*, and were nudged toward the pure IFS state. The time-series of the pure IFS state is visualized in Fig. 4.5a) as a timeline of atmospheric states where the blue circles indicate an individual time-step (t) in the IFS dataset. Each time-step t, in Fig. 4.5, contains the large-scale forcing profiles required by the LES. The subscripts k represent where each specific t is in relation to the time of the DS launch, where t_k is the time-step directly before the time-point of the DS launch. The time difference between each t is exactly 3 hrs.

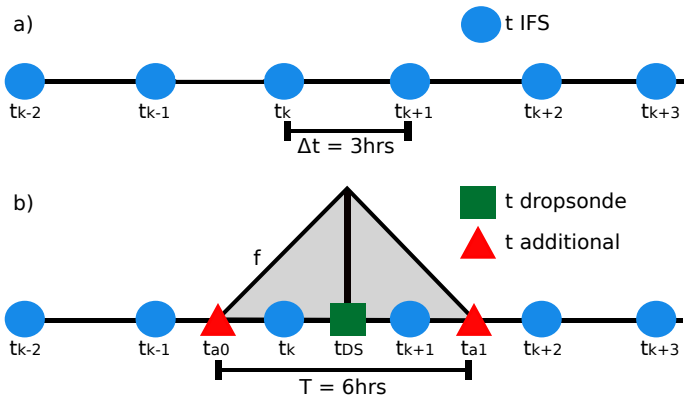

Figure 4.5: Schematic of the time-series of the Integrated Forcing System (IFS), from ECMWF, with each time-step (t, blue circle) contains the large-scale atmospheric profiles at that location and time of day for a) Sim_Con, while b) Sim_DS also includes the DS profiles, on the IFS vertical grid, at the DS launch time (green square, t_{DS}) and two additional time-steps (red triangles, t_{a0} and t_{a1} which are located 3 hrs before and after the DS launch time. These two additional time-steps allow for a gradual nudging towards the DS profile, and are created by linearly interpolating the atmospheric profiles from the adjacent IFS time-steps.

Each Sim_Con was initialized at 00:00 UTC and run for 24 hrs. The nudging is implemented in the Sim_Con cases in order to reduce as many differences as possible between the different simulations carried out in this study.

4.3.3.2 Dropsonde Simulations

The second tier of 11 simulations, referred to as *Sim_DS*, has a similar setup to the Sim_Con. The main difference between the setup of the Sim_DS and the Sim_Con is that the DS profile is inserted into the IFS dataset at the time-point of the DS launch. To effectively blend the DS profile into the IFS nudging dataset the following procedure, made up of three steps, is designed.

First, at the exact time-point of the DS launch, a new time-step is created in the IFS time-series, t_{DS}. This time-step is indicated by the green square in Fig. 4.5b). To calculate the radiation, the DS profiles are used below the flight altitude of HALO while the IFS profiles are used above this altitude. The second step is then to define two new time-steps, 3 hrs before and after t_{DS}. This creates a nudging time-window ($T = t_{a1} - t_{a0}$) of 6 hrs. At these two new time-steps, represented by the red triangles in Fig. 4.5b), the values from the atmospheric profiles at the two adjacent IFS time-steps are linearly interpolated onto t_{a0} and t_{a1}.

The final step is then to adjust each of the profiles at time-steps t_k and t_{k+1}. The closer time-step t_k or t_{k+1} is to t_{DS}, the more it resembles the DS state. This is achieved by using a gradual changing weight, f:

$$f = \begin{cases} \left| \dfrac{t_{a0} - t_k}{t_{a0} - t_{DS}} \right| & \text{for} \quad t_k < t_{DS} \\ \left| \dfrac{t_{a1} - t_k}{t_{a1} - t_{DS}} \right| & \text{for} \quad t_k \geq t_{DS} \end{cases} \tag{4.2}$$

$$\overline{\phi}^{\star}_{t_k} = \overline{\phi}(t_k) \cdot (1 - f) + \overline{\phi}(t_{DS}) \cdot f \tag{4.3}$$

where $\overline{\phi}(t_{DS})$ is the DS profile on the IFS vertical grid as a domain-average profile, and $\overline{\phi}(t_k)$ is original domain-average profile at time-step t_k. As illustrated by Fig. 4.5b), to adjust the profile at the time-step t_k, situated directly before the t_{DS}, f is calculated using Eq. 4.2. Using f, the new profile ($\overline{\phi}^{\star}_t$) at time-step t_k is calculated using Eq. 4.3.

Summarizing, the new time-series contains three new time-steps, together defining a nudging time-window in which the reference state for nudging is modified to reflect the atmospheric state observed by the DS. The addition of the new time-steps t_{a0} and t_{a1} in the sequence ensures that the impact of the DS is not felt before the simulation enters the time-window. This also ensures that the differences in the proximity of t_{DS} to the adjacent IFS time-steps do not affect the nudging.

4.4 Model Results

4.4.1 Results for all Sim_Con cases

Previous studies, such as Nuijens et al. (2014) at the BCO and Lamer et al. (2015) at the ENA site, have reported observations of strong temporal-evolutions of the BL in the trade-wind region. To assess if this is also seen in simulations for the NARVAL campaign, the time-height contour plots of RH, including the evolution of the cloud layer, for all 11 Sim_Con are shown in Fig. 4.6. All simulations contain clouds, but differ considerably. Indeed, all simulations show time-variation on a short timescale. We speculate that this variation is introduced by time-varying forcings. The cloud base (Z_{CB}) is defined as the lowest level at which the cloud fraction (CF) is greater than 0.001 %, while cloud top (Z_{CT}) is defined as the level above which the CF is less than 0.001 % . The results from Fig. 4.6 indicate that i) the LES is able to reproduce the strong temporal-evolution of the BL, and that ii) this behavior that Nuijens et al. (2014) observed is not unique to the BCO.

As the simulations in Sim_DS are directly forced towards the DS profiles, it is beneficial to compare the simulations to an independent set of measurements to investigate their representativeness of local conditions. To this purpose, a time-series of integrated water vapor (IWV) was retrieved by HAMP. The median IWV retrieval, calculated over a 1 hr window around each DS launch time, is compared to the IWV for the domain-averaged profile at t_{DS}. From Fig. 4.7 it is shown that the LES is able to capture IWV values similar to the observed values. This comparison indicates that the LES is capable of representing the atmospheric conditions observed over the flight path. It should be noted that DS11 is not included in this comparison as the aircraft landed less than half an hour after DS11 was launched and therefore there is not enough data to have a consistent comparison.

4.4.2 DS01 Results

To understand the impact of nudging the LES towards the DS, in particular on the BL and its clouds, we focus on a single experiment. This experiment corresponds to the temporal and spatial region of the first dropsonde, DS01. First, a visual indication for both simulations is shown in Fig. 4.8. These visualizations give an instantaneous look at the impact of including the DS profile into the LES setup. To quantify the difference the CF and liquid water path (LWP) for the domain at that time-point were calculated. There is a difference of 21.8 % in CF and of 0.03 kg m^{-2} in LWP between the simulations.

One aim of this study is to investigate the impact on the BL structure by nudging the LES towards the DS profile. To this purpose the DS profiles for potential temperature (Θ), q_v,

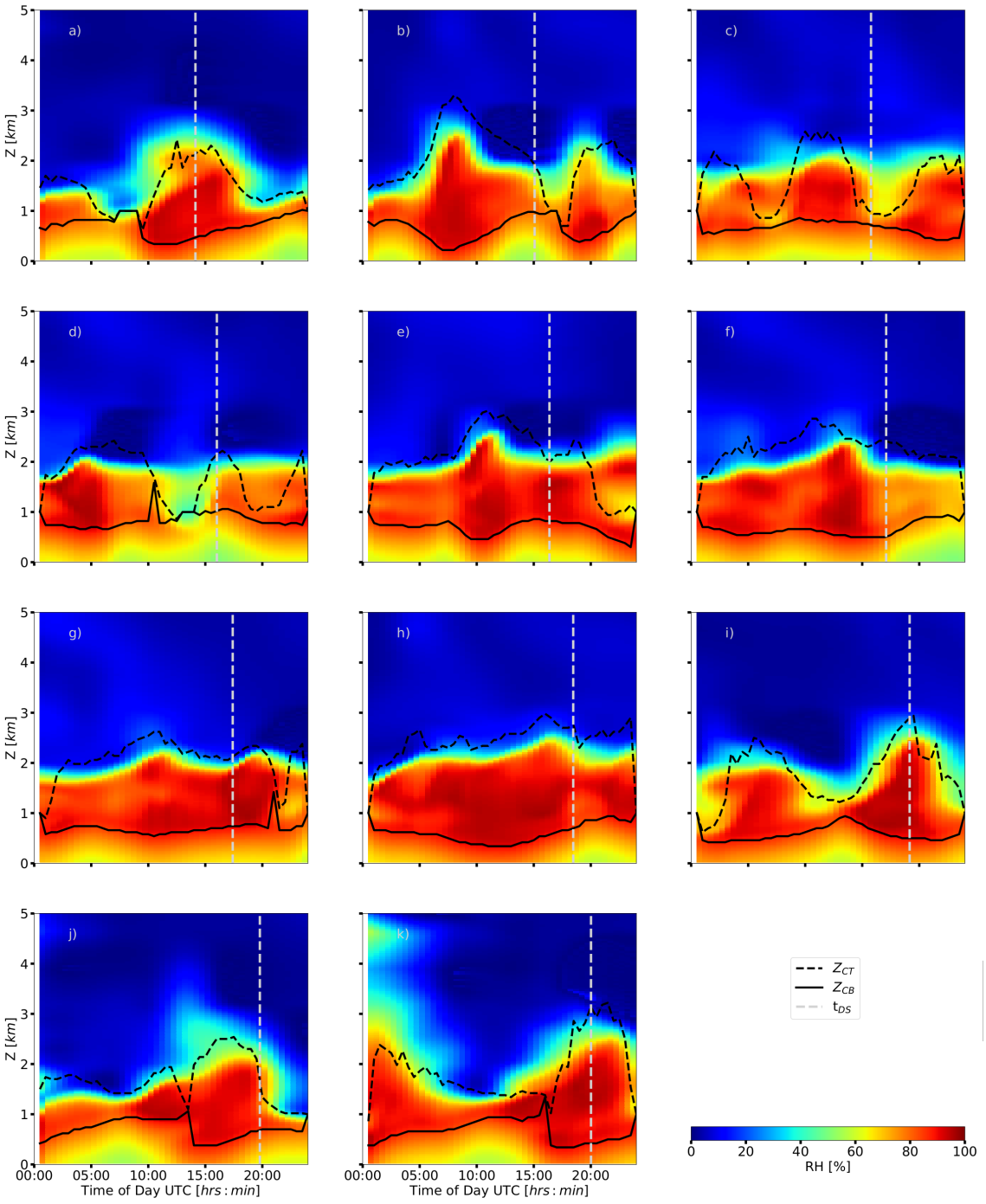

Figure 4.6: Time-height contour plot of the relative humidity (RH) of the Sim_Con for the domains centered over each DS, where a) to k) represent the locations from DS01 to DS11 respectively. The time at which each DS is launched is represented by the gray dashed line, while time-series of the Cloud Top (Z_{CT}) and Cloud Base (Z_{CB}) altitudes are shown by the dashed black line and solid black line respectively.

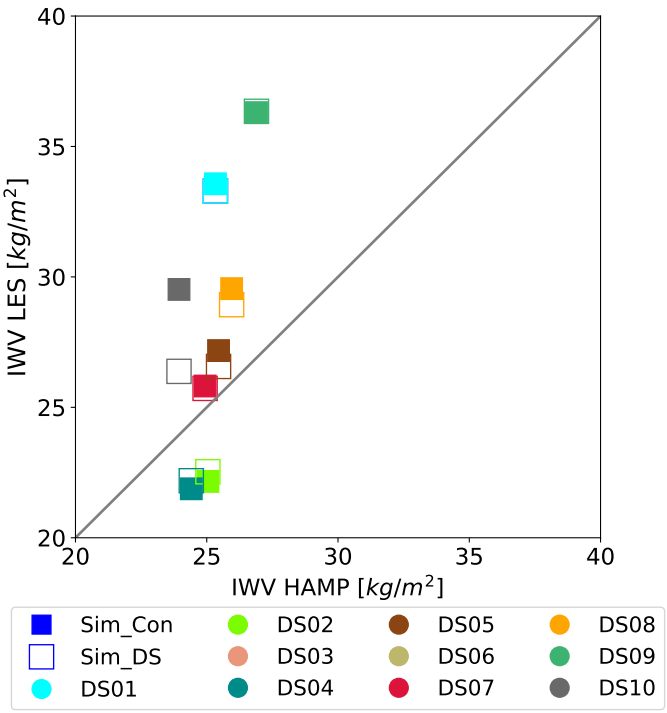

Figure 4.7: Comparison between the Integrated Water Vapor (IWV) calculated from the Sim_Con (unfilled squares) and Sim_DS (filled squares) for each DS location, and the median IWV value from a 1 hour window of HAMP retrievals around the DS launch time.

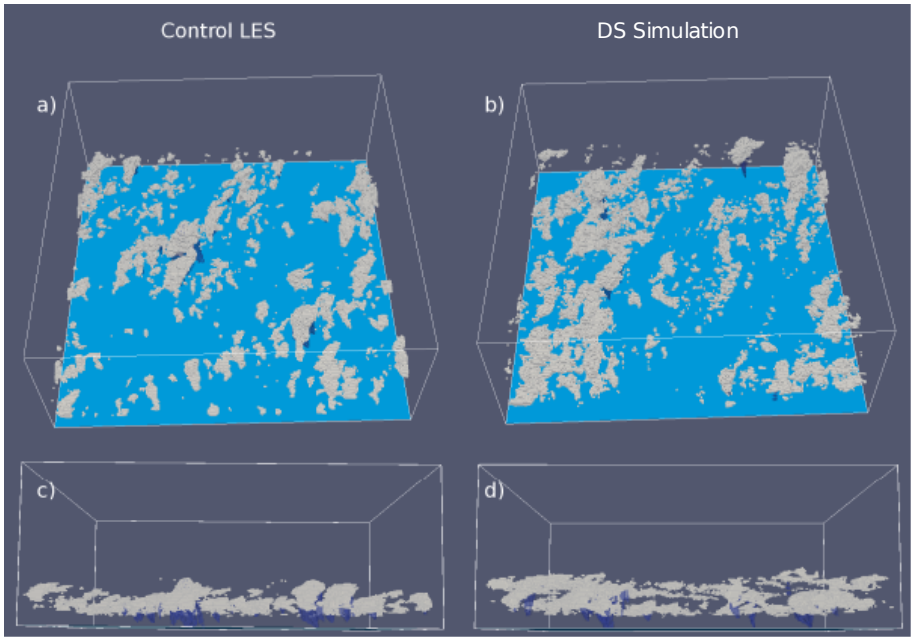

Figure 4.8: The 3D visualization of simulated clouds and precipitation at 14:00 UTC on December 14^{th} 2013. The light blue shows the ocean surface, the light gray shows the surface of the clouds and the dark blue indicates precipitation. A) and b) show tilted top views of the cloud field for Sim_Con and Sim_DS01 respectively, while c) and d) show the side-view of the cloud field for Sim_Con and Sim_DS01 respectively.

and RH are compared to the domain-averaged LES profiles at t_{DS}. The comparison of LES profiles, shown in Fig. 4.9, indicate that a number of features in the atmosphere are captured well by both the Sim_Con and Sim_DS01. These features include the inversion height, the mixing layer height and state, and the lapse rate in the free troposphere. It should be noted that the inversion layer depth and strength should not be directly compared between a domain-averaged profile and a point-sampled profile. A statistical method for comparing inversion height and strength to deal with this problem is explored in a more detailed way in Section 4.4.4 and 4.4.5.

The details of Fig. 4.9 show that the LES reproduces the observed vertical structure of the cumulus capped BL to a reasonable degree. This result is commensurate with most previous LES studies of shallow cumulus in the Trades (Siebesma et al., 2003; vanZanten et al., 2011). In Fig. 4.9a) the region that shows the largest effect of the nudging towards the DS is in the layer between approximately 2 km and 3 km. This is in the region of the inversion layer. It should be noted though that this difference is still quite small. The effect of nudging the simulation towards the DS is more pronounced for variables q_v, RH, and CF. The most significant difference between the Sim_Con and Sim_DS01 profiles occurs in Fig. 4.9d) where the vertical profile of CF is changed as a result of nudging the simulation towards the DS. Compared to the single peak at cloud base in the Sim_Con simulation, the Sim_DS01 profile consists of two peaks, one at cloud base and one at cloud top. The second peak in the CF is potentially related to outflow clouds just below the inversion layer. This is also seen in the 3D visualization in Fig. 4.8c) and d).

Due to the importance of wind-speed (Nuijens and Stevens, 2012) and as the profiles can be quite variable throughout the troposphere, particularly in the boundary layer, it is beneficial to determine how well the LES can represent the wind-speed profiles compared to the observations. To this purpose the wind-speed profiles, u and v, are shown in Fig. 4.9e) and f). The profiles shown for DS01 are based on recordings of wind-speed by the GPS system onboard the DS. Both Sim_Con and Sim_DS01 show a good ability to capture the general profile. However, both simulations tend to underestimate the sharp changes in wind-speed throughout the profile. Based on the profiles it is indicated that the LES can represent the atmospheric conditions to a reasonable degree.

We next focus on a visual comparison of the trade-wind inversion in the water vapor profiles. In the case of both simulations the inversion occurs at approximately 2.4 km. In general, domain-averaged LES profile of q_v exhibit slight differences between Sim_Con and Sim_DS01, with the latter showing a slightly sharper change in the profile at the capping inversion height. Although the nudging towards the DS profile does appear to increase the strength of the inversion, both simulations seem to underestimate the inversion strength. One suspected cause of this underestimation is that the LES profiles being compared are domain-averages. A more detailed comparison of the inversion height and strength are further investigated in Section 4.4.4 and 4.4.5 respectively.

To quantify the difference between Sim_Con and Sim_DS01 in the domain-averaged profiles, the differences between the profiles of CF and q_v were calculated for every time-step in the LES. The resulting time-height contour plots are shown for a) CF and b) q_v in Fig. 4.10. As expected, before the nudging time-window (T) begins there are no differences between the simulations for both variables. The differences in the simulations begin slowly after the start of T and gradually increase in strength, particularly around t_{DS}. Most of the differences in the simulations tend to occur within the cloud region, with a larger CF in Sim_DS01 compared to Sim_Con at around 2 km. This is also true for the difference in q_v. The strengthening of the inversion is highlighted by the larger values of q_v at lower altitudes in Sim_DS01, compared to the corresponding values in the Sim_Con, and lower values of q_v at higher altitudes. The time-height contour plot also indicates that the impact

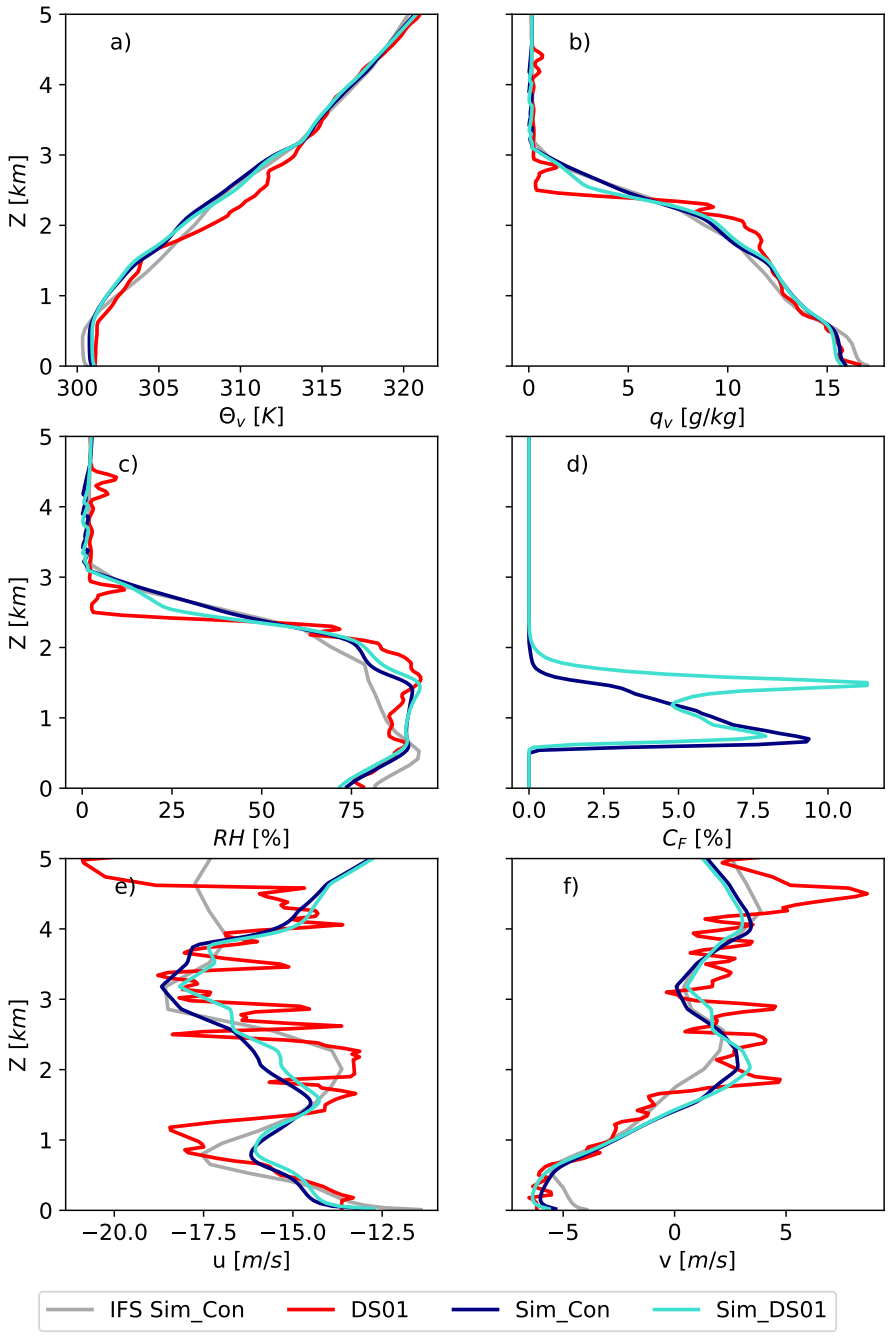

Figure 4.9: Atmospheric profiles of Potential Temperature (Θ), Water Vapor Specific Humidity (q_v), Relative Humidity (RH), Cloud Fraction (CF), West-East wind-speed velocity (u), and South-North wind-speed velocity (v) for DS Observations (red), Sim_Con (navy), Sim_DS01 (light blue). The IFS for the control simulations (IFS_Con) in gray for the time DS01 was launched are included for reference.

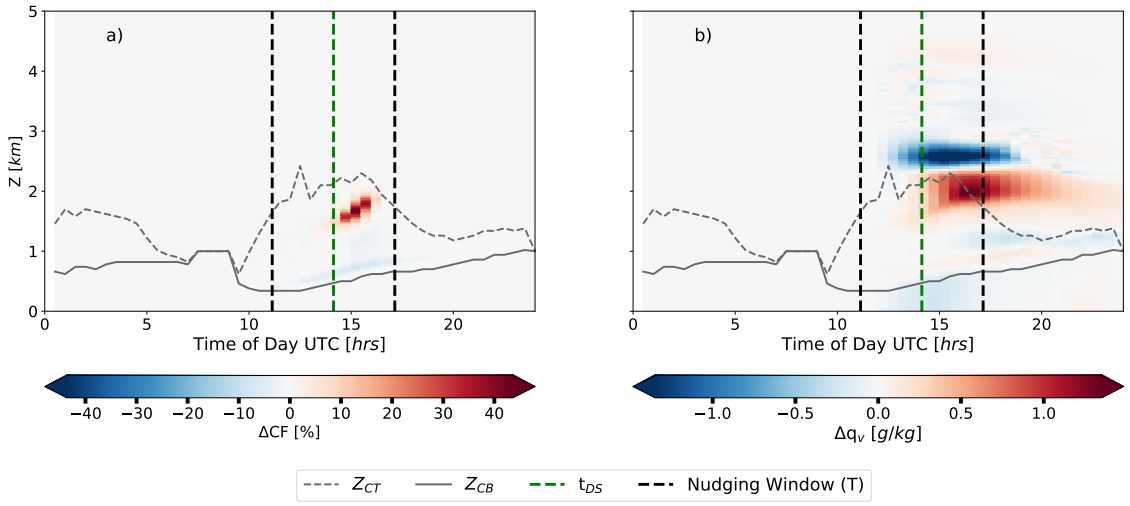

Figure 4.10: Time-height contour plot of the difference between Sim_DS01 and the Sim_Con for a) CF and b)q_v. When ΔCF and Δq_v are greater than 0 if the value for Sim_DS01 is greater than the corresponding value in the Sim_Con. The nudging time-window is shown by the dashed black lines while the DS launch time is shown by the dashed green line. The cloud top altitude and cloud base altitude time series are shown for Sim_Con are shown as the dashed and solid gray lines respectively, as seen in Fig. 4.6a).

of including the DS data in the forcing lasts for a long period after T ends.

4.4.3 Dropsonde Impact Analysis

We now progress from a single case to assessing the impacts for all 22 simulations. To this purpose a special metric is adopted to express the deviation of LES from the observations concerning the vertical structure within the BL. In order to quantify the impact of including the DS data on the thermodynamic state of the BL, the areas between the domain-averaged LES profiles and the corresponding observed DS profiles were calculated. It should be noted that the DS profiles have been linearly interpolated onto the LES vertical grid to ensure a fair calculation of the area between the profiles. The time-evolution of these areas, during T, is then assessed for all 22 cases.

Suppose A_ϕ is the area enclosed between the simulated and observed profiles of variable ϕ, in the lowest 3 km:

$$A_\phi = \int_{0\,km}^{3\,km} \left|\overline{\phi}_{LES}(z) - \phi_{DS}(z)\right| dz \tag{4.4}$$

where $\phi \in q_v, \Theta, RH$, or any variable of interest, with LES and DS indicating the domain-averaged and observed profiles respectively. This area is calculated as a function of time during T and is done for both the Sim_Con and Sim_DS simulations. Time is synchronized between all simulations such that $t = 0$ at t_{DS}. For Sim_Con, the area will be referred to as A_{ϕ,Sim_Con}, while for Sim_DS it is A_{ϕ,Sim_DS}. The next step is to normalize these areas with respect to A_{ϕ,Sim_Con} at t_{DS}. The normalization yields the following two non-dimensional expressions for the skill, S, of the simulation in matching the DS profile.

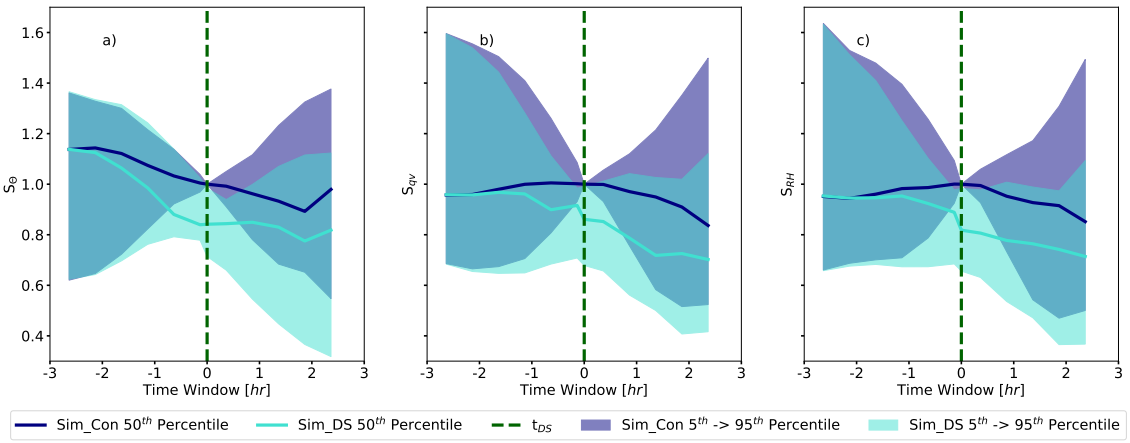

Figure 4.11: A time series of the area between the domain averaged profiles and the corresponding DS profile for a) Θ, b) q_v, and c) RH. The plots are centered on zero, the time of the DS launch (green dashed line), and takes into account the 6 hr window during which Sim_DS is nudged towards the DS profile. The solid navy and light blue lines are the median time-series of the skill for all 11 Sim_Con and 11 Sim_DS respectively, while the shaded regions represent the 5^{th} to 95^{th} percentile across all the time-series.

$$S_{\phi,\,Sim\_Con}(t) = \frac{A_{\phi,Sim\_Con}(t)}{A_{\phi,Sim\_Con}(t=0)} \tag{4.5}$$

$$S_{\phi,\,Sim\_DS}(t) = \frac{A_{\phi,Sim\_DS}(t)}{A_{\phi,Sim\_Con}(t=0)} \tag{4.6}$$

Note that the division of both metrics by $A_{\phi,Sim\_Con}(t=0)$ makes these quantities directly comparable. It should also be noted that the lower the value of $S_\phi(t)$ the better the simulation is at representing the DS profile.

To see if nudging the LES towards the DS improves the representativity of the domain-averaged profiles, this calculation is carried out for the profiles of three variables, Θ, q_v, and RH. A time-series for the duration of T is shown for each of these variables in Fig. 4.11. The shaded region in the time-series designating the 5^{th} to 95^{th} percentiles, and the median indicated separately. Per definition $S = 1$ for Sim_Con at t_{DS}. In the case of all three variables the ensemble spread for the Sim_Con and Sim_DS are identical at the start of the time-window, t_{a0}. This reflects that until that point in time the forcing is identical. Following the beginning of the time-window, the median value of S for Sim_DS in all variables remains smaller than that of the Sim_Con, for a longer time period.

As expected, S begins to decrease, in each of the variables, as Sim_DS begins to feel the effects of the DS data to a larger extent. Following t_{DS}, Sim_DS feels the effects of the DS data to a lesser extent as time progresses. Therefore, the spread in the values of S begins to increase again towards the end of T, as the simulations begin to feel the impact of the pure IFS state. The behavior of the time-series for all three variables indicates that by including the DS profiles into the IFS data leads to better representation of the BL deep vertical structure.

4.4.4 Inversion Height

Previous studies have shown that the strength of the trade-wind inversion has a significant impact on the presence of clouds in the BL (e.g Klein and Hartmann, 1993). As a result

of this and based on the visual impact of nudging in the region of the capping inversion in Fig. 4.9 it is important to determine if the capping inversions in the LES are representative of observations. To assess whether the visual impact of nudging leads to an improvement in the representativeness, a comparison of the inversion height and strength needs to be derived from both model data and observations. In literature, there have been a large variety of methods proposed for this (Albrecht et al., 1979; Stull, 1988; Wood and Bretherton, 2004; Teixeira et al., 2008; Lock, 2009; Neggers, 2015; Gentine et al., 2015).

This study explores the use of a new probabilistic method for determining the inversion height and strength. This method makes use of probability density functions (PDFs) of inversion height and strengths as diagnosed over all columns in the LES. It is designed to achieve a fair comparison between measurements and high-resolution simulations.

The first step is to calculate the discretized vertical gradient (Γ_ϕ) of a variable ϕ as follows:

$$\Gamma_\phi = \left| \frac{\Delta\phi}{\Delta z} \right| \tag{4.7}$$

where $\phi \in \{q_v, \Theta_v\}$ and Δ represents the difference between two model levels. The next step is to apply this procedure to i) the DS profile and ii) all columns in the three-dimensional LES field at t_{DS}. This yields a single inversion height for the DS and a PDF of inversion heights for the LES. The final step is to compare up to three modes, defined as the three largest local maxima in the PDF, to the single observed value. The closest mode is then selected as the inversion height of the LES, referred to as the *Selected Mode*.

A first benefit of using the probabilistic method described above is that it avoids comparing the domain-averaged profiles to single point samples. Secondly, by scanning multiple modes to establish the simulated inversion height we increase the chance that we select one that best reflects the physical meaning of the height that is derived from the DS. For example, at cloud base the vertical profiles can exhibit strong jumps, that are associated with the cumulus transition layer (Albrecht et al., 1995; Neggers et al., 2007). Also, the DS-derived height does not necessarily reflect the trade-inversion. By including up to three modes it accounts for this possibility. The strongest gradients are typically seen at i) the trade-inversion, ii) the cloud base transition layer, and iii) possibly one in between. By considering up to three modes instead of only one, the most relevant height is automatically considered. In the LES the depth of the inversion layer reflects the spread among inversion heights among all columns in the grid, each calculated as the altitude of the strongest gradient. This means that the width of the PDF represents the depth of the inversion layer.

The probabilistic procedure is now illustrated with some concrete examples. Figure 4.12a) and c) show the observed and simulated inversion heights for DS01 and DS03 respectively. The first three LES modes are indicated for both Sim_Con (navy) and Sim_DS (light blue). The DS-derived inversion height is indicated by the dashed green line, while the LES Selected Mode is indicated by the crosses. Figures 4.12b) and d) also show the respective observed and domain-averaged q_v profiles for reference. What is clear from these two examples is that the first three modes in LES reflect the Trade-inversion, the cloud base inversion, and an additional third jump in the cloud layer. Interestingly, the trade-inversion does not always have the largest mode in the LES. However, selecting the LES mode closest to the observed one still ensures that the most relevant inversion height in the LES is chosen for the comparison, and also occurs relatively frequently in the domain.

To determine whether the inversion heights in the LES are representative of the DS-derived inversion heights, the Selected Modes in the inversion height PDFs are compared to the DS-derived inversion heights for all cases. Figure 4.13 shows the comparison between the

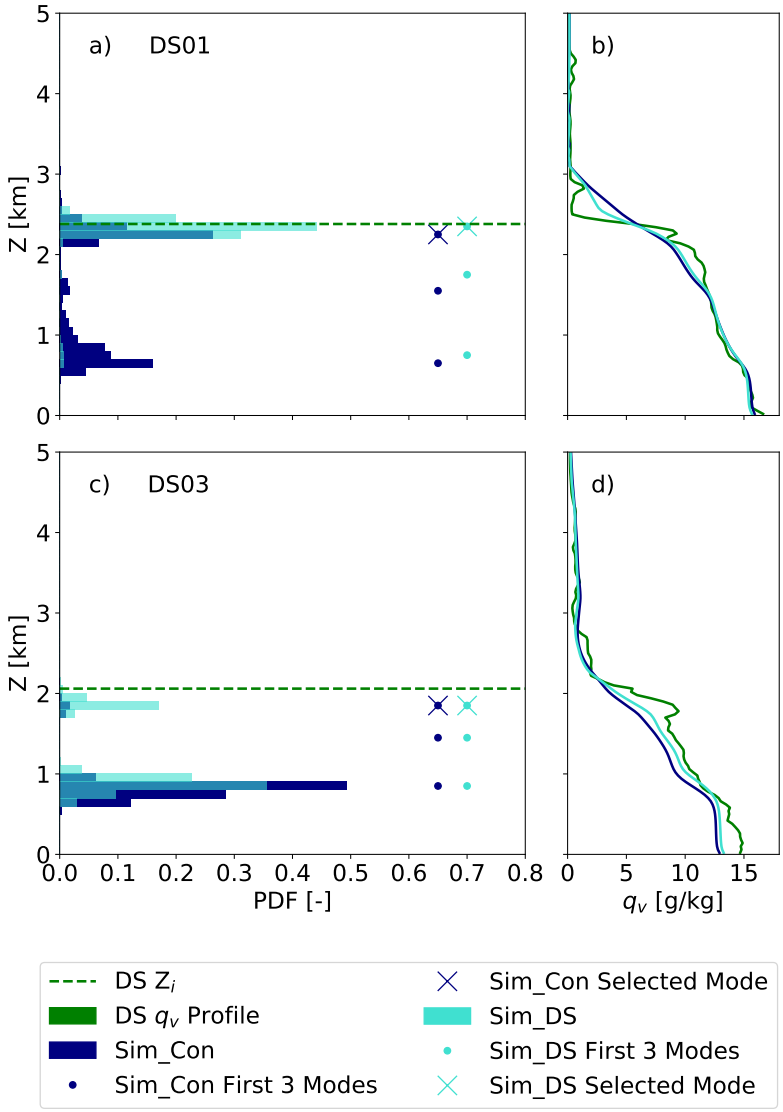

Figure 4.12: a) DS01 and c) DS03 Probability Density Functions (PDFs) of the altitudes at which the maximum Δq_v occurs for each column in the LES domain for the Sim_Con (navy) and Sim_DS (light blue). The inversion altitude in the corresponding DS profiles is given by the green dashed horizontal line. The dots represent the three largest local maximum number of occurrences, while the crosses represent the LES mode selected by the probabilistic method. c) and d) show the Sim_Con (navy) and Sim_DS (light blue) area-averaged profile for q_v for the location and time of DS01 and DS03 respectively. The corresponding q_v profiles for the DS are shown in green in b) and d).

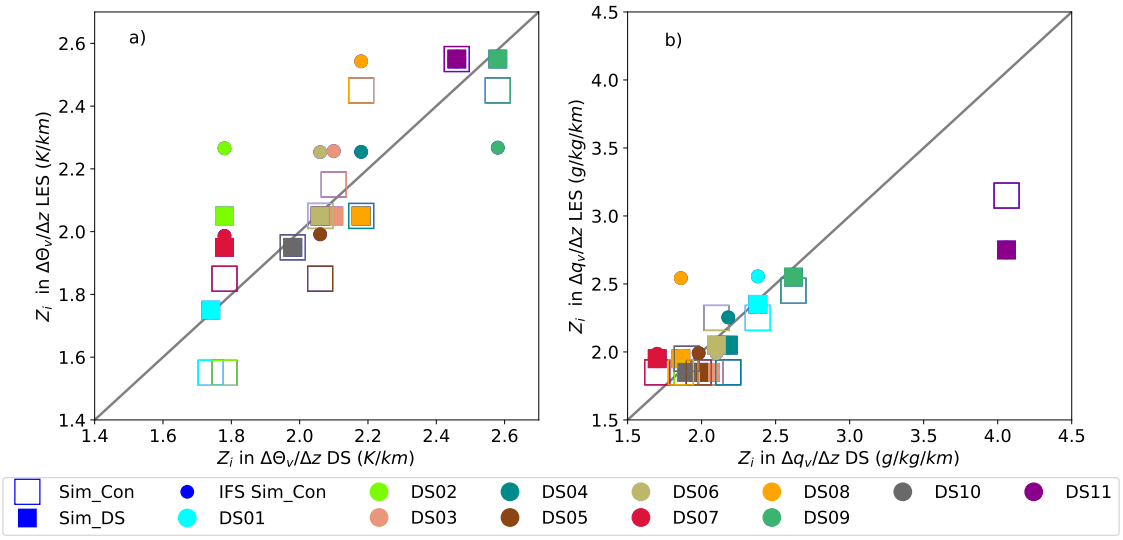

Figure 4.13: Comparison between the inversion heights in the DS profile and the height of the Selected Mode from the inversion height PDFs for all simulations, for a) Θ_v and b) q_v. The unfilled squares represent the modes in the Sim_Con while the filled squares represent the Sim_DS. The inversion heights for the IFS dataset are also included for Sim_Con (IFS Sim_Con) as a reference to where the LES is nudged.

altitudes of the Selected Modes, in Sim_Con and Sim_DS, compared to the inversion heights in the corresponding DS profiles, for a) Θ_v and b) q_v. It should be noted that all 11 Sim_DS are included in Fig. 4.13a), however the Selected Mode for two of the Sim_DS cases occurs at the same altitude as the Selected Modes for two of the other Sim_DS cases. From this comparison it is therefore concluded that the LES is successful in capturing inversions at altitudes that are observed by the DSs for both Θ_v and q_v.

4.4.5 Inversion Strength

Next the inversion strength is calculated. To this purpose only the grid locations which have their inversion height at the level of the Selected Mode are considered. The median over the subset of inversion strengths is then compared to the DS derived inversion strength. An example of the inversion strength PDFs derived for Sim_Con and Sim_DS01 is described in the Appendix.

Figure 4.14a) shows that both the Sim_Con and Sim_DS reproduce the observed DS inversion strength in Θ_v to a reasonable degree. However, the spread among the LES values is quite significant. In addition, Fig. 4.14a) shows that the inclusion of the DS profile in the forcings appears to only improve the inversion strength in the Θ_v in approximately 36 % of the cases. Figure 4.14b) shows that the performance for the strength in the humidity inversion is worse, being underestimated by both Sim_Con and Sim_DS. The IFS data also underestimates the inversion strength in Θ_v in 90 % of the cases.

The considerable difference in performance for the strength of the inversion for temperature and humidity is remarkable. We speculate that various reasons could exist for this, including i) extremely low humidity observed above the Trade inversion, ii) the significantly underestimated inversion strength also in the IFS, seen in Fig. 4.9b) and Fig. 4.14b). Both effects could conspire to make advective forcings in the vicinity of the inversion, as derived from the IFS, less reliable. It could be the case that these forcings play a big role in

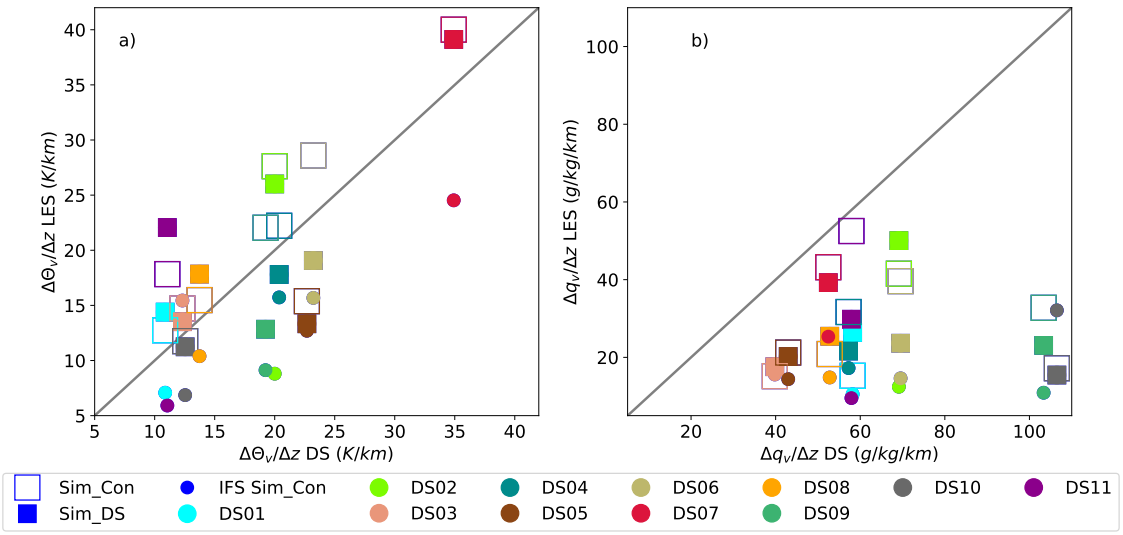

Figure 4.14: Comparison of inversion strengths in a) Θ_v and b) q_v as calculated using Eq. 4.7 for all DSs, Sim_Con (unfilled squares) and Sim_DS (filled squares), where individual colors relate both simulations to their corresponding DSs. The inversion strength for the IFS dataset are also included for Sim_Con (IFS Sim_Con) as a reference to where the LES is nudged.

establishing the strong inversion that is observed. When inversion strength is underestimated in the GCM, sharp differential advection across the inversion is likely not captured. Investigating this possibility and addressing its impact are a future research topic.

4.4.6 Sensitivity Studies

An additional 14 simulations were run to determine the sensitivity of the results in relation to different parameters. These parameters include i) the tightness of the nudging as expressed by τ, ii) the length of T around t_{DS}, and iii) the vertical discretization in the LES (Δz). Each of these simulations were run for the DS01 location. In the analysis only the lowest 3 km were considered, where the DS has the largest impact. The area A_{qv}, as defined in Eq. 4.4, is thus calculated over the lowest 3 km at t_{DS}. To calculate the area between profiles the DS profile was linearly interpolated onto the respective LES vertical grid.

Nudging timescale: Ten simulations, divided between Sim_Con and Sim_DS, were carried out to study the impact of increasing and decreasing τ in the LES. The different τ values used in this sensitivity study are summarized in Table 4.2. For the purpose of analyzing the impact of varying the value of τ, Sim_Con and Sim_DS for DS01 are used. Figure 4.15a) shows A_{qv} for each value of τ at t_{DS}. For each value of τ the value of A_{qv} for Sim_DS is consistently smaller than that of Sim_Con. Note the slightly larger value for A_{qv}, for Sim_Con, when $\tau = 1$ hr compared to when $\tau > 1$ hr. This deviation is potentially due to the τ being set to a tight nudging value. The value of A_{qv} does not vary significantly for values of τ between 2 hrs and 6 hrs. In the Sim_DS studies, the value of A_{qv} increases with increasing τ. This indicates that the nudging effect decreases with increasing τ. Therefore, it can be determined that the simulation where τ is equal to 1 hr, where the nudging strength is strongest, captures the DS profile with the highest accuracy. However, one issue with using $\tau = 1$ hr is that the turbulence unable to act freely in the simulation.

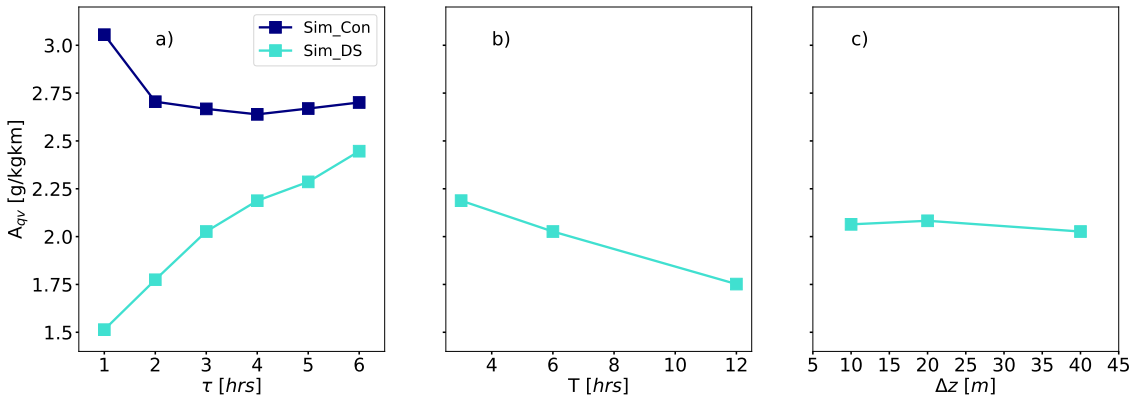

Figure 4.15: The area calculated between the observed q_v profile and the simulated q_v profiles, at the DS launch time, for the sensitivity simulations for a) the tightness of the nudging as expressed by the nudging timescale (τ), b) the length of the nudging time-window (T), and c) the vertical resolution (Δz). The Sim_Con (navy) was only run for the sensitivity simulations on the nudging tightness.

Nudging Time-window: Two simulations were carried out to study the impact of the duration of the time window during which the DS profile affects the IFS dataset. Similar to the experiments conducted for τ, these simulations are summarized in Table 4.2. Using the method described for the Sim_DS, simulations where $T = 3$ hrs and $T = 12$ hrs were generated. Figure 4.15b) shows A_{qv} at t_{DS} for each value of T. A_{qv} is lowest for $T = 12$ hr, and largest for $T = 3$ hrs. Therefore, the larger time window makes the nudging more effective allowing the simulation to be more representative of the BL observed.

Vertical Resolution: The final sensitivity study conducted was on the vertical resolution. As mentioned in the previous sensitivity experiments, Table 4.2 summarizes the two simulations carried out for this sensitivity study. This study was carried out to investigate whether having a higher vertical resolution would improve the representation of the BL in the atmospheric profiles. Two simulations were carried out in the vertical resolution test, one where $\Delta z = 20$ m and a second where $\Delta z = 10$ m. All LES input files were interpolated onto a higher vertical grid resolution. Figure 4.15c) shows A_{qv} for each of the studied resolutions. Over the three simulations A_{qv} varies by approximately 0.05 g kg^{-1} km^{-1}. Therefore, it is determined that there is very little impact in increasing the vertical resolution, for this case.

4.5 Discussion

Throughout this study the LES has shown good skill in reproducing the mean thermodynamic structure, wind-speeds, IWV, and inversion heights. A significant impact due to nudging the LES towards DS profiles is seen on the simulated trade-wind cumulus fields. Finally a probabilistic method for comparing observed and simulated inversion properties has been shown to be successful.

There are however some shortcomings. For example the representation of the inversion strength, particularly in humidity. As speculated earlier this could be due to the extremely low values in humidity directly above the inversion, or potentially due to the representation of the inversion in the IFS dataset. Investingating this shortcoming is definitely an important future research topic. A second possible shortcomming is that the use of a limited domain size can artificially boost variability in the mean.

4.6 Conclusions

In this study LES realizations were generated of cumulus cloud fields observed by HALO during NARVAL. The main novelties compared to previous studies of this kind (e.g. Bretherton et al., 1999; Siebesma et al., 2003; vanZanten et al., 2011) include i) the use of time-varying large-scale forcings and ii) the incoporation of dropsonde profiles using a simple assimilation method.

The main results of this study are briefly summarized as follows:

- The simulations show a strong temporal evolution of the boundary layer state, commensurate with previous observational studies at the BCO site.
- Comparing Sim_Con and Sim_DS with the independent observational data from HAMP reveals that domain averaged LES IWV is representative of the observed median IWV.
- The representation of the atmospheric profiles throughout the boundary layer is improved in Sim_DS compared to Sim_Con. This is a result of nudging the LES towards the observed state in the large-scale forcings as opposed to the prescribed large-scale forcings.
- The probabilistic method for evaluating inversion properties shows that the inversion height is reproduced to a satisfactory degree. However, the simulated inversion strength contains significant spread, and is also significantly underestimated in water vapor.
- As expected, sensitivity tests show considerable dependence on the tightness of the nudging, with the more representative boundary-layer profiles in the LES with a nudging timescale of 3 hrs compared to 6 hrs, when the simulations were compared to observed profiles. Also concluded from these sensitivity tests was a weak dependence on vertical resolution, with little difference when the resolution is increased by a factor of 2.

The method detailed in this study can also be applied to several other field campaigns where the profiles of a number of measured variables can be blended into the large-scale forcings.

In a related and ongoing follow-up study, the clouds in these simulations are evaluated against additional observations recorded by instrumentation onboard HALO, for example HAMP. A key question addressed in that study is how well the observed horizontal variability in the convective cloud field is reproduced by the LES, and how this relates to spatial organization.

acknowledgments

The research carried out for this study was conducted as part of the High-Definition Clouds and Precipitation for advancing Climate Prediction (HD(CP)^2) project funded by the German Federal Ministry of Education and Research within the program "Research for Sustainable Development (FONA)" www.fona.de, under the number 01LK1504C. The authors would like to thank Dr. Mario Mech and Marek Jacob for their assistance regarding information about HALO and the dropsonde data, and Dr. Jan Chylik for his assistance with the DALES model. We would also like to thank the DLR for providing the measurements by HALO during NARVAL-South, which was funded by the DFG SPP project 1294.

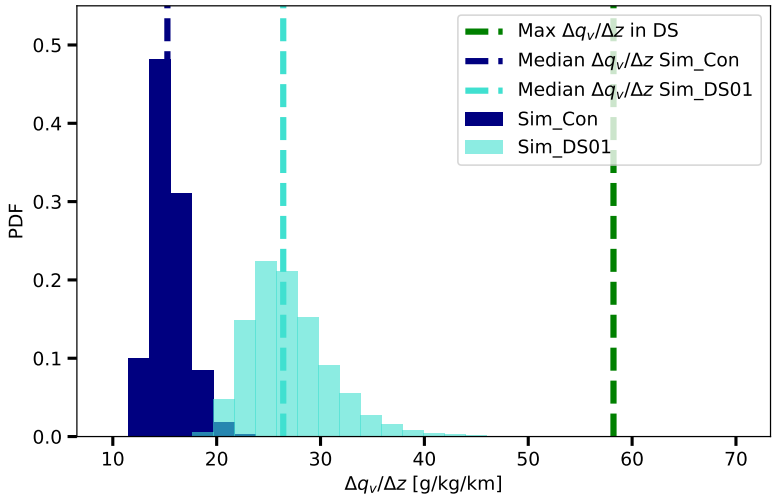

Figure 4.16: PDF of maximum $\Delta q_v/\Delta z$ values for the Sim_Con (navy), Sim_DS01 (light blue), the median of both simulations represented by the dashed line of the respective colors, and the maximum $\Delta q_v/\Delta z$ in DS01 profile represented by the dashed green line.

Appendix

Determining the Inversion Strength

As described at the beginning of Section 4.44.4.5, the inversion strength in q_v and Θ_v is calculated for every column in the three-dimensional LES field with an inversion height within the Selected Mode. A PDF of these inversion strengths is produced for each Sim_Con and Sim_DS. The median of these inversion strength PDFs is then compared to the inversion strength in the corresponding DS profile.

Taking DS01 as an example, Figs. 4.16 and 4.17 show the PDFs of the inversion strength in q_v and Θ_v respectively. The medians of the Sim_Con and Sim_DS01 PDFs, represented by the dashed navy and light blue lines respectively, are compared with the inversion strength in the DS01 q_v and Θ_v profiles, represented by the dashed green line.

From Fig. 4.16 it is clear that both simulations underestimate the inversion strength compared to the observed inversion strength. While both simulations underestimate the inversion strength, the median of the Sim_DS01 PDF is more representative of the inversion strength in the DS01 q_v profile. For the inversion strength in Θ_v comparison Fig. 4.17 shows that both simulations capture the inversion strength to a relatively high degree. Comparing the median inversion strength in Θ_v for both simulations to the observed inversion strength shows that the Sim_Con has a more representative in this case. This is repeated for the Sim_Con and Sim_DS at each of the DS locations. The results of the comparisons across all DS locations are seen in Section 4.4.5.

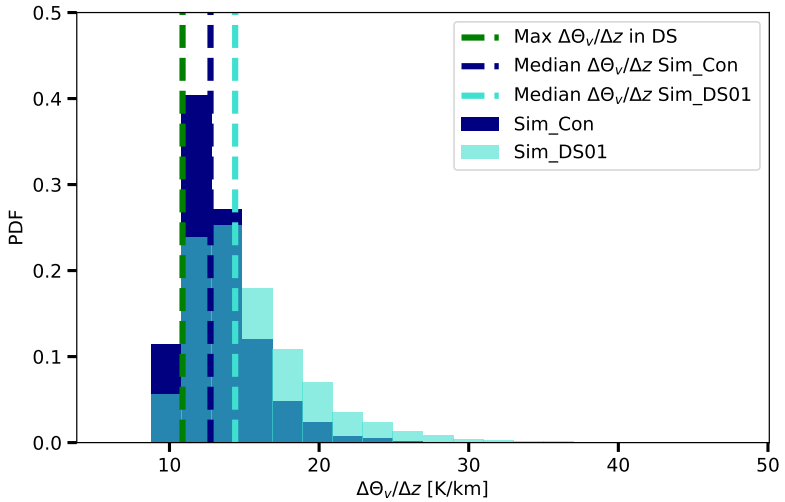

Figure 4.17: PDF of maximum $\Delta\Theta_v/\Delta z$ values for the Sim_Con (navy), Sim_DS01 (light blue), the median of both simulations represented by the dashed line of the respective colors, and the maximum $\Delta\Theta_v/\Delta z$ in DS01 profile represented by the dashed green line.

Chapter 5

Confronting water vapor variability in limited domain LES with retrievals from HAMP during NARVAL South

Abstract

This study compares the variability in integrated water vapor and liquid water path from limited domain large eddy simulation (LES) realizations of trade-wind cumulus cloud fields to retrievals derived from observations by the High Altitude and Long Range Aircraft (HALO) Microwave Package (HAMP) instrument during the first Next Generation Aircraft Remote-sensing for Validation (NARVAL) campaign. A composite case is designed that reflects the conditions observed during research flight 4, which took place on December 14^{th} 2013. The configuration of the composite case is compared to a well-known cumulus case, based on the Rain in Shallow Cumulus over the Ocean (RICO) campaign, which took place in the same region in 2004. The aim of the study is to investigate whether a large-domain simulation is required to capture the range of values from the retrievals derived from the HAMP measurements, and how smaller domains and radiation have an impact. This study also aims to gain an insight into how the integrated water vapor, liquid water path, and precipitation flux correlate with the organization index (I_{org}) metric for expressing the spatial organization of the cloud field. The variability in the simulated integrated water vapor does approach the values from the HAMP retrievals when the LES has a domain of size 51.2 km^2, while the smaller domains significantly underestimate the variability in the integrated water vapor. The variability in both integrated water vapor in the NARVAL simulation and RICO simulation are relatively similar when compared. In both the NARVAL and RICO cases there is a strong correlation between the variability in the integrated water vapor, liquid water path, and precipitation flux, and the I_{org}. The slope of these dependencies differs between the cases, in particular for the liquid water path and precipitation flux. This suggests that not only are the clouds differently structured with a flower like structure seen in the NARVAL case, which tends to indicate the presence of outflow cumulus clouds, and a gravel like structure in the RICO case, but also that the I_{org} is predominantly controlled by the water vapor distribution. Switching off the radiation in the NARVAL case supports this hypotheses, as there is a reduction in the presence of outflow clouds and as such it resembles the RICO case to a higher degree.

5.1 Introduction

Shallow cumulus cloud fields are a common and persistent feature found over large areas in the North Atlantic trade-wind region. The accurate representation of shallow cumulus clouds in both weather and climate models is important due to their role in the transport of moisture and momentum in the atmosphere (Stevens, 2007; Siebert et al., 2013), and their significant impact on the Earth's radiation budget. At the heart of uncertainties in climate projections is the uncertainty in the feedback from shallow cumulus clouds in response to climate change (Bony and Dufresne, 2005; Zelinka et al., 2012).

The temporal and spatial organization of a shallow cumulus cloud field (Tompkins, 2001) also has an impact on how shallow cumulus affects climate, which prioritizes gaining insight into why this phenomenon occurs and how it is maintained. Convective organization has been a topic that has been widely researched and discussed for several years. Organization such as self-aggregation has been identified based on an increase of the variability in the moisture over the large-scale region (Wing, 2019). Using large-eddy simulation (LES) models Bretherton and Blossey (2017) indicated that the organization of the cloud field is heavily impacted by precipitation (Wing et al., 2017). As a result it is important that large-domain simulations are used to capture this organization in models (Muller and Held, 2012).

In a recent study by Naumann and Kiemle (2019) investigate the question of whether simulations with grid spacings from hectometers to kilometers could represent the water vapor variability that was observed by the Water Vapor Lidar Experiment in Space (WALES) which was mounted to the High Altitude and Long Range Aircraft (HALO) during the first and second Next Generation Aircraft Remote-sensing for Validation (NARVAL) campaigns, NARVAL 1 and NARVAL 2 (Stevens et al., 2019a). They reported a weak impact of the grid resolution on simulated water vapor variability compared to the observations. The domain size of their simulations was very large, therefore the question remains at what domain size does the variability begin to be artificially underestimated, e.g. Reilly et al. (2019), where a very small domain size of 12.8 x 12.8 km^2 was studied. In addition the method by which the radiation is treated can also potentially have an impact on the spatial variability in water vapor, as it plays an important role in establishing dry regions (Bretherton et al., 2005). A main difference between the study conducted by Naumann and Kiemle (2019) and the present study is the observational instrumentation taken into account. While Naumann and Kiemle (2019) takes the observations from the WALES instrument into account, the retrievals of the integrated water vapor (IWV) and liquid water path (LWP) are determined from the HALO Microwave Package (HAMP) (Jacob et al., 2019), and are therefore worth comparing the LES too.

In this study the retrievals from the HAMP instrument, which was also onboard HALO for both NARVAL campaigns, are supplemented by results from an LES in order to investigate the potential link between the spatial organization of the cloud field and atmospheric properties such as the precipitation flux, the variability in IWV, and variability in LWP. First, this study aims to determine whether the variability in IWV and LWP in the observations can be reproduced in an LES with a limited domain. The second goal is then to use the simulations to gain an additional insight into the variability by using the three-dimensional field from the LES to determine the spatial organization, which cannot be measured by HAMP. To this purpose a composite case, based on research flight 4 (RF04) of the first NARVAL campaign, is built using large-scale forcings derived from the European Center for Medium Range Weather Forecasts (ECMWF). In order to determine whether the LES has the ability to reproduce the variability in IWV and LWP that is observed, metrics are derived for the variability in both the LES data and the HAMP retrievals. An additional

metric for the spatial organization is determined to investigate the link between the variability in IWV, and LWP, and the organization of the cloud field. The results from an LES study on the Rain in Shallow Cumulus over the Ocean (RICO) campaign will also be taken into account in this study as a reference.

This study is divided into seven sections, beginning with a description of the datasets including the retrievals, LES models, and large-scale forcings in Section 5.2. The methods for deriving the variability in IWV, and LWP, and the spatial organization are described in Section 5.3. The results of the simulations are presented in Section 5.4, where the variation in the IWV values is compared between the LES and the retrievals, while also investigating the response in the organization of the cloud field. An investigation into the impact of the domain size and the radiation used in the LES is described in Section 5.5. Finally the successes and shortcomings of the study will be discussed, along with the main conclusions, in Sections 5.6 and 5.7.

5.2 Data

5.2.1 HAMP Retrievals

This study makes use of retrievals from the HAMP instrument during the fourth RF04 of NARVAL South. HAMP was mounted in the bellypod of HALO during the NARVAL campaigns in 2013 and 2016. Detailed descriptions of the NARVAL campaigns are found in Stevens et al. (2019a), with a descriptions of the first NARVAL campaign also found in Klepp et al. (2014) and Chapter 3. The HAMP instrument consists of 2 nadir pointing instruments, a cloud radar which operates at 32 GHz and a suite of passive remote sensing microwave radiometers which operate at 26 frequencies between 22.24 and 183.31 GHz (Mech et al., 2014). The cloud radar is a MIRA-36 (Melchionna et al., 2008) radar.

The retrievals of liquid water path (LWP) and IWV only require the use of 7 Ka-bands, within the rage 22.24 GHz to 31.40 GHz along with the 90 GHz channel. These frequencies are similar to those used by satellite instrumentation, however the exception is the size of the precipitation particles. The retrievals of IWV have an accuracy of less than 1.4 kg m^{-2}, while the accuracy of the LWP retrievals are 20 g m^{-2} for retrievals of LWP less than 100 g m^{-2} and around 10 % for retrievals of LWP that are greater than 100 g m^{-2} (Jacob et al., 2019). In order to reduce potential noise, the retrievals around the first and last dropsondes are not taken in to account in this study.

To gain some insight into the observational dataset used in this study, a time-series of the retrieved IWV and liquid water path (LWP) values from HAMP are shown in Fig. 5.1a) and c) respectively. From both the IWV and LWP time-series a substantial amount of variability can be seen. As seen in the IWV time-series, shown in Fig. 5.1a), the IWV value peaks to approximately 50 kg m^{-2} at the beginning and end of the research flight. Soon after the flight begins there is decrease in IWV. The level of IWV then continues to vary in amplitude between 20 kg m^{-2} and 35 kg m^{-2}, until the significant increase in IWV towards the end of flight. While there is some variation in the IWV time-series, the LWP time-series has significantly more variability, with numerous local maxima in LWP throughout RF04. Figure 5.1c) indicates there are several short time windows during which the level of LWP increases and decreases relatively quickly. As noted in both time-series there are several time windows during which there are no retrievals. This is based on flags which indicate the presence of ice or precipitation at those time-steps which can affect the retrieved IWV and LWP values.

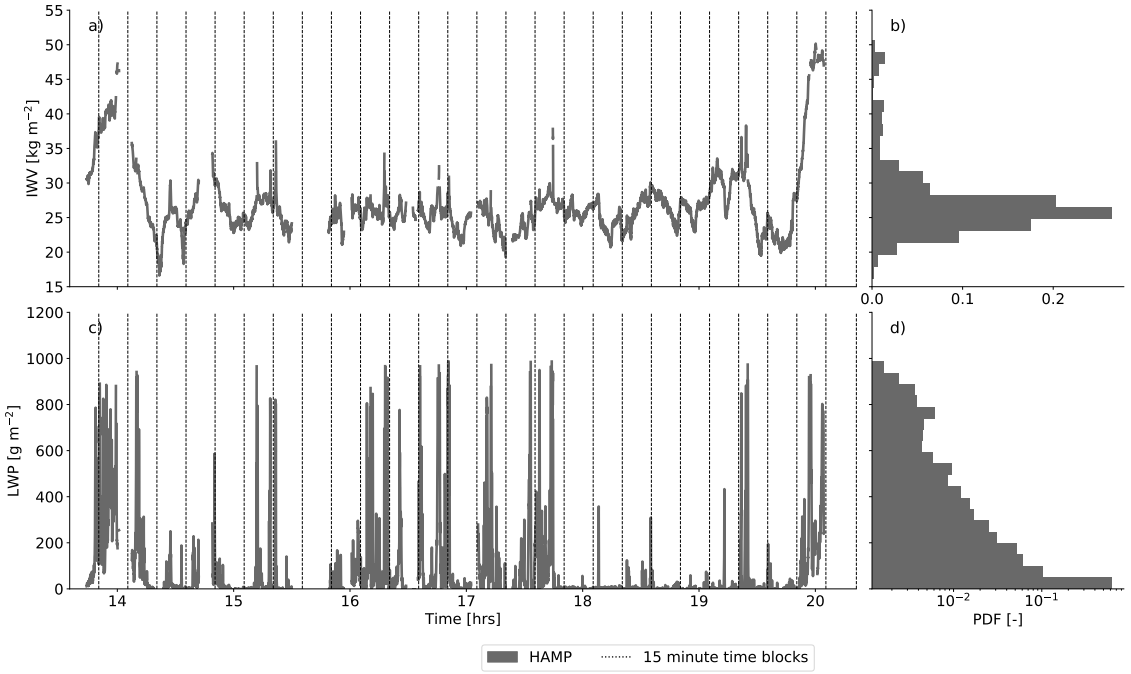

Figure 5.1: Time-series and probability density function (PDF) of the retrieved Integrated Water Vapor (IWV) (a and b) and Liquid Water Path (LWP) (c and d) by the HAMP instrument. The time between each vertical line represents the 15 minute time windows during which the median and standard deviation are calculated.

In order to quantify the distribution of IWV and LWP values throughout RF04, a probability density function (PDF) of both variable across the time-series was produced, as can be seen in Fig. 5.1b) and d) respectively. The PDF of IWV values, as seen in Fig. 5.1b) indicates that in a majority of cases the IWV is usually between 20 kg m^{-2} and 35 kg m^{-2}, however the higher IWV are also visible in the PDF. While the PDF for IWV has a skewed Gaussian shape, the PDF for LWP looks more logarithmic shaped. This is due to the large number of occurrences of very small values of LWP,and significantly less number of occurrences of high LWP values. The PDF does indicate that there is a significant distribution of LWP between the very low LWP values and the very high values.

5.2.2 Large-Eddy Simulations

Simulations for two different trade-wind cumulus cloud cases are used in the study, as simulated using two different LES codes. The primary simulations are generated using the Dutch Atmospheric Large Eddy Simulation (DALES) model (Heus et al., 2010) for the newly created NARVAL case. This NARVAL case is compared to a reference simulation created with the University of California Los Angeles Large-Eddy Simulation (UCLA-LES) model for the RICO campaign, as used in a previous study by Seifert and Heus (2013). Both simulations are composite cases, which means that the large-scale forcings are constant with time and reflect conditions during a longer period. The simulation time for both cases was 48 hours.

5.2.2.1 NARVAL RF04

The DALES model is used to generate simulation based on the NARVAL campaign, referred to as NARVAL$_{rad}$ for the remainder of this study. Simulations are generated using a similar setup to those run by Reilly et al. (2019), however there are some significant differences in the setup of the model. The main size difference is the the domain size over which DALES is run, which includes various sizes with the largest being the NARVAL$_{rad}$ case with a domain size of 51.2 x 51.2 x 5.02 km^3, discretized at a spatial resolution of 100 x 100 x 50 m^3.

The domain of the NARVAL$_{rad}$ case is fixed in space, an Eulerian domain, centered around the location of dropsonde 4, as this is towards the center of the research flight. The large-scale subsidence and advective tendencies are prescribed. Horizontal periodic boundary conditions are applied to the LES domain, with a prescribed sea-surface temperature (SST). Roughness length and interactive fluxes are also prescribed. Nudging, as demonstrated by (Neggers et al., 2012; van Laar et al., 2019; Reilly et al., 2019), is only applied in the upper vertical layers in the model. This nudging is applied from an altitude of 3 km to the top of the DALES domain at a slow synoptic time-scale of 6 hrs. This reduces the drift in the upper atmosphere. Below 3 km, DALES is run with an idealized setup, allowing the boundary layer to develop freely, with the profiles from the large-scale forcing only providing the initialization and forcing profiles.

Horizontal advection is also prescribed for all the prognostic variables. Using the large-scale pressure field the geostrophic forcing for the wind is derived. This simulation also makes use of the Seifert-Beheng bulk microphysics scheme, details of which can be found in (Seifert and Beheng, 2005), and a fully interactive radiation scheme that is implemented in DALES. The radiation scheme is initialized at 00:00 UTC and contains a changing solar zenith angle with time. This changing solar zenith angle introduces a diurnal cycle in the solar radiation. A detailed description of the DALES code is provided by Heus et al. (2010).

5.2.2.2 RICO

This study also makes use of a LES study based on the RICO campaign (Rauber et al., 2007b), referred to as RICO$_{norad}$ for the remainder of this study. The RICO campaign took place from November 2004 and January 2005 off the coast of Antigua and Barbuda in the northeast trades. This campaign took place in a similar region as the NARVAL campaign which took place in December 2013. Similar to the NARVAL$_{rad}$, RICO$_{norad}$ is generated on a horizontal domain of 51.2 x 51.2 km^2 with a altitude of 4 km. The resolution of the RICO simulation is also higher with a resolution of 25 m in both the horizontal and vertical directions. Similar to the NARVAL$_{rad}$, the RICO$_{norad}$ also applies horizontal periodic boundary conditions and a prescribed SST (vanZanten et al., 2011).

Organization in the marine cloud field was first described in Seifert and Heus (2013) and then in Neggers et al. (2019). The case is a slowly organizing marine shallow cumulus cloud field, which reflects the marine subtropical subsidence conditions observed. The spatial organization in this case is related to warm precipitation process, producing cold pools with low cloud mass that are separated by convergence lines where clouds tend to congregate.

The double moment microphysics scheme of Seifert and Beheng (2001) is applied with a Smagorinsky scheme for the subgrid transport of momentum, energy, and heat. An interactive radiation scheme is switched off for the RICO simulations, however a cooling

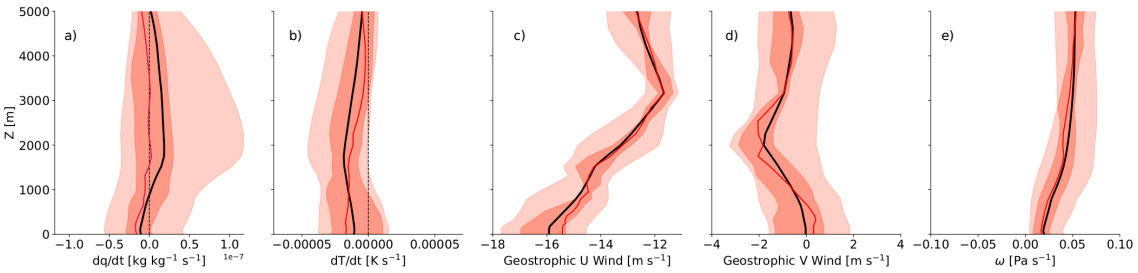

Figure 5.2: Profiles of the large-scale forcings including a) humidity advection (dq/dt), b) temperature (dT/dt) advection, c) geostrophic U wind, d) geostrophic V wind, and e) the pressure velocity (ω) used to initialize the LES. The mean profile, represented by the black line, is used to initialize the simulation. The median (50^{th} percentile) profile is shown by the red line, while the shading represents the 25^{th} to 75^{th} percentile and the 5^{th} to 95^{th} percentile range of large-scale forcings across all dropsondes used in this study.

rate is prescribed for the simulations. A detailed description of the UCLA-LES code used for the RICO simulation is provided in Seifert and Heus (2013).

5.2.3 Composite Large-Scale Forcings

DALES is initialized and forced using a set of large-scale forcing profiles that give an indication of the atmospheric conditions in the region. The large-scale forcing profiles used in this study are profiles from a general circulation model (GCM) that have been averaged over a 0.5 x 0.5 degree domain. To this purpose a combination of analyses and short range forecasts from the Integrated Forecasting System (IFS) in the European Center for Medium Range Weather Forecasts (ECMWF) are used to initialize and force DALES in this study. A detailed description of method applied to derive these forcings is provided by van Laar et al. (2019). Several recent studies have previously also used IFS datasets to drive high resolution simulations of cumulus convection for example Gustafson et al. (2017), Dal Gesso and Neggers (2018), Neggers et al. (2019) and Reilly et al. (2019).

This study makes use of the exact forcing data as applied in the study by Reilly et al. (2019). In the study by Reilly et al. (2019) the LES was driven at each of the 11 dropsonde locations, released during RF04, maintaining time-dependency in the forcing. In contrast, this study makes use of a composite setup with time-constant forcing, obtained by averaging the IFS profiles over all dropsonde locations and over all dropsonde locations and over the full day of the flight. The large-scale forcings from the locations of dropsondes 1 and 11 are excluded in the averaging, because they represent outliers reflecting deep convective conditions, seen in Fig. 5.1.

The use of a composite case is motivated by the full IWV and LWP time-series of the HAMP retrievals which can therefore be used, increasing the sample size of the variability calculated. In the study by Reilly et al. (2019) it was seen that there was significant time-variation in the large-scale forcings at individual dropsonde locations. Compositing removes this variation, making mechanisms leading to spatial variability in water vapor and cloud variables easier to identify. The composite forcing profiles of the humidity advection, temperature advection, geostrophic U wind, geostrophic V wind, and the pressure velocity are shown in Fig. 5.2. The spread in the daily-averaged forcings across all dropsonde locations is indicated by the shading between the 5^{th} and 95^{th} percentile. For all of the forcing variables the overall vertical structure is well defined, with the spread between the different dropsonde locations remaining relatively small compared to the features that

define the vertical structure. The mean profile, seen as the black line in Fig. 5.2, is the main profile used to initialize DALES. Figure 5.2a) indicates that there is a slight drying of the atmosphere close to the sea surface, with a slight increase in moisture above 1000 m. This moistening of the atmosphere remains from 1000 m to the height of the DALES ceiling. Throughout the atmosphere the large-scale profiles indicate that there is a cooling affect, as seen in Fig. 5.2b), where the value of the temperature advection remains less than 0.0 K s^{-1}. There is little variation in the geostrophic wind in both the U and V directions, as seen in Fig. 5.2c) and d). From the large-scale profile of the pressure velocity (ω), as seen in Fig. 5.2e) indicates that there is consistent large-scale divergence throughout the lower troposphere. The RICO_{norad} case is also driven by time-constant composite forcings, and can thus act as a useful reference for the NARVAL case.

5.3 Quantifying Variability and Spatial Organization

5.3.1 Variability in IWV and LWP

To obtain a characteristic value of the spread in the IWV and LWP values, including the temporal variation in that spread, the time-series of IWV and LWP is divided into 27 time-windows that last 15 minutes each, where the boundaries of each time-window can be seen in Fig. 5.1a) and c). To determine the variability in the IWV and LWP, the standard deviation is calculated using the following equation:

$$\sigma_\phi = \sqrt{\frac{\sum(\phi - \bar{\phi})^2}{H}} \tag{5.1}$$

where $\phi \in \{IWV, LWP\}$, $\bar{\phi}$ is the mean, and H is the number of points in the dataset.

Figure 5.3 shows that a σ_{IWV} from approximately 1.5 g m^{-2} to 2 g m^{-2} is the most common throughout research flight 4. There are a number of larger values of σ_{IWV} which are representative of a number of time-windows during which the IWV sharply increases or decreases, which may have to do with deep convective systems near Barbados at the beginning and end of the research flight. As seen Fig. 5.1, during the main part of the flight the variability in the IWV was relatively constant with time.

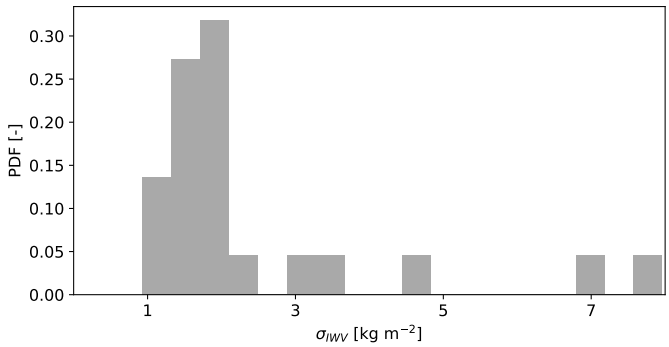

Figure 5.3: Probability density function of the standard deviation of IWV (σ_{IWV}) PDFs computed for the HAMP retrievals during each of the 15 minute time-windows seen in Fig. 5.1.

5.3.2 Spatial Organization Index

To investigate if there is a relation between σ_{IWV} and the organization in the cloud field this study makes use of the Organization Index (I_{org}) parameter (Tompkins and Semie, 2017; van Laar, 2019). I_{org} gives an indication of whether a cloud field is regularly distributed, randomly distributed, or clustered, while also indicating the degree of organization in the field. The organization index parameter is based on the nearest neighbor spacing between the clouds in the convective cloud field. The nearest neighbor spacing between clouds has previously been used to study the organization of the cloud field by Weger et al. (1992), Zhu et al. (1992), and Nair et al. (1998). As the nearest neighbor distances are important, this study uses a method based on that of Joseph and Cahalan (1990). While they used the cloud brightness based center of gravity to determine the center of the cloud, this study uses a cloud mask to determine the cloud centers.

To calculate the nearest neighbor spacing, a cloud mask of the domain needs to be produced. The cloud mask is set to 1 if the liquid water specific humidity (q_l) for a single column, with location (a,b) where a is the location along the x direction and b is along the y direction, is greater than 10^{-8} kg kg^{-1} and 0 otherwise. This produces a domain of binary numbers, highlighting the clouds. Figure 5.7 shows the cloud masks at 08:00, 16:00, and 24:00 UTC for NARVAL$_{rad}$ case. Based on these cloud masks the clouds in the domain are numbered, in order to calculate the nearest neighbor spacing. In order to number the clouds, locations where a column with a cloud mask of 1 is directly connected to a second column with a cloud mask of 1 they are classified as being the same cloud.

Following this the cloud centers are determined. This is done by making a temporary assumption that the cloud is a perfect circle, from which the center can be determined. The distances between the center of each cloud and all other clouds in the domain are calculated. Based on all the calculated distances the minimum distance for each cloud is determined. This is defined as being the nearest neighbor spacing for that cloud.

To compute the I_{org} of the cloud field a Cumulative Density Function (CDF) of the nearest neighbor spacings for the clouds in the LES domain is calculated. A second cumulative density function is then calculated based on a randomly distributed cloud field, which follows a Poisson distribution, where the number of clouds and domain size remain the same. The Poisson Cumulative Density Function (CDF_P) is calculated using Equations 5.2 and 5.3:

$$CDF_P = 1 - \exp(-\rho\pi d^2) \tag{5.2}$$

$$\rho = \frac{N}{L^2} \tag{5.3}$$

where d is the nearest neighbor spacing for the randomly distributed cloud field, ρ is the number of clouds normalized by the area of the LES domain, L is the horizontal length of the LES domain, and N is the number of clouds in the domain.

The CDF of the LES nearest neighbor spacings can be directly compared to the CDF_P. The I_{org} value is determined by integrating the area under the curve (Tompkins and Semie, 2017). An I_{org} value greater than 0.5 indicates that the cloud field is clustered. If the value of I_{org} is equal to 0.5, the comparison is along the diagonal line, indicates that the simulated cloud field is randomly distributed. If the I_{org} value is less than 0.5 the cloud field is regularly distributed.

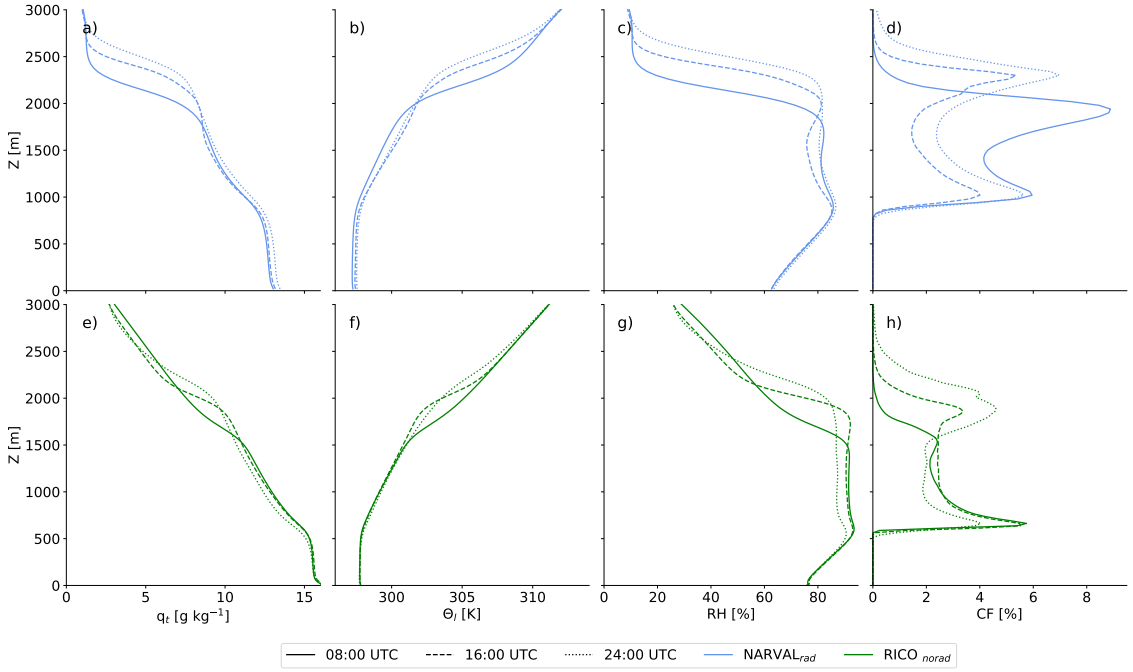

Figure 5.4: The domain averaged profiles for the total specific humidity (q_t) (a and e), the liquid water potential temperature (Θ_l) (b and e), relative humidity (RH) (c and f), and cloud fraction (d and h) for both the NARVAL$_{rad}$ (a - d) and the RICO$_{norad}$ (e - h). The profiles at 08:00 UTC, 16:00 UTC, and 24:00 UTC are shown as the solid line, dashed line, and dotted lines respectively.

5.4 Results

5.4.1 Mean State

In order to investigate the LES's ability to represent the variability in IWV and LWP as observed by HAMP and the degree of organization in the cloud field, it is important to first assess the LES mean vertical structure of the cloudy boundary layer. To this purpose the domain averaged profiles of total specific humidity (q_t), liquid water potential temperature (Θ_l), relative humidity (RH), and cloud fraction (CF) for both the NARVAL$_{rad}$ and RICO$_{norad}$, as seen in Fig. 5.4, are analysed.

While both LES cases feature a vertical structure typical of trade-wind cumulus, some subtle but important differences exist. NARVAL$_{rad}$ has a much drier free troposphere compared to RICO$_{norad}$. A second feature in these profiles is the visually stronger inversion at the top of the boundary layer in the NARVAL$_{rad}$, when compared to RICO$_{norad}$. Related to this there is a significantly stronger humidity jump across the inversion. A third difference between the NARVAL$_{rad}$ and RICO$_{norad}$ is seen in the domain averaged profiles of Θ_l, as seen in Fig. 5.4b) and f). NARVAL$_{rad}$ is cooler throughout the boundary layer compared to the conditions in RICO$_{norad}$. As a result, the boundary layer can contain less water in vapor form, which should be reflected in the IWV. Similar to the profiles of q_t and RH, the inversion in the profiles of Θ_l is visually stronger compared to the inversion in the RICO$_{norad}$.

What both composite cases share, however, is that the boundary layer continuously deepens throughout the simulated 48 hrs.. This is evident by the profiles at 16:00 UTC, represented by the dashed line, and 24:00 UTC, represented by the dotted line, showing deeper boundary layer when compared to the profile at 08:00 UTC, represented by the solid line. The

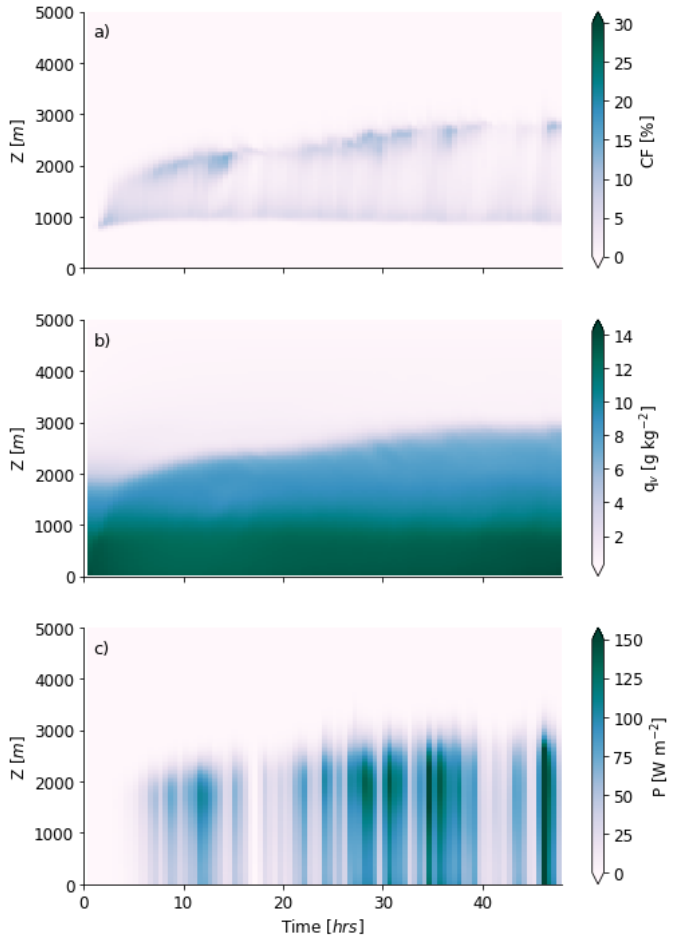

Figure 5.5: Time-height profile of the domain averaged a) specific humidity (q_v), b) CF and c) precipitation flux (P) from the NARVAL$_{rad}$

deepening of the boundary layer is also indicated in the domain averaged CF profiles, in Fig. 5.4d) and h). The CF profiles for both cases also share a double peak, at cloud base and directly below the inversion altitude. At all three time points these two maxima are present at cloud base and cloud top. This double peak in cloud fraction can also be seen in the time-height profiles, as seen in first half of Fig. 5.5a). Another robust feature seen in Fig. 5.5a) is the almost constant cloud base height. While there is very little variation in the height of cloud base, there is a consistent increase in the altitude of the cloud top. This increase in cloud top height can be seen throughout the first 24 hrs of the simulation and continues to develop into the second simulated day, reflecting a boundary layer that is not exactly in equilibrium but is still adjusting slightly to the time-constant forcings. This behavior is a defining feature of the classic RICO case and also shared by the NARVAL$_{rad}$ case.

5.4.2 Time Evolution

This continuous and gradual deepening of the boundary layer is also visible in the time-height profile of specific humidity (q_v), as seen in Fig. 5.5b). At the beginning of the simulation a sharp jump from q_v values of approximately 8 and 9 g kg^{-1} to approximately 2 g kg^{-1} occurs across the trade inversion, which is located at approximately 2000 m. This inversion rises to approximately 3000 m towards the 48:00 UTC mark. The gradual

deepening of the boundary layer is accompanied by an increase in the precipitation flux (P). The value of P varies with time, but in general the maximum intensity occurs around 1500 m. This points towards significant evaporation of precipitation below this height, which results in a cooling of the lower altitudes of the boundary layer. It should also be noted that in a number of cases the peaks in P appear to visibly correlate with the maximums in CF near the inversion, which suggests a potential outflow of cumulus clouds at that height.

The time-series of selected variables, that reflect the cloud related properties, from the NARVAL$_{rad}$ case are shown in Fig. 5.6. The corresponding results from the RICO$_{norad}$ case are included for reference. Figure 5.6a) shows the time-series of P at an altitude of 1500 m, a height that is close to the maximum flux throughout the simulation. At 1500 m the value of P generally varies between 0 and approximately 125 W m^{-2}. Note that in the RICO$_{norad}$ case only six time-points are available. As a result, the temporal variability in P gives the appearance of being smoother than it actually is. This is also true for the other variables shown in Fig. 5.6.

Similarly a difference in the cloud cover, averaged over the entire LES domain, is seen between the two simulations. The RICO$_{norad}$ consistently has a lower cloud cover compared to the NARVAL$_{rad}$, as seen in Fig. 5.6b). During the first 24 hrs the simulated cloud cover in RICO$_{norad}$ begins to increase with time, peaking at 24:00 UTC with a cloud cover of approximately 20 %, however there is a decrease in the cloud cover at the beginning of the second simulated day. The NARVAL$_{rad}$ time-series for cloud cover also indicates relatively similar trend, however it does show significantly more variability. Throughout the 48 hrs NARVAL$_{rad}$ generally has a cloud cover ranging between 20 % and 40 %, which is consistently larger than the RICO$_{norad}$ at corresponding time-steps. This probably reflects the presence of more outflow clouds near the inversion in NARVAL$_{rad}$, as shown in Fig. 5.4d).

While the value of P is more intense and cloudiness more enhanced in NARVAL$_{rad}$ case, there are very little differences between the two simulations in the median LWP time-series, as seen in Fig. 5.6c). For the full 48 hrs both simulations indicate a median LWP below 50 g m^{-2}. Comparing these values to the range of median LWP values obtained from the 27 time-windows of HAMP retrievals, here shown in box-whisker format, it is clear that the LES values are well within the range of retrieved LWP values, with a slight bias towards low LWP values compared to HAMP, which has median LWP values of up to approximately 250 g m^{-2}.

In comparison, Fig. 5.6d) suggests that the simulated range of median IWV values reasonably compares to the range observed by HAMP. Note that the median IWV is continuously increasing during the simulation, which is an artifact of its composite setup. When compared to the RICO$_{norad}$, it is clear that the NARVAL$_{rad}$ has a consistently lower median IWV. This is due to NARVAL being somewhat colder throughout the boundary layer, and therefore it can contain less water in vapor phase.

5.4.3 Spatial Structure

Next the simulated spatial structure of the cloudy boundary layer in NARVAL$_{rad}$ is investigated, starting with the cloud mask at 08:00 UTC, 16:00 UTC, and 24:00 UTC, as shown in Fig. 5.7. What is immediately noticeable is the heterogeneous structure of the projected cloud field, with substantial cloudy areas surrounded by smaller clouds in clearer patches. The substantial clouds represent areas dominated by cumulus outflow near the inversion. The IWV two-dimensional fields were also determined for the corresponding

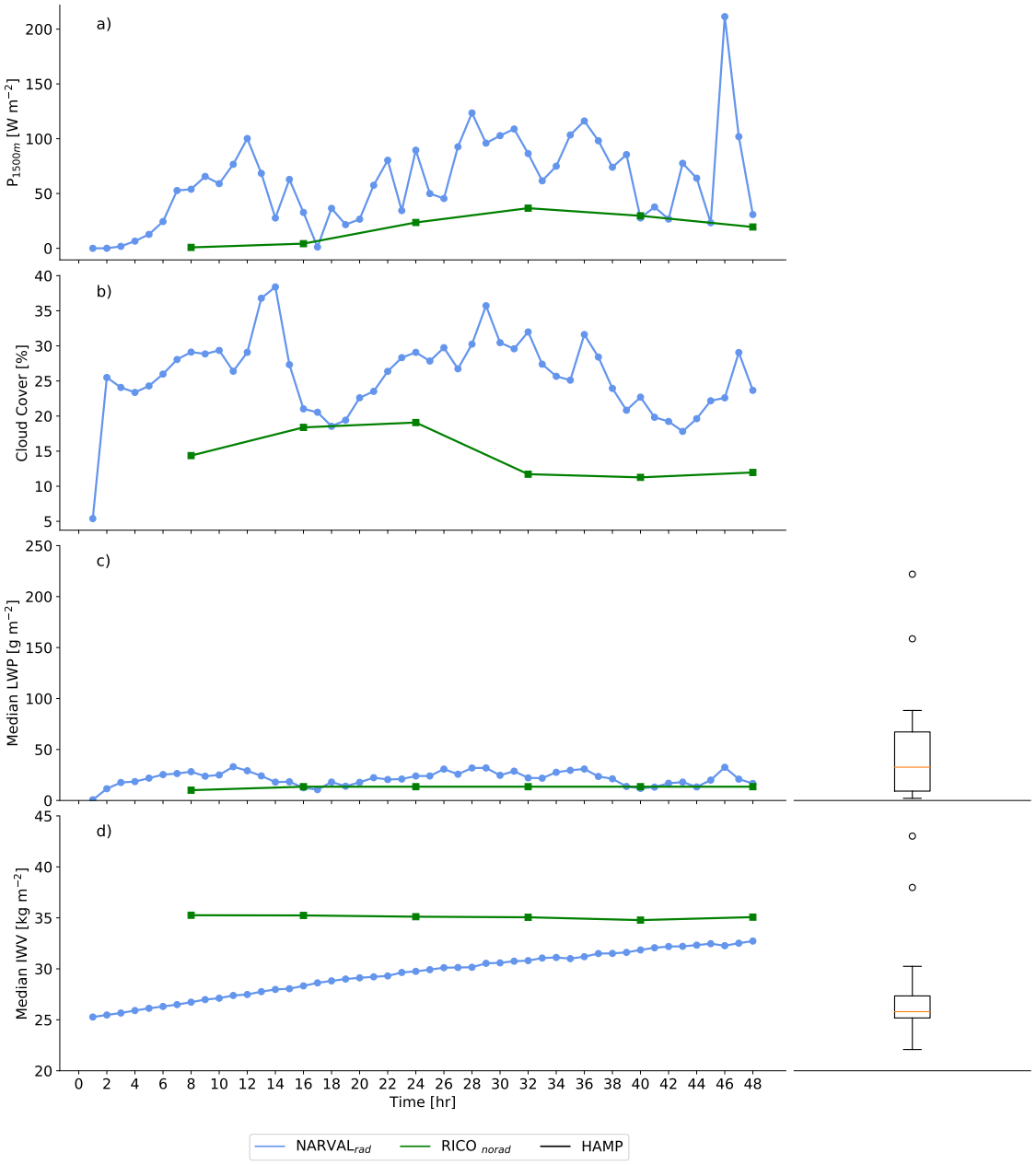

Figure 5.6: Time-series of the a) Precipitation Flux at 1500 m (P_{1500m}), b) CF, c) median LWP, and d) median IWV for NARVAL$_{rad}$ (blue) and RICO$_{norad}$ (green), with the median IWV values and median LWP values from the time-windows in the HAMP retrievals represented by the corresponding box-whisker plots.

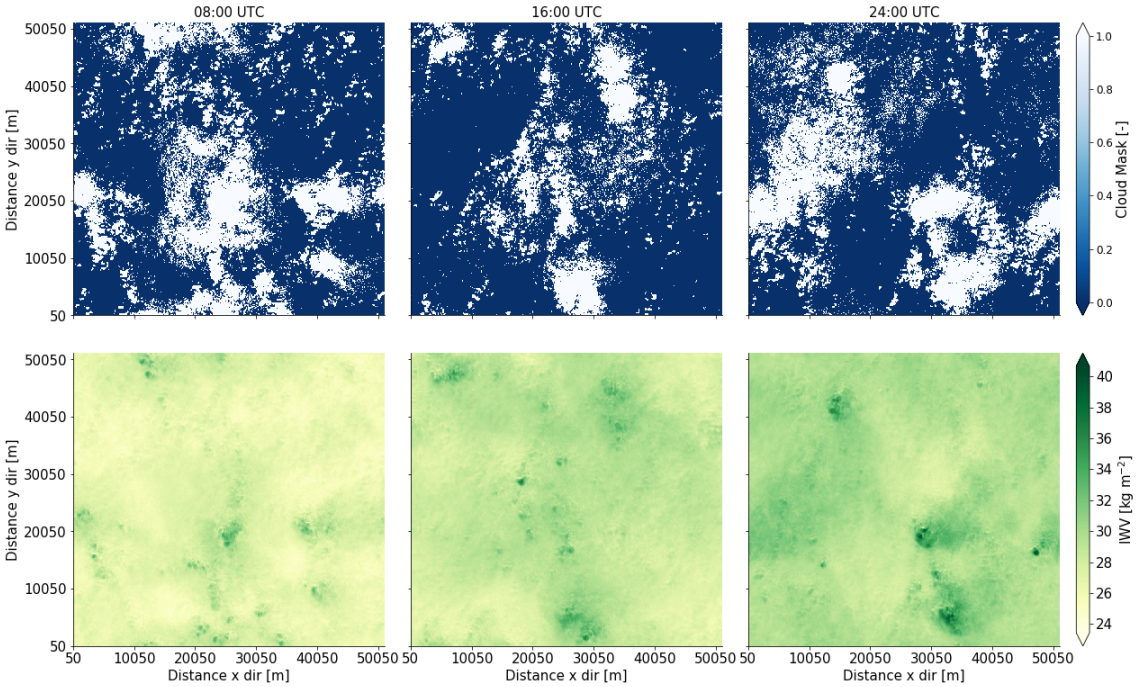

Figure 5.7: The cloud mask is shown for the NARVAL$_{rad}$ at a) 08:00 UTC, b) 16:00 UTC, and c) 24:00 UTC, with the corresponding IWV field shown for d) 08:00 UTC, e) 16:00 UTC, and f) 24:00 UTC.

time-steps to gain insight into the increasing median IWV, as shown in Fig. 5.6d) to f). Cross comparing cloud mask with the IWV field immediately confirms that the clearer areas correspond to relatively low IWV conditions, and vice-versa. The gradual increase in IWV during the simulation, related to the gradual deepening of the boundary layer, is also visible. It seems that difference between the lower and higher IWV values within the field gradually increases with time, which is a manifestation of the increasing degree of spatial organization.

We next address the question to what extent the LES can reproduce the variability in IWV and LWP values as observed in the HAMP retrievals, derived using the method described in Section 5.3.1. In addition, we investigate whether the cloud field organization is connected to this distribution. I$_{org}$ is calculated, following the method described in Section 5.3.2, for the three-dimensional fields in both the NARVAL$_{rad}$ and RICO$_{norad}$ cases. Because the RICO$_{norad}$ case has been used extensively for studying spatial organization with LES (Seifert and Heus, 2013; Neggers et al., 2019), it is used as a reference for interpreting the relationship between the cloud field organization and the variability in IWV and LWP as diagnosed for the NARVAL$_{rad}$ case.

The time-series of the I$_{org}$ values of all time points for which the LES produced a cloud mask are shown in Fig. 5.8a). Initially, during spin-up the NARVAL$_{rad}$ has a regularly distributed cloud field, with an I$_{org}$ increasing from sub-0.5 values to super-0.5 values. This reflects that the cloud field quickly becomes organized. Once the NARVAL$_{rad}$ begins to organize it remains organized for the remainder of the 48 hrs, occasionally fluctuating slightly in the degree of organization. Both the time-development and the amplitude of the degree of organization as expressed by I$_{org}$ is very similar to the RICO$_{norad}$ case.

The time-series of the standard deviation of IWV and LWP (σ_{IWV} and σ_{LWP} respectively) are shown in Fig. 5.8b) and c) respectively. The value of σ_{IWV} increases quickly in value at the beginning of the simulation, but then stabilizes around 1.5 kg m^{-2} for the remainder

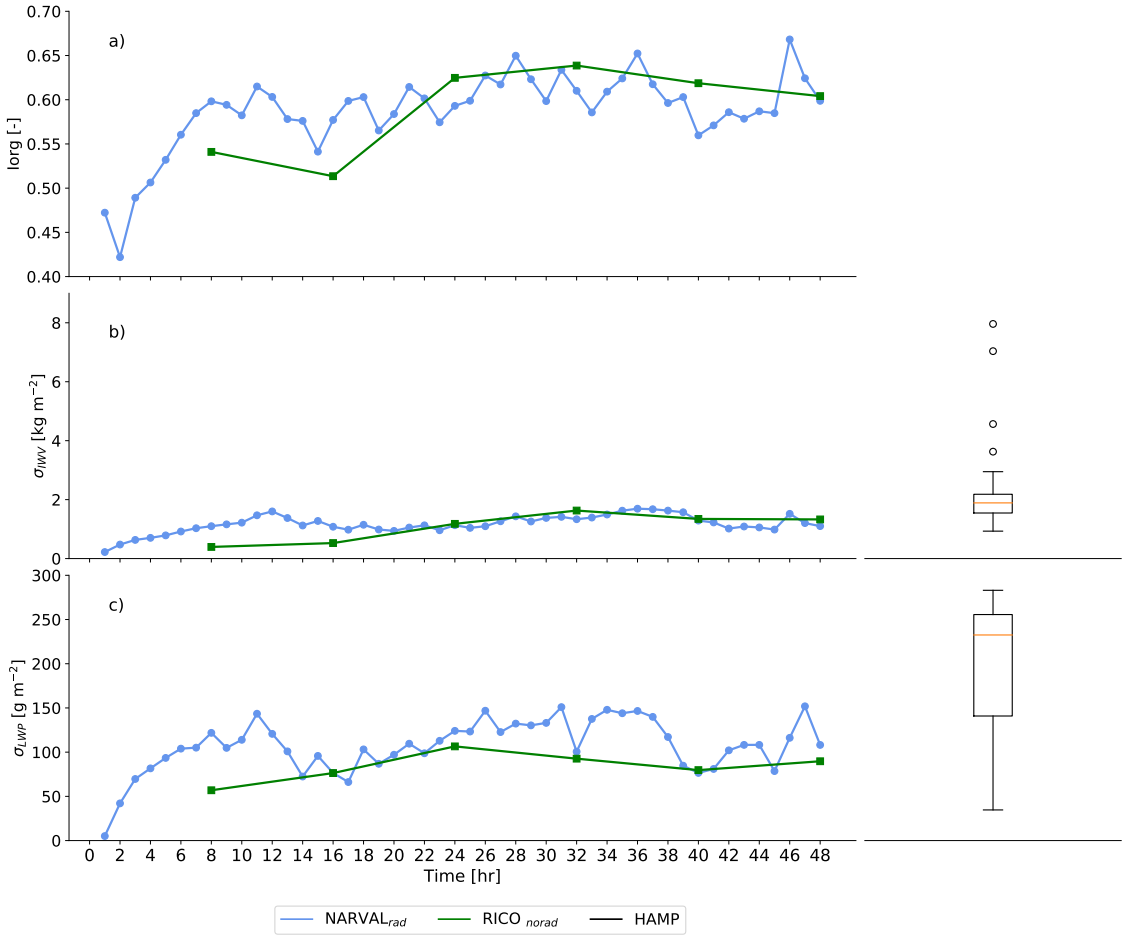

Figure 5.8: Time-series of a) I_{org}, b) σ_{IWV}, and c) σ_{LWP} for the NARVAL$_{rad}$ (blue) and RICO$_{norad}$ (green). The spread in the σ_{IWV} and σ_{LWP} from the HAMP retrievals are represented by the corresponding box-whisker plots.

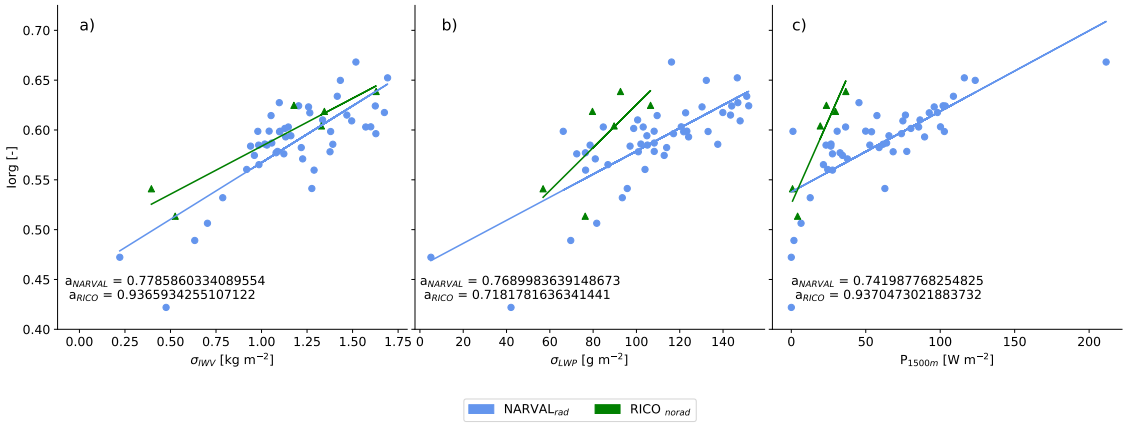

Figure 5.9: Comparison of a) standard deviation of the variance in IWV (σ_{IWV}), b) standard deviation of the variance in LWP (σ_{LWP}), and c) the value of P_{1500m} with respect to I_{org}. The individual time-steps for each simulations are represented with the markers, while the best fit indicates the relationship between the variable and the organization index.

of the simulation. A similar trend can be seen in the time-series for σ_{LWP}. Intercomparing all three panels suggests that for both LES cases and the HAMP retrievals the variability appears to correlate with the I_{org}. A similar trend is also seen in the RICO$_{norad}$ over the course of the 48 hrs.

One of the main objectives of this study is to determine if the LES reproduces the degree of variability as diagnosed from the HAMP retrievals. To this purpose box-whisker plots of the distributions of σ_{IWV} and σ_{LWP} as diagnosed from the HAMP retrievals are included in Fig. 5.8b) and c) respectively. The results indicate that the range of variability covered by LES sits reasonably close to the bulk of the observed distribution, for both variables. The performance of the LES is better for the IWV compared to LWP, for which the LES shows a slight underestimation. Also the LES does not reproduce the strong outlying values for IWV. One shortcoming is that the NARVAL$_{rad}$ cannot capture the very large values of σ_{IWV} that are seen in some of the time-windows of HAMP retrievals. This suggests that while the NARVAL$_{rad}$ does show that there is an increase in the σ_{IWV} is still struggles slightly with with extreme distributions in the σ_{IWV}. Similarly the NARVAL$_{rad}$ can also reproduce values of σ_{LWP} within the range of those determined from the HAMP retrievals. The NARVAL$_{rad}$ however shows a bias towards lower values of σ_{LWP}.

As a result of the visual correlation between the time-series of the variables in Fig. 5.6, it is possible to quantify this correlation, which is shown in Fig. 5.9 by means of scatterplots and linear regression. Apart from σ_{IWV} and σ_{LWP}, the correlation of P at 1500 m (P_{1500m}) with Iorg is also calculated. The correlation between the σ_{IWV} and the I_{org} is significant in both NARVAL$_{rad}$ and RICO$_{norad}$, with a relatively similar slope. A significant correlation also exists between σ_{LWP} and I_{org} in both LES cases. The slope of the dependency in σ_{LWP} and I_{org} is quite different between the NARVAL$_{rad}$ and RICO$_{norad}$ cases. This confirms the visual indication of a relationship between the values of σ_{IWV}, and σ_{LWP}, and the degree of organization, that was seen in the time-series. Finally, the value of I_{org} is also compared to the value of P_{1500m} for each time-step. A correlation also exists, in both simulations, between the value of P_{1500m} and I_{org}. The difference in the slope for this correlation between P_{1500m} and I_{org}, between the NARVAL$_{rad}$ and RICO$_{norad}$ cases, are even larger compared to the slopes for the σ_{IWV}, and σ_{LWP}, correlations. Previous studies have indicated a relationship between the precipitation in the domain and the degree

of organization. The results from the two LES cases presented confirm the relationship between the precipitation and the degree of organization.

To summarize, the large domain LES shows a relatively good ability in representing the variability in IWV and LWP from the HAMP retrievals, however it still struggles with large variability in both variables. The slopes from the quantitative comparison indicate that the correlation between some variables and the I_{org} are very case dependent, e.g. the cloud-related variables such as LWP and the value of P_{1500m}, while for others it is not, e.g. for IWV. This information that the case dependence is strongest for these cloud-related variables suggests that the cloud structure between the $NARVAL_{rad}$ and the $RICO_{norad}$ cases is responsible. In particular the difference in the presence of outflow clouds near the inversion between the two LES cases, $NARVAL_{rad}$ case contains more outflow clouds compared to the $RICO_{norad}$ case, as suggested by the domain-averaged profiles in Fig. 5.4d) and h).

5.5 Sensitivity Studies

In this section two sets of additional simulations are discussed that are designed to give additional insight into the results obtained. A total of four new simulations are discussed in order to perform these two sets of sensitivity studies. The first tests the impact of the domain size on the results, while the second investigates the impact of the radiative transfer.

5.5.1 Domain Size

Three additional simulations of the $NARVAL_{rad}$ case were performed at different domain sizes, as part of the domain size sensitivity study. The four versions of the $NARVAL_{rad}$ case thus cover a set of domain sizes $L \in \{6.4, 12.8, 25.6, 51.2\}$ km, referred to as L6.4, L12.8, L25.6, while the domain size of 51.2 km^2 is the $NARVAL_{rad}$ from earlier. The simulations generated on the smaller domains were only run over a 24 hr period.

The time-series of key properties for all four experiments are shown in Fig. 5.10, with the mean values over the last 12 hrs of the day for each simulation seen in the corresponding scatterplots. During the spin up, there are very few differences in the cloud cover (CC) within the domain between the simulations, as seen in Fig. 5.10a). The differences in CC between the simulations begin after around 10:00 UTC. During the simulated day the range of values in cloud cover between the simulations generally vary between 20 % and 35 %. This range of cloud cover values increases into the night, ranging between 20 % and approximately 55 % towards 24:00 UTC. This increase in the range values is primarily a result of the significant increase in cloud cover in the Sim 6.4 km^2, which peaks at 24:00 UTC.

A similar divergence between the simulations is seen in the value of P_{1500m}, as seen in Fig. 5.10b). For this variable the divergence between the simulations begins much earlier in the day even during spin up. This difference persists throughout the simulation with the $NARVAL_{rad}$ and L25.6 cases having peaks in the values of P_{1500m} towards the end of the day, with values reaching approximately 90 W m^{-2}. In comparison the L6.4 and L12.8 cases which have much lower values of P_{1500m}, peaking at approximately 10 W m^{-2}. This increase in P_{1500m} with increasing domain size is also indicated by the mean P_{1500m} over second half of the day, as shown in Fig. 5.10f).

Having an understanding of the divergence in the atmospheric conditions between the different domain sizes can also help with understanding potential differences in the variability

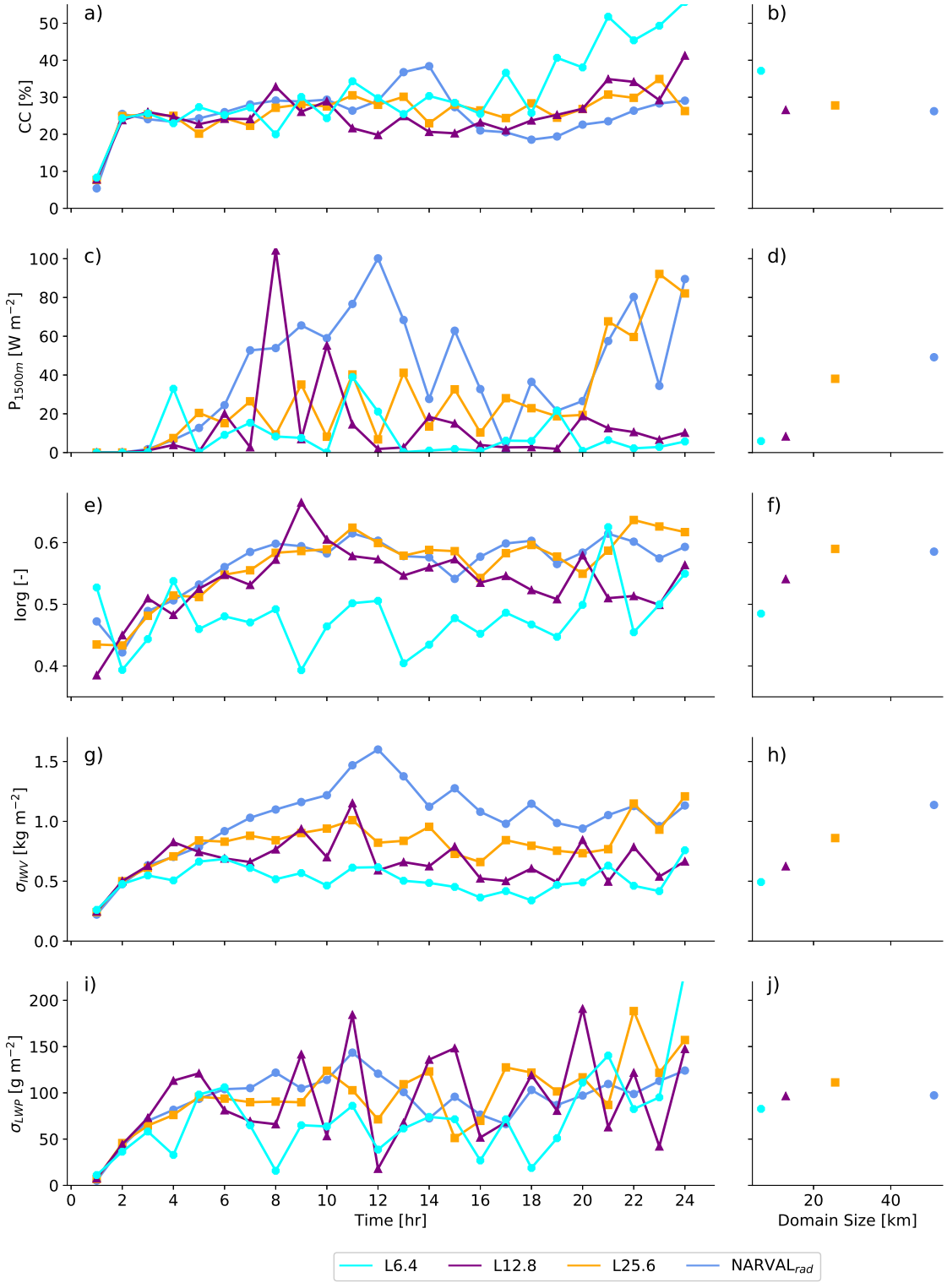

Figure 5.10: Time-series and corresponging mean values over the second 12 hrs of a) and b) Cloud Cover (CC), c) and d) P_{1500m}, e) and f) I_{org}, g) and h) σ_{IWV}, and i) and j) σ_{LWP} for the NARVAL$_{rad}$ (blue), and the three simulations generated for the two domain size simulation 25.6 km^2 (yellow), 12.8 km^2 (purple), and 6.4 km^2 (light blue)

in IWV and LWP, and the degree of organization. In order to investigate this in more detail the time-series of I_{org} is shown in Fig. 5.10e). The time-series of the L6.4 case indicates an I_{org} that remains almost consistently below 0.5. This indicates that an LES with a domain of size L6.4 is too small for organization to develop. The degree of organization begins to increase with increasing domain size, with values increasing to above 0.5 in the L12.8 case. For the two largest cases, the L28.6 and NARVAL$_{rad}$, the values of I_{org} begin to converge towards values of approximately 0.6. The mean values of I_{org} over the second half of the day, shown in Fig. 5.10f), highlight the convergence between the two larger domain cases.

The time-series of σ_{IWV} shows a similar stratification, with the smallest domain having the smallest variability in IWV. Similar to the time-series of I_{org}, the value of σ_{IWV} in the L6.4 case is consistently lower compared to the larger domain simulations. The mean σ_{IWV}, as shown in Fig. 5.10h), shows an increase in σ_{IWV} with increasing domain size. A slight convergence towards larger values of σ_{IWV} is seen between the two larger domain size simulations.

In comparison, there are very few differences in the value of σ_{LWP} between each of the domain size simulations. The value of σ_{LWP} for all simulations are quite variable throughout the 24 hrs, as shown in Fig. 5.10i). By calculating the mean σ_{LWP}, over the second half of the day, it is confirmed that there are very few differences between the different domain sizes, with all four simulations having a mean value around 100 g m^{-2}. This suggests that the LES domain size does not play a significant role on the variability in LWP.

To summarize, these results suggest that both I_{org} and σ_{IWV} are highly dependent on the size of the LES domain, with both variables increasing in value with increasing domain size. The mean variability in LWP indicates that σ_{LWP} is not as highly dependent on the domain size. Similar to the value of σ_{LWP}, the mean CC is not significantly dependent on the domain size, with only the L6.4 case having a higher mean CC in the second half of the day. In comparison, the value of P_{1500m} does show a high dependence on the domain size, with increasing P_{1500m} with increasing domain size.

5.5.2 Radiation

The impact of radiation is investigated, by performing one additional NARVAL experiment in which the radiation was completely switched off for the duration of the simulation. As a consequence the diurnal cycle, driven by radiative forcings also completely disappears. This simulation is labeled NARVAL$_{norad}$.

Figure 5.11, the domain and temporally averaged profiles of CF give a first indication of the impact of radiation on the simulations. While both cases have two local maxima in CF at cloud base and cloud top, however the magnitude of the CF is significantly different between the two simulations. In both simulations the local maxima at the cloud base are at similar altitudes with the NARVAL$_{rad}$ case having a larger magnitude in CF compared to the NARVAL$_{norad}$ case. The most significant difference between the two simulations is located at the cloud top, both in the location and the magnitude. The difference in the magnitude between the peak in CF at cloud top in NARVAL$_{rad}$ is almost 5 % larger compared to the peak of just over 2 % in the NARVAL$_{norad}$ case. The altitude of this peak in CF, in NARVAL$_{norad}$, is also almost 1000 m below the altitude of the NARVAL$_{rad}$ case, which indicates a significant impact on the cloud layer depth as a result of the radiation. The same also applies to P_{1500m}, except that for this variable the impact is stronger, shifting the median from approximately 55 W m^{-2} to 10 W m^{-2}. Given the strong reduction in the second peak in CF near the inversion, shown in Fig. 5.11, it is speculated that the absence of radiative cooling at the cloud top harms the formation of cumulus outflow structures, which produce a significant fraction of the precipitation flux in this regime.

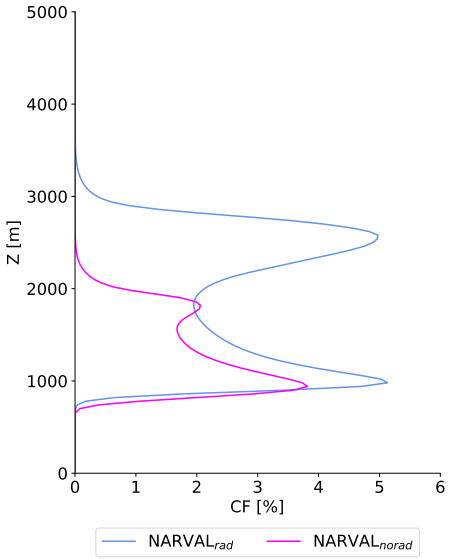

Figure 5.11: Domain averaged profile of cloud fraction (CF), averaged over the second 24 hours simulated, NARVAL$_{rad}$ (blue) and NARVAL$_{norad}$ (magenta)

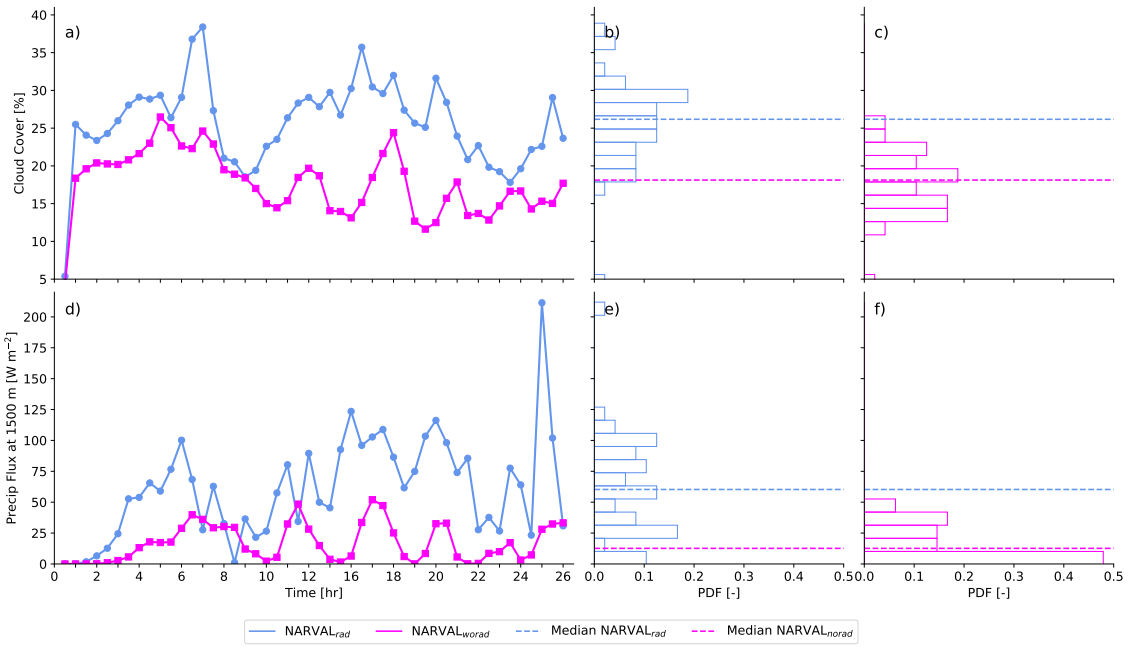

Figure 5.12: Time-series of a) Cloud Cover and b) Prec Flux at 1500m for the NARVAL$_{rad}$ (blue) and NARVAL$_{norad}$ (magenta) with the corresponding PDFs for b) and e) NARVAL$_{rad}$ and c) and f) NARVAL$_{norad}$

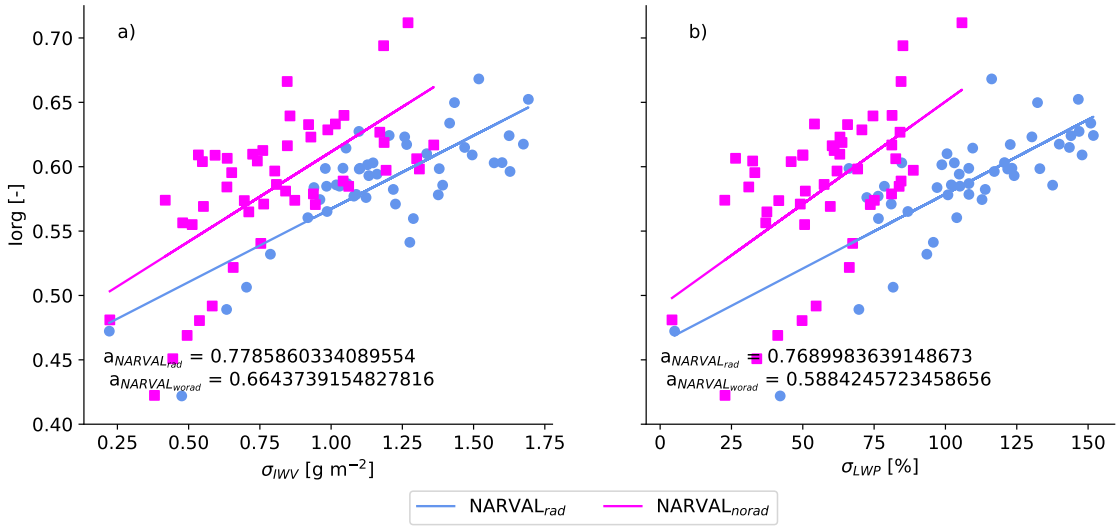

Figure 5.13: Comparison of a) σ_{IWV} and b) σ_{LWP} with respect to the I_{org} for the NARVAL$_{rad}$ (blue) and the NARVAL$_{norad}$ (magenta) for the 48 hrs simulated.

The question then remains how the absence of radiation and the associated impacts on the cloud boundary layer translate to the values of σ_{IWV}, σ_{LWP}, and I_{org}. To this purpose scatterplots of σ_{IWV} and σ_{LWP} against I_{org} are shown for both NARVAL$_{rad}$ and NARVAL$_{norad}$. In both the NARVAL$_{rad}$ and NARVAL$_{norad}$ simulations there is significant correlation between both values for σ_{IWV}, and σ_{LWP}, and the I_{org} values, as shown in Fig. 5.13. However, as seen from the correlation coefficient in Fig. 5.13 there is a weakening in the correlation when the radiation is switched off. The slopes of the dependencies in both variables are larger in the NARVAL$_{norad}$ compared to the NARVAL$_{rad}$ simulation. This mainly results from the NARVAL$_{norad}$ having lower values of σ_{IWV} and σ_{LWP} compared to the NARVAL$_{rad}$ case, while the values of I_{org} remains relatively similar between the two simulations. The trend of the NARVAL$_{norad}$ slope of the dependency in these variables is relatively similar to that of the RICO$_{norad}$, that was shown in Fig. 5.9.

5.6 Discussion

The NARVAL$_{rad}$ case indicates that the variability in IWV and LWP, as observed in the HAMP retrievals, can be reproduced to a reasonable degree in large-eddy simulations that are 50 km^2 or greater in the horizontal extent. This suggests that it is not completely required to run simulations that cover the entire tropical and subtropical Atlantic to investigate the spatial organization of shallow cumulus. This is encouraging, particularly in relation to the ongoing Elucidating the role of clouds-circulation coupling in climate (EUREC^{4}A) campaign (Bony et al., 2017) and the modeling work corresponding to it.

Significant correlations are found between the three metrics that were defined for determining the variability in IWV and LWP, and the degree of spatial organization. The use of the RICO$_{norad}$ case is beneficial in that spatial organization had previously been noted in the simulation by Seifert and Heus (2013) and more recently by Neggers et al. (2019). There are some noticeable differences in the correlations between the variability in IWV, and LWP, and I_{org} between the two simulations. The slopes in the comparisons between σ_{IWV}, and σ_{LWP}, compared to I_{org} differ, with the slope suggesting whether the correlation is case dependent or independent. In the case of the σ_{IWV} comparison with I_{org} there are

very few differences between the two cases, while for the comparison between the cloud-related variables and the I_{org} there is a high dependence on whether it is the NARVAL$_{rad}$ case or the RICO$_{norad}$ case.

When tested, the domain size suggests an impact on the correlation between σ_{IWV}, and σ_{LWP}, with the I_{org}. This is particularly noted for the L6.4 case which struggles to organize due to its very limited domain size. The larger domains begin to converge towards an I_{org} of 0.6, with very little differences between the L25.6 and NARVAL$_{rad}$ cases. A corresponding impact is also seen in the σ_{IWV} values which increase with increasing domain size, while less of an impact is seen in σ_{LWP}.

When tested, the radiation indicates a significant impact on the vertical structure of the clouds layer, with significantly less clouds present, and the cloud top located at a lower altitude found in the NARVAL$_{norad}$ case compared to the NARVAL$_{rad}$ case. The radiation also has an impact on the correlations between the cloud-related variables and the I_{org}. The resulting slopes suggest that the NARVAL$_{norad}$ case is actually closer to the RICO$_{norad}$ case. There is a potential connection between this impact on the cloud layer and the recent classification of trade-wind clouds, which divide the clouds into flowers, fish, or gravel (Stevens et al., 2019b; Bony et al., 2020). For the NARVAL$_{rad}$ case the cloud fields, shown in Fig. 5.7, indicate a flower structure which are usually associated with outflow clouds and generally tend to have a high amount of precipitation. Once the radiation is switched off this cloud field shifts from a mainly flower dominated cloud field towards a cloud field dominated by gravel like cloud structures. This result has similarities to the RICO$_{norad}$ case, the cloud field for which is shown in Fig. 1 of Neggers et al. (2019).

A second important result found, when the radiation was switched off, was in the correlation between the variability in LWP, and the value of I_{org}. The slopes of the dependency for the cloud-related variables in these comparisons indicated that the NARVAL$_{norad}$ shows a similar trend to the RICO$_{norad}$ case. However it is interesting to note that in the NARVAL$_{norad}$ there is no significant change in the value of I_{org}. The correlation between the variability in IWV and I_{org} does not change significantly between the NARVAL$_{rad}$ and NARVAL$_{norad}$ cases. This would suggest that the I_{org} mainly reflects the horizontal water vapor distribution. This is particularly interesting as the I_{org} is determined from the cloud population.

There are still a number of shortcomings however. While NARVAL$_{rad}$ does capture values of σ_{IWV} similar to a majority of the 27 time-windows from the HAMP retrievals, there are still values of σ_{IWV} for some HAMP time-windows that the NARVAL$_{rad}$case does not capture. This would indicate that the while the NARVAL$_{rad}$ case is representative for the lower σ_{IWV}, it still struggles with large distributions of IWV.

5.7 Conclusions

This study focused on determining whether a large domain LES is required to capture a range of σ_{IWV} and σ_{LWP} values that were retrieved using the HAMP instrument during the 4^{th} research flight of the NARVAL South Campaign. A second aim was to investigate whether there is a relation between the increase in σ_{IWV} and the degree of organization in the cloud field. A simulation based on the RICO campaign, with a relatively similar model setup, is also used as a proxy case for a cloud field that organizes.

The main results of this study are briefly summarized:

- Dividing the time-series of the HAMP IWV and LWP retrievals into 27 time-windows gives a range of σ_{IWV} and σ_{LWP} that are representative of research flight 4.

- The NARVAL$_{rad}$ shows good ability in reproducing σ_{IWV} and σ_{LWP} values in the range of those retrieved by HAMP, however a struggle with very large values remains.
- By quantifying the correlation between the σ_{IWV}, and σ_{LWP}, and I$_{org}$ values, in both the NARVAL$_{rad}$ and the RICO$_{norad}$, it is confirmed that there is a relation between the variability in IWV, and LWP, and the degree of organization.
- A similar relation is also seen in the correlation between P$_{1500m}$ and I$_{org}$ in both simulations, however it is noted that the value P$_{1500m}$ is very limited in the RICO$_{norad}$ case compared to the NARVAL$_{rad}$ case.
- The reduction in P$_{1500m}$ in the RICO$_{norad}$ is potentially related to the gravel like classification of the cloud field in the RICO$_{norad}$ case, while the cloud field in the NARVAL$_{rad}$ case is more flower like as a result of increased amounts of outflow clouds, which can produce more precipitation.
- These results suggest that not only do the clouds have different structures but that the I$_{org}$ is predominantly controlled by the water vapor distribution as opposed to the liquid water distribution.
- The vertical structure of the CF profile in the NARVAL$_{norad}$ case indicates a similar classification, with significantly lower amounts of outflow clouds below the inversion.
- This potentially explains the significantly lower values of P$_{1500m}$ in the NARVAL$_{norad}$ case compared to the NARVAL$_{rad}$ case, indicating that the radiative cooling at the cloud top, that is present in the NARVAL$_{rad}$, plays an important role in the development of the cumulus outflow structures.
- Similar to the NARVAL$_{rad}$ case, the NARVAL$_{norad}$ also shows a correlation between σ_{IWV}, and σ_{LWP}, and the value of I$_{org}$, however based on the slopes of the dependency it is suggested that the NARVAL$_{norad}$ case is more similar to the RICO$_{norad}$ case. There is little impact to the value of I$_{org}$ in the NARVAL$_{norad}$ case compared to the NARVAL$_{rad}$ case, which is also similar to the RICO$_{norad}$ case.
- While the domain size test does also show a correlation between σ_{IWV} and I$_{org}$, there is a very clear impact as a result of the domain size, particularly for the small domain. The L6.4 struggles to organize due to its very small horizontal extent, while there is a convergence between the larger domain simulations with very little differences seen between the L25.6 and NARVAL$_{rad}$ cases.

Chapter 6

Using elevated moisture layers to study the fast boundary layer responses to climate perturbations

Abstract

The uncertainties in the responses of boundary layer clouds to a change in climate make up one of the largest uncertainties in climate projections using general circulation models (GCMs). This is primarily related to the parameterization required in GCMs to represent boundary layer processes and clouds as the coarse resolution of the GCMs is larger than the horizontal extent of cumulus clouds. Therefore high resolution models such as large-eddy simulation (LES) models, which require less parameterizations, have been used in several studies to simulate potential future climates. In most studies perturbations in sea surface temperature or an increase the concentration of CO_2 are added to the simulation setup to indicate a potential future climate. This study makes use of elevated moisture layers (EMLs) to investigate the fast response of boundary layer clouds to a change in climate. These EMLs are based on an EML observed during research flight 4 of the first Next Generation Aircraft Remote-sensing for Validation (NARVAL) campaign. A composite case, identical to the L25.6 study in Chapter 5, is setup as a control simulation, with an additional 5 simulations generated where the depth of the EML perturbation is varied. The presence of an EML has a direct impact on the magnitude and depth of the cloud layer within the boundary layer, while the the development of a convective layer is also indicated above the boundary layer. Within the boundary layer the largest impact is in the cloud layer depth and magnitude of the cloud fraction. An impact in the radiative fluxes are also indicated, particularly at altitudes above the boundary layer. Therefore it is suggested that the boundary layer acts as a buffer where the impact of the water vapor on the longwave radiation is reduced. This study makes use the cloud radiative effect at the top of the cloud layer in order determine whether the boundary layer clouds, produced in response to the EML, have a warming or cooling effect on the boundary layer. Initial results indicate that with increasing EML depth, the boundary layer clouds have a positive cloud feedback, which corresponds to a warming of the boundary layer.

6.1 Introduction

One of the largest questions in climate science is how boundary layer clouds respond to a changing climate. The uncertainty in the response of boundary layer clouds corresponds to

one of largest uncertainties in climate projections (Bony and Dufresne, 2005; Boucher et al., 2013; Vial et al., 2013; Blossey et al., 2016; Tan et al., 2016). This particularly applies to marine boundary layer clouds in the tropical and subtropical regions (Tan et al., 2017). This uncertainty is predominantly related to the use of general circulation models (GCMs) to simulate projected climates. As marine boundary layer clouds are generally spatially smaller than the horizontal resolution of GCMs parameterizations are required in order to represent the processes involved in the boundary layer (Bretherton, 2015; Myers and Norris, 2016; Vogel et al., 2016). While the resolution in the GCMs has been significantly increased and the parameterizations updated, there are still a number of shortcomings such that the uncertainty in the cloud feedback remains (Bretherton, 2015).

Several solutions have been suggested in order to tackle these shortcomings in GCM simulations. These solutions include using observations of clouds in order to predict how they will respond to a change in the climate. Observations from recent field campaigns, such as the first and second Next Generation Aircraft Remote-sensing for Validation (NARVAL) campaigns, NARVAL1 and NARVAL2, and the ongoing Elucidating the Role of Clouds-Circulation Coupling in Climate (EUREC^{4}A) campaign, provide information to help with understanding the different processes that control the cloud fraction. It was planned that a second research aircraft, during the EUREC^{4}A field campaign, would have a backscatter lidar and a radar mounted on the plane, which would fly just above the altitude of the cloud base in an effort gain an understanding of the processes at cloud base. The measurements from the EUREC^{4}A campaign aims to give an insight into how convection and the large-scale environment have an impact on the cloud feedbacks (Bony et al., 2017).

Additional solutions that have been suggested involve using high resolution models such as large-eddy simulation (LES) models or single-column models (SCMs) in order to gain an understanding of the cloud feedback (Klein et al., 2017). The use of these high resolution models means that the model has the ability to resolve boundary layer clouds. An added benefit of using LESis that they are known to be able reproduce realistic realizations of boundary layer clouds. While it is still not practical to use LES on large temporal and spatial climatological simulations, they can give an insight into feedbacks on small temporal and spatial scales (Bretherton, 2015). Numerous studies have been conducted on how boundary layer clouds will respond to climate change using a variety of different models and methods. Tan et al. (2017) summarized that a majority of current studies using LES to investigate the response of boundary layer clouds to climate change use one of three methods: i) a perturbation of temperature profiles in the troposphere based on a prescribed sea surface temperature, ii) an increase in sea surface temperature, or iii) an increase in the concentration of carbon dioxide (CO_2). Additionally several intercomparisons have focused on investigating the feedback of clouds to these potential climate perturbations in LES models, for example the Cloud Feedback Model Intercomparison Project (CFMIP) and the CFMIP/GASS Intercomparison of Large-Eddy and Single-Column Models (CGILS).

Perturbations in the concentration of CO_2 have been investigated in several studies using different magnitudes of CO_2 and different models. These include to name a few a doubling of the CO_2 concentrations in CFMIP models (Zelinka et al., 2012), quadrupling of CO_2 concentration in the Icosahedral Non-hydrostatic global climate model (ICON-GCM) and ICON large-eddy model (ICON-LEM) (Nam et al., 2018), and a quadrupling the CO_2 concentrationin the LES models from CGILS (Blossey et al., 2016) study. A number of these studies have also investigated the corresponding change in the upper troposphere, while keeping the ocean heat flux constant (Tan et al., 2017).

Additional studies, like for example those by Bretherton et al. (2013) and Bretherton and Blossey (2014) also included investigations on the impact of changes to humidity, subsidence, wind-speed, warming in the free troposphere, and increases in the sea surface

temperature to name a few. The increasing of the sea surface temperature is a common method used to represent a changing climate in models. Studies such as Bretherton and Blossey (2014) and Bellon and Geoffroy (2016) describe simulations in which the the sea surface temperature is increased as proxy cases for future climates. In the case of the sea surface temperature study in Bretherton and Blossey (2014) a warming is applied throughout the atmosphere with the relative humidity held constant. An intercomparison of the sensitivity of boundary layer clouds to an increase in sea surface temperature was conducted by Blossey et al. (2013) at three different locations, as part of the CGILS project.

A number of shortcomings do remain in the use of observations and LESs to investigate the responses of boundary layer clouds to climate change. Observational campaigns, designed to gain detailed information on the cloud processes generally take place over a relatively short time period, which is not long enough to represent the changes in the climate. Similarly simulations generated using LES models also have a relatively short temporal extent due to their high computational costs.

This study proposes the use of elevated moisture layers (EMLs) as a proxy for a future warming in the free troposphere. An example of an EML was observed during the 4^{th} research flight of the first Next Generation Aircraft Remote-sensing for Validation (NARVAL) campaign. To this purpose, a composite of the large-scale forcings representing the flight path of research flight 4 are used to initialize and force the LES. The general structure of this observed EML is used to inform the configuration of the simulations generated as part of this study. The study aims to investigate the fast response of boundary layer clouds to the presence of an EML, using the Dutch Atmospheric Large-Eddy Simulation Model (DALES). In the case of this study the total cloud radiative effect at the top of the cloud layer is used to quantify the response of the boundary layer clouds to the EML.

The model and the GCM dataset used to initialize DALES are introduced in Section 6.2, with a detailed description of the different simulations built for this study given in Section 6.3. Section 6.4 details the analysis of the results, comparing the atmospheric conditions in the different simulations, the response in the radiative fluxes and boundary layer clouds due to EMLs, and finally the response of these clouds in the form of the total cloud radiative effect. Finally, Sections 6.5 and 6.6 summarize and describes the main conclusions of this study.

6.2 Datasets

6.2.1 NARVAL Observations

The use of an EML as a proxy for a future climate is based on the presence of EMLs in nature. The 4^{th} research flight from the first NARVAL campaign observed one of these EMLs. The profiles from the 11 dropsondes that were launched during the 4^{th} research flight, shown in Fig. 6.1, provide an insight into the elevated moisture layer that was observed throughout the flight. This EML is particularly evident in the profiles of the water vapor specific humidity (q_v) and the relative humidity (RH), shown in Fig. 6.1b) and c), where there are peaks in both variables in the free troposphere above the boundary layer. These peaks are generally decoupled from the boundary layer, with the presence of a dry layer between the boundary layer and the EML.

The range of altitudes of this EML vary during the flight, occurring at around 12 km throughout the middle section of the flight, and at a lower altitude of around 8 km in the region of Barbados where a deep convective system was observed (Stevens et al., 2016). The different upper limits of the profiles are a result of the altitude at which the aircraft

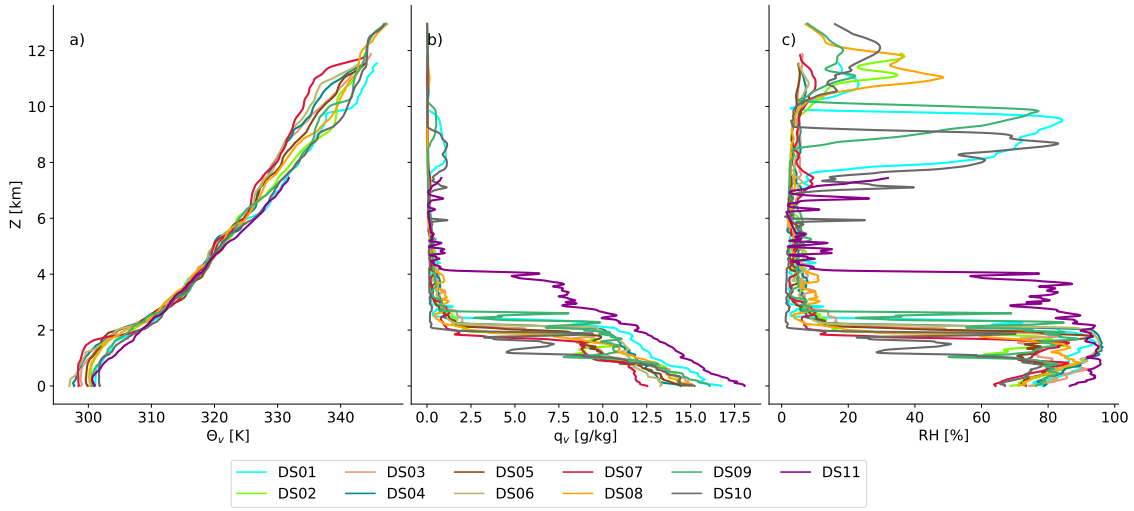

Figure 6.1: The profiles of a) virtual potential temperature (Θ_v), b) water vapor specific humidity (q_v), c) relative humidity (RH), for each dropsonde launched during research flight 4 of the first NARVAL Campaign, similar to Fig. 4.2.

was flying when the dropsonde was released, with the most significant difference occurring in the profiles for the 11^{th} dropsonde which was launched just before the aircraft landed.

6.2.2 LES Model Description

This study makes use of DALES to generate high resolution simulations at the location of research flight 4 during the NARVAL campaign (Klepp et al., 2014). DALES is setup on an Eulerian domain of size 25.6 x 25.6 x 7.02 km^3, with a horizontal resolution of 100 m and a vertical resolution of 40 m. Similar to the DALES setup, as described in Chapter 4 and 5 the horizontal advection on the large-scale is prescribed in each of the prognostic variables. The interactive fluxes at the surface and the sea surface temperature is also prescribed for these simulations. While the geostrophic forcing used for the wind in DALES is derived from the large-scale pressure field based on the GCM dataset. For this study DALES employs a Seifert-Beheng two-moment bulk microphysics scheme, as described in Seifert and Beheng (2005), along with an interactive radiative scheme.

Nudging used in this study follows that described in Neggers et al. (2012); van Laar et al. (2019) and Reilly et al. (2019) however in this case it is limited to altitudes from 3 km to the ceiling of the LES domain at 7.02 km. The nudging is applied at a time-scale of 1 hr in order to constrain the EML to the free atmosphere. Below 3 km where nudging is not implemented the boundary layer is free to develop throughout the day.

6.2.3 Composite Large-Scale Forcings

DALES is initialized and forced using a large-scale forcings that are based on GCM profiles from the European Center for Medium Range Weather Forecasts' (ECMWF) Integrated Forecasting System (IFS) used in Reilly et al. (2019). The large-scale profiles that are used to initialize and force DALES in this study are identical to the composite forcings used in Chapter 5, the profiles for which are shown in Fig. 5.2. These composite forcings are based on the mean large scale forcings over the locations of dropsondes 2 to 10 during the flight. This study makes use of these composite forcings to ensure that there would not

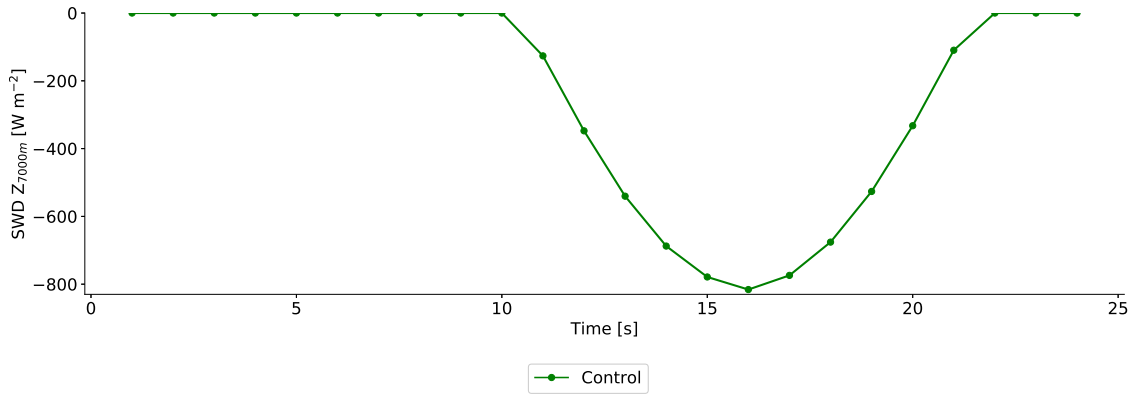

Figure 6.2: Time-series of the prescribed downward shortwave radiation (SWD) at the ceiling of the LES (Z_{7000m}) for the Control simulation

be an impact as a result of the region of deep convection that was seen in the region of Barbados that day.

6.3 Experiment Configuration

Two main sets of simulations are built as part of this study. These include a control simulation and a set of simulations with an elevated moisture layer included above the boundary layer.

6.3.1 Control Experiment

A single control simulation, referred to as Control, was nudged directly toward the composite large-scale forcing profiles, and is identical to the 25.6 km^2 domain simulation studied in Chapter 5. While the nudging was primarily included for the EML simulations, it is also applied to the Control in order to limit the differences between the Control and the set of EML simulations. Control was initialized at 00:00 UTC and run for a total of 24 hrs.

The time-series of the downward shortwave radiative flux (SWD) at the ceiling of the Control simulation gives an insight into the prescribed shortwave radiative flux for the simulations. The time-series confirms that the incoming shortwave radiation only begins to have an impact after 10:00 UTC, before peaking at 16:00 UTC, and decreasing as the sun begins to set. This prescribed incoming shortwave radiation at the LES ceiling remains constant throughout all the simulations.

6.3.2 Elevated Moisture Layer Simulation

A second set of simulations was generated with a similar setup to Control. These simulations were also initialized at 00:00 UTC and run for 24 hrs. The only difference between Control and the set of EMLs is the inclusion of a moisture layer above the boundary layer. A total of five simulations were generated as part of the EML study. The depths of the EMLs were set to 200 m, 400 m, 600 m, 800 m, and 1000 m, referred to as EML_{200m}, EML_{400m}, EML_{600m}, EML_{800m}, and EML_{1000m}.

The strength of the EML was determined based on the domain averaged saturated specific water content, defined as the maximum amount of water vapor at a given temperature and

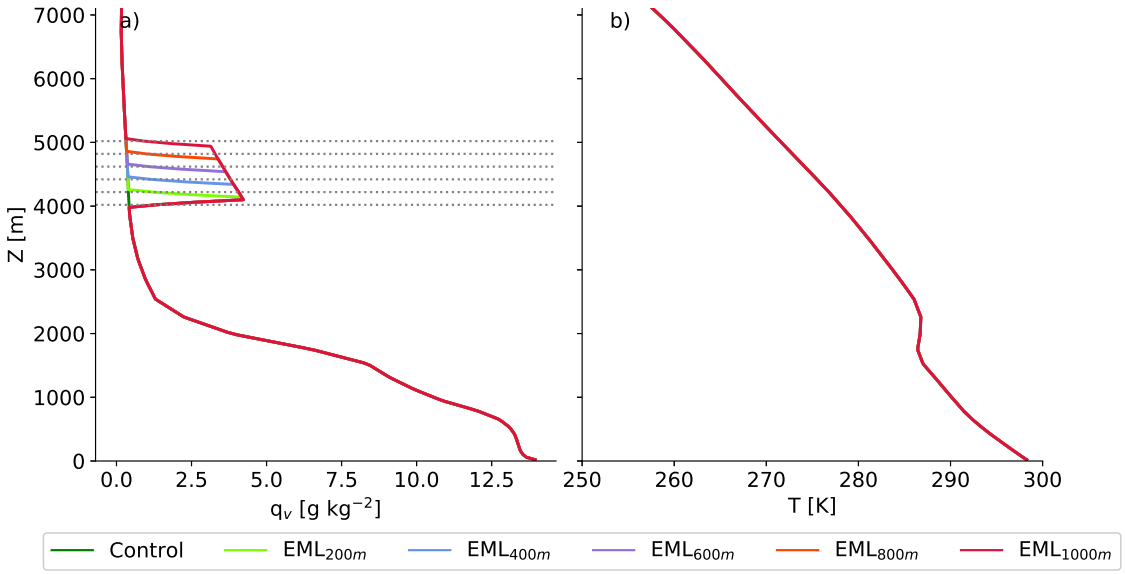

Figure 6.3: The large-scale forcing profiles of a) specific humidity (q_v) and b) temperature (T) for Control (green), EML$_{200m}$ (light green), EML$_{400m}$ (blue), EML$_{600m}$ (purple), EML$_{800m}$ (orange), EML$_{1000m}$ (red). The EML basee and individual tops are shown by the dotted lines.

pressure, profile from the first time-step of Control. The maximum magnitude of the EML was set to be 50 % of the saturated specific water content. This maximum was set in order to reduce the potential of clouds being produced within or at the top of the EML.

In order to avoid convection as a result of a sudden increase in humidity at an elevated altitude, a staggered increase in humidity is implemented. This staggering of the increased humidity is done by first calculating 15 % of the saturated specific water content at 4020 m, then increasing to 30 % of the saturated specific water content at 4060 m, before finally reaching the 50 % saturated specific water content at 4100 m. The humidity layer is consistently increased to 50 % of the saturated specific water content across all vertical level in the EML up until the altitude of the second last vertical level of the EML. To avoid a sudden decrease in the level of humidity at the top of the EML, a staggered decrease in strength is applied using the same format as at cloud base.

An insight into the staggering of the strength of the EML at the base and top can be seen in the large-scale forcing profiles in Fig. 6.3. To emphasis that the only changes made to the setup of the EML simulations is in the humidity, the temperature (T) profile for all simulations are shown to be identical in Fig. 6.3b).

6.4 Results

6.4.1 Vertical Structure

Before analyzing the impacts of the inclusion of an EML in the forcing data, it is important to gain an understanding of the atmospheric conditions seen in Control. To that purpose the domain averaged profiles of liquid water potential temperature (Θ_l), total specific humidity (q_t) and cloud fraction (CF) are shown in Fig. 6.4. Profiles at 06:00 UTC, 12:00 UTC, 18:00 UTC, and 24:00 UTC provides an insight into the atmospheric conditions develop throughout the day. This development of the boundary layer is based on the

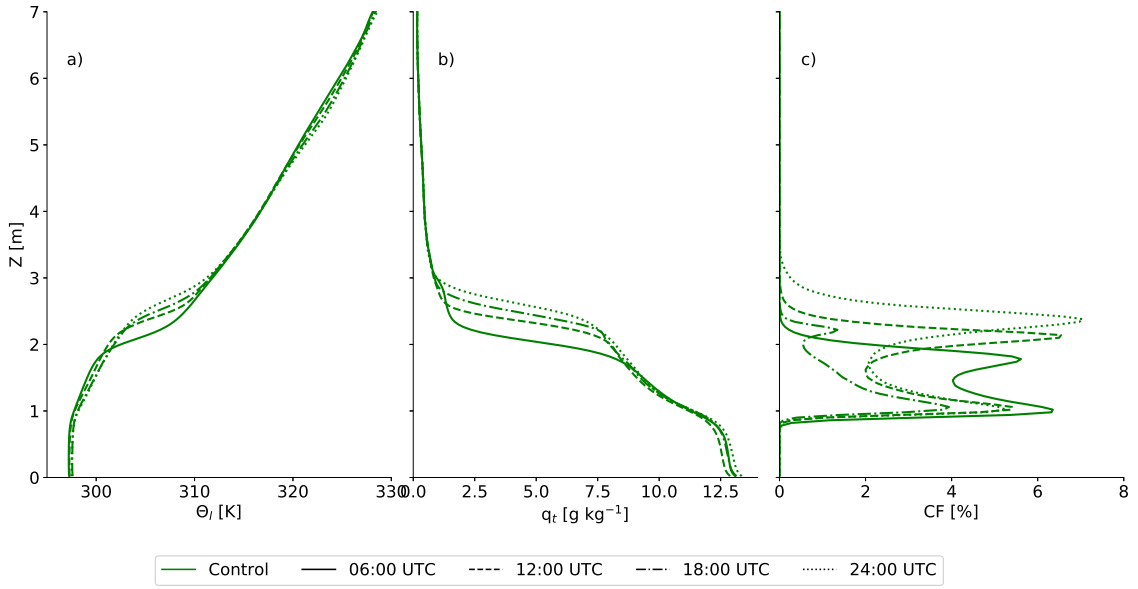

Figure 6.4: The domain averaged profiles of a) liquid water potential temperature (Θ_l), b) total specific humidity (q_t), and c) Cloud Fraction (CF) at 06:00 UTC (solid line), 12:00 UTC (dashed line), 18:00 UTC (dashed and dotted line), and 24:00 UTC (dotted line) for Control

increase in altitude of the height of the visible inversion throughout the day, particularly in the q_t and RH profiles in Fig. 6.4b) and c). The altitude of the inversion increases from approximately 2000 m at 06:00 UTC to 2700 m at 24:00 UTC. The increasing altitude of the inversion is also indicated in the CF profiles with the with the altitude of cloud top increasing throughout the day. A common feature that is consistent throughout the day is the presence of two peaks in CF, one at cloud top and one at cloud base. This suggests the presence of outflow clouds at the boundary layer inversion.

Having an understanding of the atmospheric conditions in the Control is useful for gaining an insight into the impact of the EML on the atmospheric conditions. In order to investigate this impact the Control and EML domain averaged profiles of Θ_l, q_t, relative humidity (RH), and CF, temporally averaged over the last 6 hrs of the simulation, are shown in Fig. 6.5. The domain averaged profiles do indicate that there are some similarities between the Control and each of the EML simulations. These similarities include a similar structure of the boundary layer, with only small differences in the values q_t and RH close to the surface. The double peak in CF, previously noted in the Control, is also present in each of the EML simulations, with some variation in the magnitude of these peaks. This suggests that the main impact in the boundary layer, as a result of the EML, is in the CF.

There are also several additional differences between the Control and EML simulations indicated in the domain averaged profiles. The most significant differences occur at altitudes above the boundary layer. The presence of the EML is very clearly defined in the profiles of q_t and RH, shown in Fig. 6.5b) and c) respectively, where the increase in the humidity is evident over a range of altitudes from just below 4 km to just below 6 km. The magnitude of this humidity increase and depth of this range of altitudes is highly dependent on the depth of the EML, with both increasing with deeper EMLs.

Within this range of altitudes the EML is also seen to have an impact on the Θ_l profiles, with the value of Θ_l remaining constant throughout the layer. Similar to the q_t and RH profiles, the depth of this layer and the constant value of Θ_l are highly dependent on the depth of the EML, with the EML_{1000m} maintaining a constant Θ_l of approximately

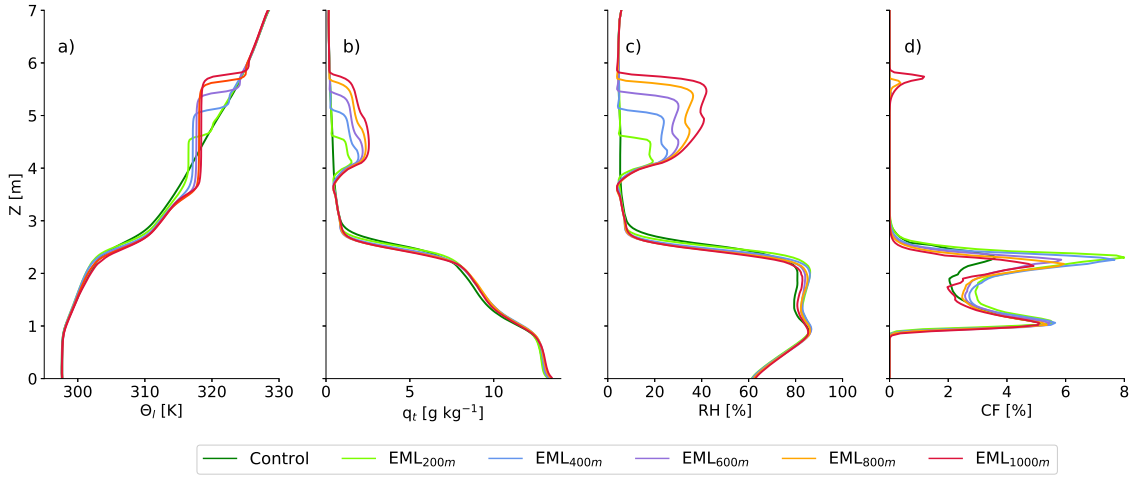

Figure 6.5: The domain averaged profiles averaged over 6 hrs from 18:00 UTC to 24:00 UTC for a) Θ_l, b) q_t c) relative humidity (RH), and d) CF for the Control (green) EML_{200m} (light green), EML_{400m} (blue), EML_{600m} (purple), EML_{800m} (orange), and EML_{1000m} (red).

319 K over an approximately 2 km layer while the EML_{200m} has a constant Θ_l of around 315 K over a 600 m layer. This constant value of Θ_l over several vertical levels suggests the presence of a dry turbulent layer, above the boundary layer, which allows for the production of convection within the EML. These profiles are significantly different to those for the Control which shows a constant increase in Θ_l with with increasing altitude, while the humidity values decrease to indicate very dry conditions above the boundary layer.

6.4.2 Time Evolution

While there is only a small impact of EML on the value q_t at the surface, as indicated from the profiles in Fig. 6.5b), there is a significant impact on the latent heat flux (F_q) over those 6 hrs. This impact of the EML on F_q towards the end of the day is indicated in the time-series of the sensible and latent heat flux at the surface are shown in Fig. 6.6. The time-series of the latent heat flux, shown in Fig. 6.6a), indicates a significant impact as a result of the depth of the EML. This impact is primarily related to the slightly higher values of q_t at the surface and the slightly reduced altitude of the inversion, as a result of increased EML depth. This decrease in F_q is also noted in a study by Rieck et al. (2012) where there is a strong decrease in F_q with increasing strength of the climate perturbation. It should be noted that the differences in the magnitude of the decrease in F_q, between the two studies, can be explained by the methods used for climate perturbation. In the study by Rieck et al. (2012) the perturbed climate is applied to the full atmospheric profiles, while in this study it is only applied to a layer above the boundary layer. As there is limited impact on the temperature profiles within the boundary layer, there is little difference in the latent heat flux, as seen in Fig. 6.6a).

The sensible and latent heat fluxes are important for the development of the convection in the boundary layer and thus important for the development of the marine boundary clouds. To gain an insight into whether the impact, seen in the domain averaged profiles of CF, is consistent throughout the simulation a time height profile of the CF for the Control and each of EML simulations is shown in Fig. 6.7. The time height profiles do indicate that the two peaks in the CF, at cloud base and cloud top, are present in all simulations. It should be noted that the magnitude of the CF varies quite significantly throughout the

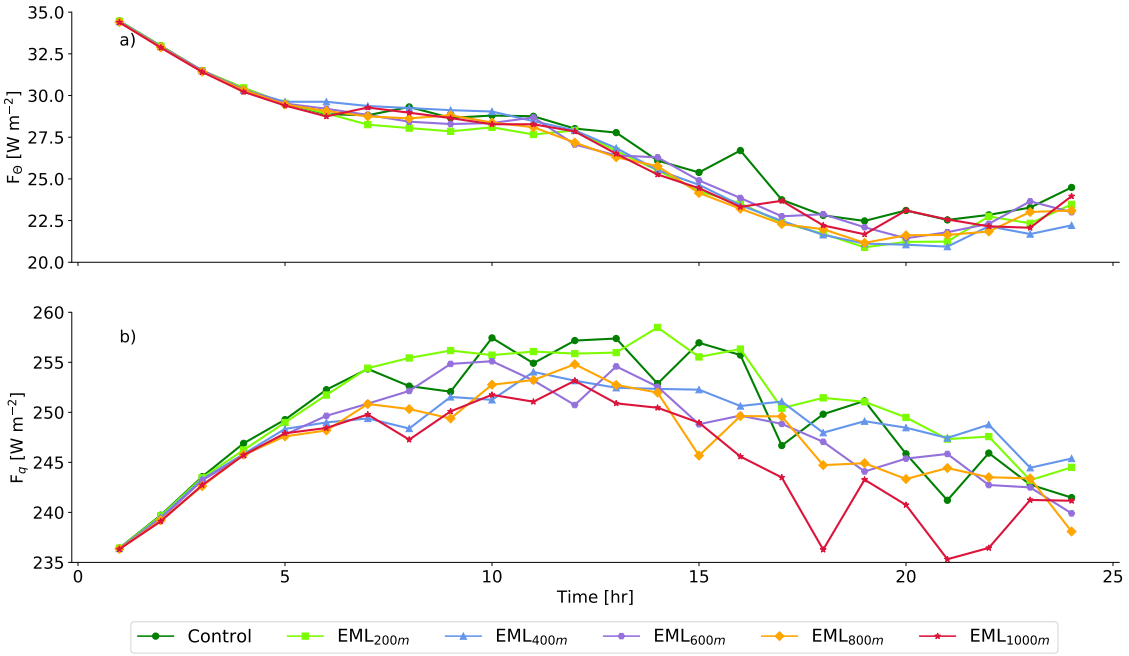

Figure 6.6: Time-series of the a) Latent Heat Flux (F_Θ) and b) Sensible Heat Flux (F_q) at the surface for Control (green), EML_{200m} (light green), EML_{400m} (blue), EML_{600m} (purple), EML_{800m} (orange), EML_{1000m} (red).

simulated day, and also across the different simulations.

As this CF has an impact on the Earth's radiation budget it is important to understand the resulting changes in the radiative fluxes. To this purpose, a time-series of the upward shortwave (SWU) radiative flux and downward longwave (LWD) radiative flux at three altitudes are shown in Fig. 6.8 and Fig. 6.9 respectively. These three altitudes represent the radiative fluxes at the surface (Z_{20m}), at an altitude between the boundary layer and the EML (Z_{3500m}), and at the LES ceiling (Z_{7000m}). The time-series of the SWU radiative flux indicates that the EML has a limited impact at the surface, with the larger impacts occurring at 3500 m and at the ceiling of the LES. At these higher altitudes it is suggested that the less shortwave radiation is being reflected above the boundary layer in the Control compared to the EML simulations. This suggests that the EML simulations would have a cooling effect as more shortwave radiation is reflected.

The time-series of the LWD radiative flux indicates that the largest impact, as a result of the EML, is in the altitudes below the EML. While the LWD radiative flux appears to be extremely variable at the LES ceiling, it should be noted that the values only vary over a range of around 2 W m^{-2}. In comparison the time-series of the LWD radiative flux at 20 m (LWD Z_{20m}) and at 3500m (LWD Z_{3500m}) have a much larger impact. At the surface the LWD radiative flux indicates that with the presence of an EML the magnitude of the LWD Z_{20m} increases, with a difference of almost 10 W m^{-2} between the Control and EML_{800m}. This difference in magnitude increases at 3500m. Throughout the day the EML simulations have a significantly larger magnitude of LWD radiative flux compared to the control, with the magnitude increasing with increasing EML depth. This would suggest that with increased EML depth there is an increase in the absorption and reflection of the longwave radiation by the EML. The resulting increase in the magnitude of the LWD radiative flux indicates a warming of the boundary layer as a result of the EML.

The time-series of both the upward shortwave radiative flux and the downward longwave radiative flux indicate strong temporal fluctuations, which are potentially due to the limited

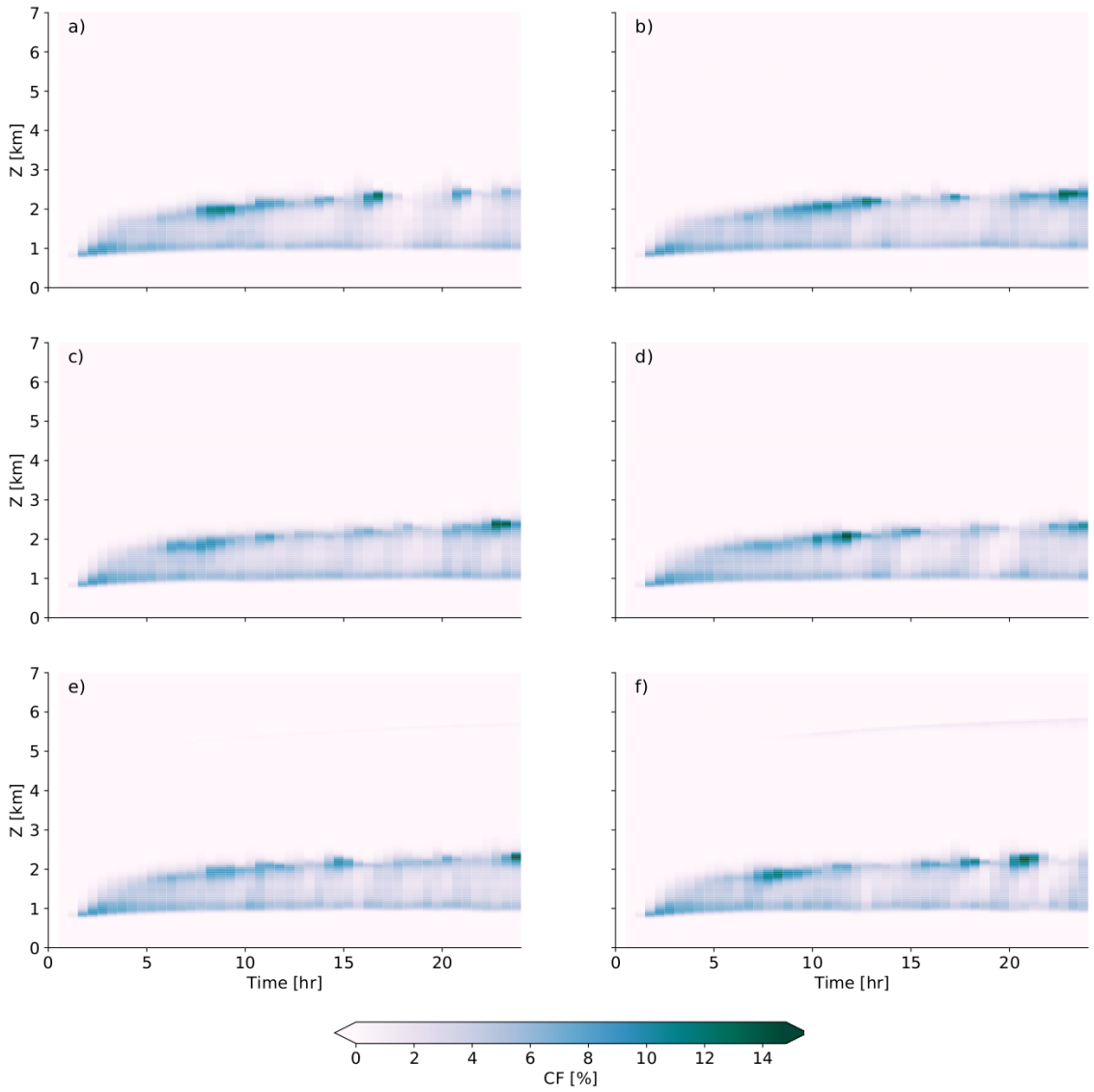

Figure 6.7: Time-height contour plots of CF for a) Control, b) EML_{200m}, c) EML_{400m}, d) EML_{600m}, e) EML_{800m}, f) EML_{1000m}.

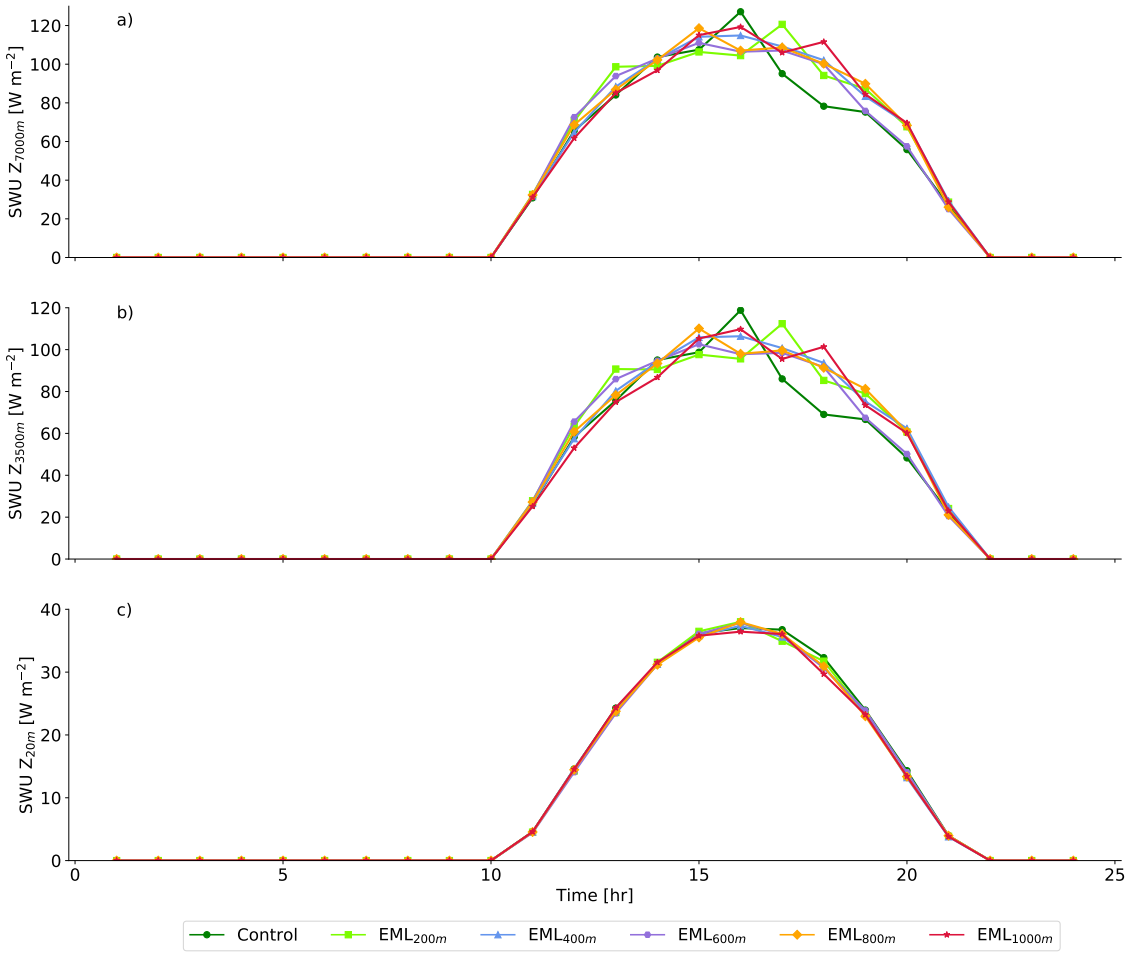

Figure 6.8: Time-series of the domain averaged SWU radiative flux at a) 7000 m (SWU Z_{7000m}), b) at 3500 m (SWU Z_{3500m}), and c) at 20 m (SWU Z_{20m}) Control (green), EML_{200m} (light green), EML_{400m} (blue), EML_{600m} (purple), EML_{800m} (orange), EML_{1000m} (red).

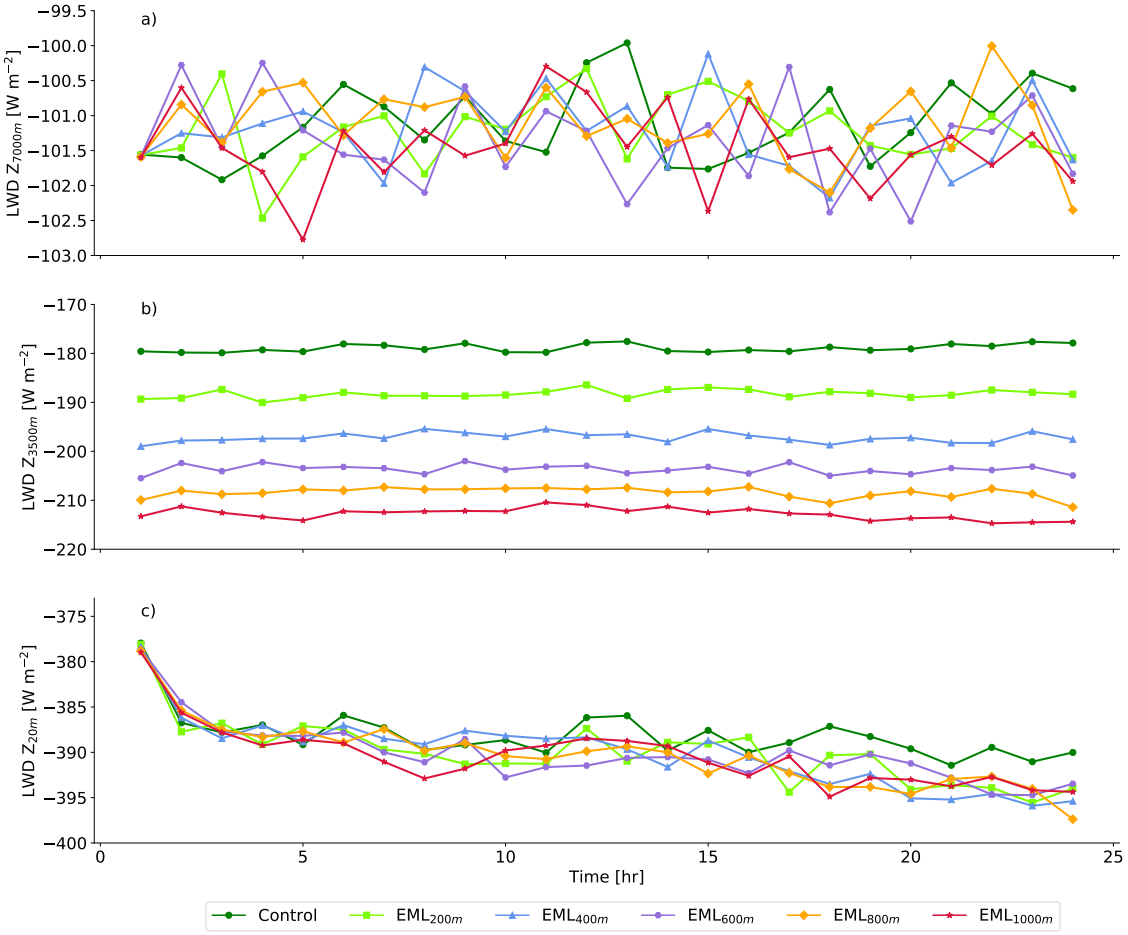

Figure 6.9: Time-series of the domain averaged LWD radiative flux a) at 7000 m (LWD Z_{7000m}), b) at 3500 m (LWD Z_{3500m}), and c) at 20 m (LWD Z_{20m}) for Control (green), EML_{200m} (light green), EML_{400m} (blue), EML_{600m} (purple), EML_{800m} (orange), EML_{1000m} (red).

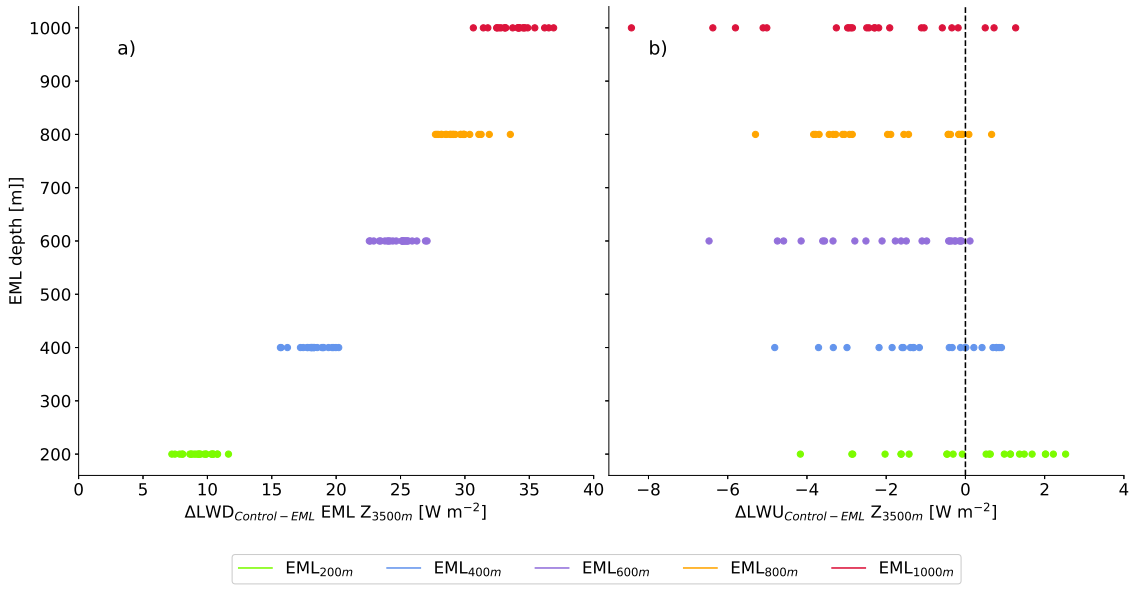

Figure 6.10: Direct comparison between the differences between the Control and EML simulations in the a) upward longwave radiation and b) downward longwave radiation at 3500 m and the depth of the EML.

domain size used for this study. This motivates the use of averaging over time for analyzing the cloud and radiative impacts in the following sections. To this purpose, the average is taken for the last 6 hrs of the simulated day, from 18:00 UTC to 24:00 UTC, during which the simulations is in an almost steady state. This also eliminates the impact of spin-up in the simulation.

6.4.3 Radiative Impacts

In order to quantify the largest impact in the LWD radiative flux occurring in the time-series at 3500 m, as a result of the EML, the difference between the LWD radiative flux at 3500 m in the Control and each of the EML simulations is derived ($\Delta\text{LWD}_{Control-EML}$). A scatterplot comparing the values of $\Delta\text{LWD}_{Control-EML}$ to the corresponding EML depth is shown in Fig. 6.10a). It should be noted that as the LWD radiative flux is negative in value, a positive $\Delta\text{LWD}_{Control-EML}$ indicates a stronger magnitude in the EML simulation compared to the Control. The comparison further confirms that the magnitude of the LWD radiative flux at 3500 m is consistently larger in the EML simulations compared to the Control, and increases exponentially with increasing EML depth.

On the other hand when the difference in the LWU Z_{3500m} between the Control and the EML simulations at 3500 m ($\Delta\text{LWU}_{Control-EML}$ Z_{3500m}) is derived and compared to the EML depth, the impact not as significant, as shown in Fig. 6.10b). In the case of $\Delta\text{LWU}_{Control-EML}$, a negative value indicates a stronger magnitude in the EML LWU radiative flux, while a positive value would indicate a stronger magnitude in the Control LWU radiative flux. The main differences between the different EML depths is in the variability of the $\Delta\text{LWU}_{Control-EML}$ values, with the EML_{1000m} presenting the largest spread.

In order to investigate the impact of the EML on the full radiative flux profiles, the domain averaged profiles, temporally averaged over the second half of the day, are shown in Fig. 6.11. The impact on the radiative fluxes, as a result of the EML tends to vary in the vertical extent and magnitude depending on whether the radiative flux is shortwave or

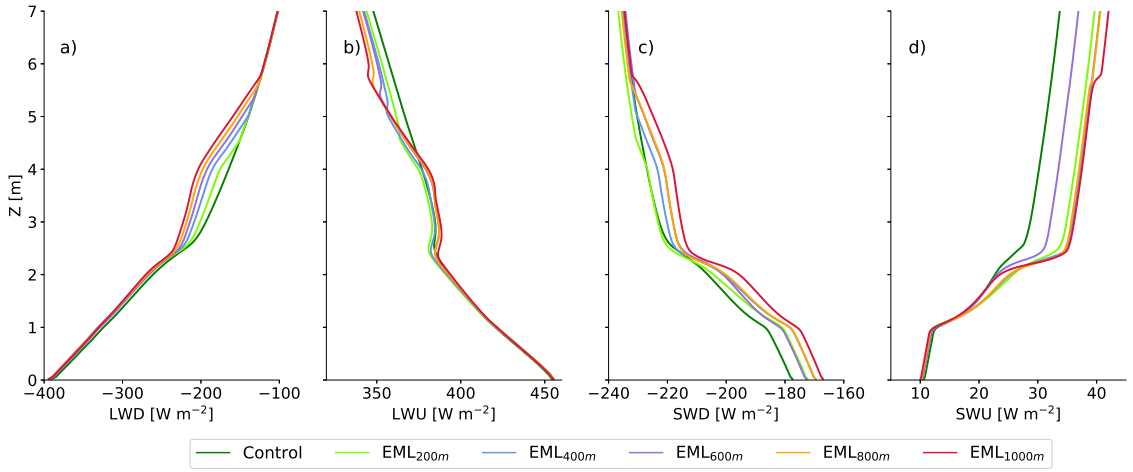

Figure 6.11: The domain-averaged profiles for a) LWD radiative flux b) LWU radiative flux, c) SWD radiative flux, and d) SWU radiative flux, temporally averaged over the final 6 hrs of the simulation, for Control (green), EML$_{200m}$ (light green), EML$_{400m}$ (blue), EML$_{600m}$ (purple), EML$_{800m}$ (orange), EML$_{1000m}$ (red).

longwave and whether it is in the upward or downward direction. In general the domain averaged profiles of the radiative flux do indicate that the region of the free troposphere between the boundary layer and the EML consistently has a large impact as a result of the EML. This is in particular contrast to the impact on the radiative fluxes near the surface where there are very small differences between the simulations, with the exception of the SWD radiative flux, where the maximum difference between the simulations is around 5 W m^{-2}. This would suggest that the boundary layer produces a buffering effect, which reduces the strong direct impact of the water vapor on the longwave radiative flux.

6.4.4 Impact of Changes in Radiation on the Cloud Cover

It has long been understood that clouds have an impact on the radiation budget, which also has a corresponding impact on the clouds present. It is therefore important to first have an understanding of the impact the EML on the radiative fluxes before being able to attempt to answer the question posed in this study, which was determine the response of clouds to a change in the climate using EMLs as potential proxy cases. The domain averaged profiles of CF, seen in Fig. 6.5, have already suggested that the presence of an EML has an impact on the CF throughout the atmosphere. In order to understand this impact additional comparisons of the CF and the downward longwave radiation are required.

To this purpose the mean LWD radiative flux at the peak in CF just below the inversion, is compared to the mean CF at the corresponding altitude, as shown in Fig. 6.12a). From this comparison it is indicated while there is not a significant difference in the mean CF between each of the EML simulations there is a clear increase in the magnitude of the LWD radiative flux, with values ranging from around -237 W m^{-2} in the Control case to -257 W m^{-2} in the EML$_{1000m}$ case. This confirms the results from LWD radiative flux domain averaged profiles in Fig. 6.11 and the time-series of the LWD$_{3500m}$ radiative flux in Fig. 6.9b), which further indicates an absorption and refection of longwave radiation in the EML.

While it is helpful to have an insight into the relation between the CF and the downward

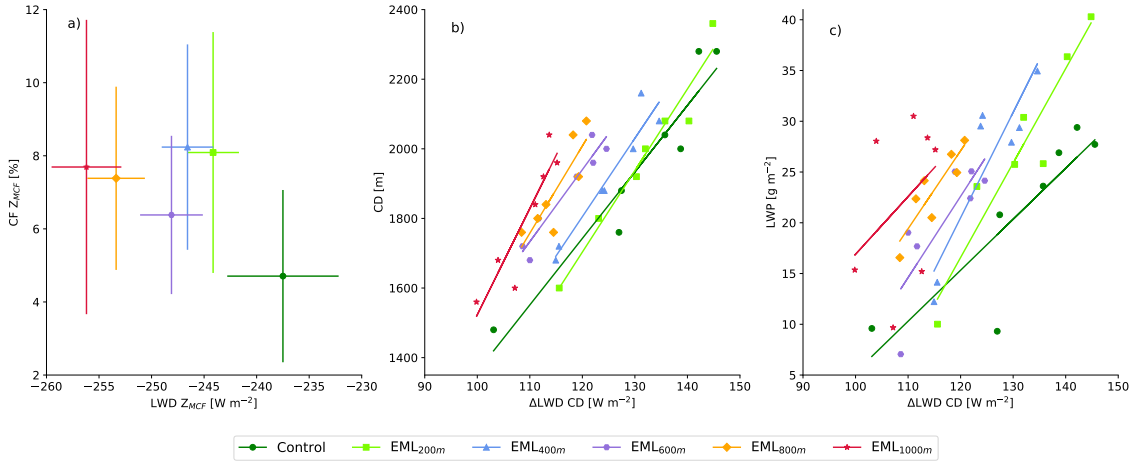

Figure 6.12: A quantitative comparison of a) the mean LWD radiative flux at the altitude of the CF peak just below the inversion (LWD Z_{MCF}) to the corresponding CF (CF Z_{MCF} where the lines represent the variation in in both variables, b) the change in LWD radiative flux over the cloud layer depth (ΔLWD CD) to the cloud layer depth (CD), and c) the ΔLWD CD to the change in mean liquid water path (LWP) in the LES domain, for the Control (green), EML$_{200m}$ (light green), EML$_{400m}$ (blue), EML$_{600m}$ (purple), EML$_{800m}$(orange), and EML$_{1000m}$ (red)

longwave radiative flux at the peak in CF below the inversion it is also important to investigate the response throughout the cloud layer to the climate perturbation. The cloud layer depth is determined by deriving the altitudes for the cloud base, the first altitude at the CF $> 10^{-2}$ %, and cloud top, the next altitude above cloud base where the CF $< 10^{-2}$ %. A scatterplot of the difference in the LWD over the cloud layer (ΔLWD CD) compared to the depth of the cloud layer (CD) for the final 6 hrs of the simulation is shown in Fig. 6.12b). There are two main results highlighted in this comparison. The first is that the CD decreases with increasing EML depth, and the second is that there is a corresponding decrease in the change in LWD radiative flux over the cloud layer.

This trend is also noted in the scatterplot of the comparison between the values of ΔLWD CD and the liquid water path (LWP) averaged across the LES domain, as shown in Fig. 6.12c). Similar to the decrease in the CD with increasing EML depth, a decrease is also noted in the average LWP. This indicates a link between the change in LWP and the decrease in the CD.

In order to quantify the impact of the EML on the change in LWD over the cloud layer the difference between the ΔLWD CD in the EML and Control simulations ($\Delta LWD_{Control-EML}$ Z_{CD}) is derived and compared to the CD in the EML simulations, as shown in Fig. 6.13. This comparison further emphasizes the decreasing CD with increasing EML. Similarly the decrease in the ΔLWD over the cloud layer with increasing EML depth is also emphasized, with the increasing values of $\Delta LWD_{Control-EML}$ with increasing EML depth.

This impact on the cloud layer depth is summarized in the schematic shown in Fig. 6.14, where the differences between the Control simulation, which does not have an EML, and the EML simulations are highlighted. In the schematic the difference in the cloud layer depth, previously seen in Fig. 6.13, can be seen where the cloud layer depth in the Control simulation is larger compared to the EML simulations. A second impact of the EML also summarized in the schematic is that of the impact on the radiative fluxes, previously seen in Fig. 6.11. The magnitude of upward and downward radiative fluxes, seen in the schematic as the green and red arrows respectively, were derived at cloud top. The increase in both

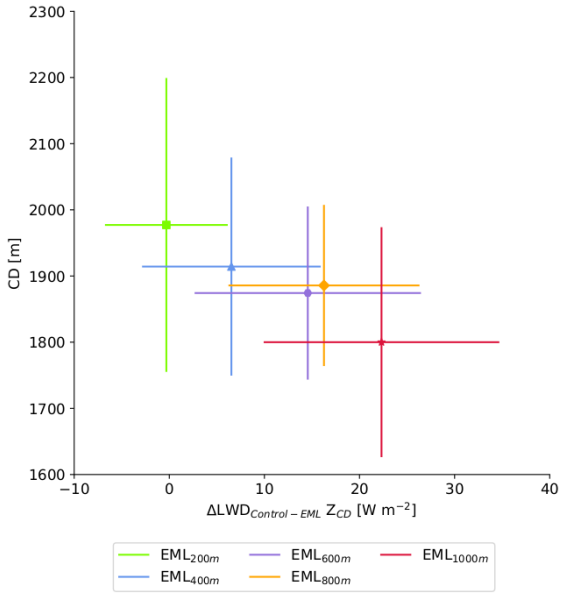

Figure 6.13: Direct comparison of the difference in the LWD over the cloud layer between the Control and EML simulations ($\Delta \mathrm{LWD}_{Control-EML}$ Z_{CD}), with respect to the cloud layer depth (CD) for the Control (green), EML 200 m (blue), EML 400 m (purple), EML 600 m (orange), EML 800 m (red), and EML 1000 m (light green).

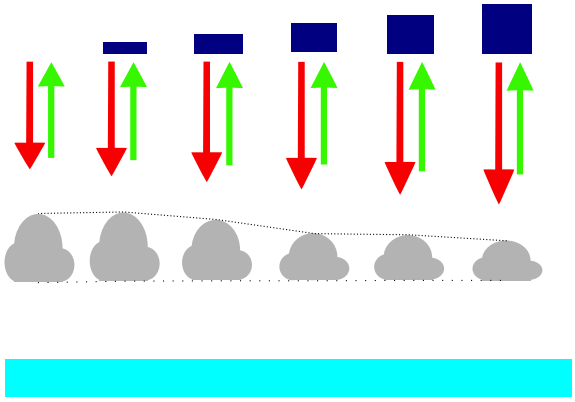

Figure 6.14: A schematic representing the increasing EML from the control to 1000 m, represented by the increasing depth of the navy blacks where Control has no EML. The resulting decrease in the depth of the cloud layer (dotted lines) and increase in the magnitude of the upward and downward radiative fluxes derived at cloud top, represented by green and red arrows respectively

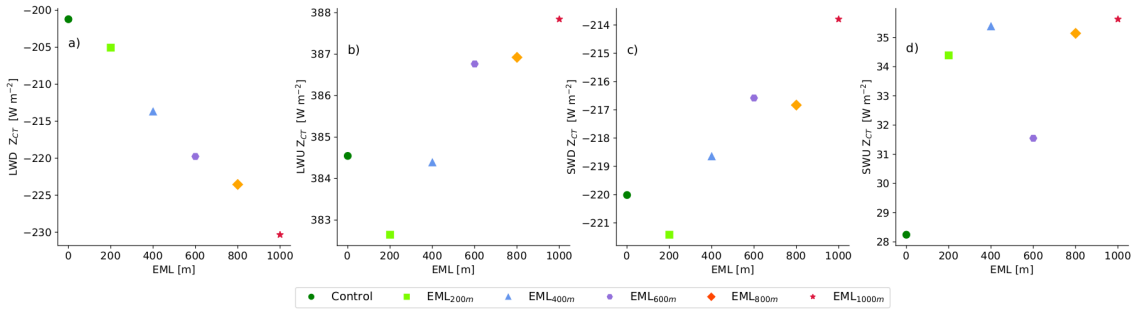

Figure 6.15: The a) LWD radiative flux, b) LWU radiative flux, c) SWD radiative flux, and d) SWU radiative flux components of the cloud radiative effect at cloud top for the Control (green), EML$_{200m}$ (light green), EML$_{400m}$ (blue), EML$_{600m}$ (purple), EML$_{800m}$ (orange), and EML$_{1000m}$ (red).

the upward and downward radiative fluxes can be seen with increasing EML depth.

6.4.5 Cloud Feedback Response to EMLs

It is evident from the previous results that the presence of an EML has a significant impact on both the radiative fluxes and the cloud layer. To quantify the response of the boundary layer clouds to a climate perturbation the total cloud radiative effect (CRE) at the top of the cloud layer is derived. The method used to derive the CRE is based on the method described in Henderson et al. (2013) and Ceppi et al. (2017), with the main difference being the altitude at which the CRE effect is calculated. In this study the CRE will be calculated at cloud top, as opposed to the top of the atmosphere. This is done in order to take the impact of the clouds into account, and reducing the effect of the absorption and reflection of radiation by the EML.

To this purpose the total CRE at the top of the cloud layer, for each simulation, needs to be taken into account. Therefore the individual components of total CRE, for each simulation, are shown in Fig. 6.15. While it is noticeable that there is an almost linear increase in the magnitude of the LWD radiative flux with increasing EML depth, there is much more variability in the other radiative components. Therefore, as it is not directly clear from these components whether the clouds would have a positive or negative cloud feedback, the total CRE needs to be calculated.

This study makes use of the CRE equation, based on E.q. 2 in Henderson et al. (2013). For this study the Control case takes the place of the clear sky conditions, while the EML conditions take the place of the all sky. This results in the equation taking the form:

$$CRE = (RAD_{up} + RAD_{down})_{EML} - (RAD_{up} + RAD_{down})_{Control} \tag{6.1}$$

where,

$$RAD_{up} = SWU + LWU \tag{6.2}$$

$$RAD_{down} = SWD + LWD \tag{6.3}$$

where RAD$_{up}$ and RAD$_{down}$ are the upward and downward components of the radiative fluxes. The CRE indicates whether the clouds produced in response to the EML have a positive or negative cloud feedback, and thus a warming or cooling effect on the boundary layer, in response to a potential future climate. When the total CRE is negative in value

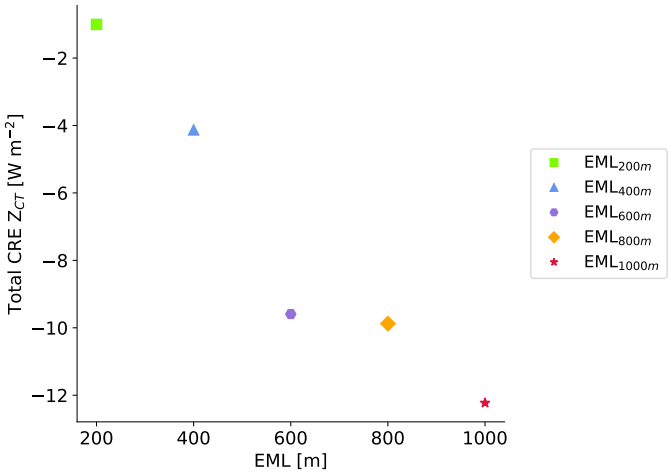

Figure 6.16: The total CRE at cloud top (CRE Z_{CT}) in EML$_{200m}$ (light green), EML$_{400m}$ (blue), EML$_{600m}$ (purple), EML$_{600m}$ (orange), and EML$_{1000m}$ (red) simulations with respect to the Control.

the boundary layer clouds have a positive cloud feedback, indicating a warming effect on the boundary layer. A positive total CRE indicates a negative cloud feedback which would mean the clouds have a cooling of the boundary layer in response to potential future climate.

The mean CRE over the last 6 hrs of the simulation are calculated for each EML simulation and is shown in Fig. 6.16. For the EML$_{200m}$ it is suggested that there will be a cooling of the atmosphere, while for the simulations with a deeper EML there is a clear shift towards a more negative CRE. This indicates that in general the boundary layer clouds produced in response to the EML simulation have a warming effect on the boundary layer, and therefore suggest that boundary layer clouds have a positive cloud feedback in response to climate change, represented by an EML.

6.5 Discussion

Over the years there have been several studies which have focused on attempting to reduce one of the largest sources of the uncertainty in climate projections, the uncertainty in how boundary layer clouds will respond to a change in climate. As GCM models continue to struggle with the representation of boundary layer clouds, due to imperfections in the parameterizations required to produce boundary layer clouds, high resolution models are suggested for testing the response of boundary layer clouds to perturbations of potential future climates. To this purpose sensitivity studies have been setup testing a variety of different climate perturbations, from increasing the concentration of CO_2 to increasing the sea surface temperature by a fixed amount. In the case of this study the response of clouds to a humidity perturbation above the boundary layer is tested.

The LES shows good ability in maintaining the presence of an EML, decoupled from the boundary layer, throughout the simulated day. The largest impacts of the EML on the boundary conditions were mainly related to the cloud fraction, with impact in Θ_l, q_t, and RF primarily seen above the boundary layer. The EML is also seen to have a significant impact on the radiative fluxes, particularly in the region between the boundary layer and the EML. Calculating the cloud radiative flux at the top of the cloud layer, allows the

impact on the cloud layer to be taken into account, while limiting the influence the EML has on the radiative effect. The results of the cloud radiative effect indicate that the boundary layer clouds, produced in response to the EML, have a positive cloud feedback and therefore a warming effect of the boundary layer.

This positive cloud feedback agrees with several recent intercomparisons where the response of boundary layer clouds to a change in climate were tested by perturbing the concentration of CO_2 or sea surface temperature (Blossey et al., 2013; Zhang et al., 2013; Bretherton and Blossey, 2014; Blossey et al., 2016). Zhang et al. (2013) gives an indication of the magnitude of the cloud feedback in single column models which appears to vary significantly across the different models. While not directly the same model type the magnitudes of the positive feedbacks in the EML simulations fall within the single column model range. These results give confidence in the potential use of EMLs as proxy cases for future climate predictions using LES models. Naturally there are a number of shortcomings associated with this study in that it is run on a relatively limited domain of 25.6 km^2 domain and therefore the larger scale impacts are not seen. This is primarily due to high computational costs for running large temporal and spatial high resolution LESs.

6.6 Conclusions

The main aim of this study was to investigate the fast response of boundary layer clouds situated under an elevated moisture layer (EML). There have been numerous studies investigating how clouds respond to changes in climate using a variety of different models and methods (e.g. Zhang et al., 2012; Myers and Norris, 2016; Nam et al., 2018). This study focuses on using large-eddy simulations generated with an EML as proxy cases for future climates where there is additional humidity above the boundary layer. As the response of the clouds to the EML is the central focus no additional modifications were made to the large-scale forcing data used to initialize the LES.

A summary of the main results are as follows:

- Large-eddy simulations were setup with an EML perturbation that was informed by an observation of an EML during the 4^{th} research flight of the first NARVAL campaign.
- Sensitivity tests were carried out on the depth of this EML, with simulations setup with EML depths of 200 m, 400 m, 600 m, 800 m, and 1000 m.
- The presence of the EML has an instantaneous impact on variables such as Θ_l, q_t, and RH above the boundary layer, with a small convective layer developing throughout the day.
- Domain averaged profiles suggest limited impact on Θ_l, q_t, and RH within the boundary layer with the largest impacts seen in the cloud fraction profiles.
- The presence of the EML has an impact on the upward and downward longwave radiative fluxes, particularly above the boundary layer, with the largest impacts in the downward longwave radiative flux in the region between the EML and boundary layer.Therefore it is indicated that the boundary layer acts as a buffer where the impact of the water vapor on the longwave radiation is reduced.
- There is a strong impact in both the upward and downward shortwave radiative fluxes in response to the EML

- At an altitude of 3500 m, between the EML and the boundary layer, EML_{1000m} has a downward longwave radiative flux that is approximately 12.5 W m^{-2} stronger compared to the Control.
- The depth of the cloud layer decreases with increasing EML depth.
- This study makes use of the total cloud radiative effect, the difference between the longwave and shortwave radiation, at the cloud top to investigate the fast response of boundary layer clouds.
- The boundary layer clouds, produced in response to the EML, have a warming effect on the boundary layer and therefore indicate that there is a positive cloud feedback in response to climate change.

Based on the results it is seen that using EMLs as a proxy for climate change in an LES reproduces a warming effect by the clouds. As this is also indicated in additional studies, using different climate change scenarios, it suggests that there is potential for using EMLs as proxy cases for climate change. There is potential in using the EMLs to test the impact with a stronger or weaker moisture perturbations, by increasing and decreasing the magnitude of the humidity perturbation using the saturated specific water content.

Chapter 7

Conclusions & Outlook

7.1 Summary of Research

Boundary layer clouds, such as stratus, stratocumulus, and cumulus clouds, play an important role in the atmosphere. While having an impact on the vertical structure, they also play an important role in the Earth's radiation budget. When the radiation budget changes there is a corresponding change in the clouds cover, referred to as the cloud feedback. With a change in climate, it is expected that the temperature and amount of moisture will increase at higher altitudes, and as a result a change in the cloud extent along with a corresponding impact on the radiation budget. It is therefore important to have an understanding as to how these clouds will respond to a change in climate.

One of the largest uncertainties in climate projections is related to the uncertainty in boundary layer cloud feedback to future climates. Therefore in recent years large-eddy simulation (LES) model have been used to set up proxy cases to investigate this feedback in response to a change in climate. These studies have usually involved including a perturbation where the CO_2 concentration is increased, or the sea surface temperature is increased by 2 to 4 K.

This study makes use of an elevated moisture layer as a proxy case for investigating the response of boundary layer clouds to a future climate. The elevated moisture layer used is based on an elevated moisture layer observed during the 4^{th} research flight of the first Next Generation-aircraft Remote-sensing (NARVAL) campaign. In order to do this the Dutch Atmospheric Large-Eddy Simulation (DALES) model is first tested against observed conditions before it generated simulations with an elevated moisture layer perturbation. Based on the results of this study an answer has been determined for the research question:

How do boundary layer clouds respond to a change in climate, using an elevated moisture layer as a proxy for a future climate.

7.2 Conclusions

In order to answer this question DALES was first compared to several observations in order to test its representativeness. Initial comparisons indicated that DALES was able to

reproduce a strong temporal development of the atmospheric boundary layer. This result is consistent with observations recorded at the Barbados Cloud Observatory. Simulations generated at the locations of the 11 dropsondes launched during the 4^{th} research flight of the first NARVAL campaign, show good ability in representing the vertical structure of the boundary layer, when compared to the dropsonde profiles. Using a probabilistic method to determine the height and strength of the inversion at the top of the boundary layer, it is indicated that DALES can capture the inversion height to a reasonable degree, however it continues to underestimate the inversion strength, particularly in the water vapor specific humidity (q_v).

Using the large-scale forcings from the simulations at the dropsonde locations, a composite case was derived to generate simulations that can be compared to the retrievals from the High Altitude and Long Range Aircraft (HALO) Microwave Package (HAMP) which was operational for the 4^{th} research flight. This allowed an investigation into how well a series of DALES simulations, with a largest domain of size 51.2 km^2, can capture the variability in integrated water vapor (σ_{IWV}) and liquid water path (σ_{LWP}) which were retrieved by HAMP. By dividing the HAMP retrievals into 27 time-windows a variety of σ_{IWV} and σ_{LWP} values were derived. Comparisons between the DALES simulations and the HAMP retrievals suggest that the LES shows a good ability in capturing σ_{IWV} and σ_{LWP} seen in the retrievals, while the smaller domain simulations have significant underestimations. There are still some underestimation in the large domain LES, where some the large σ_{IWV} and σ_{LWP} values, seen in the retrievals, cannot be represented in DALES. A correlation between the σ_{IWV}, and σ_{LWP}, and I_{org} values, in both the NARVAL simulations, confirming that there is a relation between the variability in IWV, and LWP, and the degree of organization, I_{org}. Based on the slopes of dependency between the variability and the degree of organization, it is indicated that the clouds have different structures and that the water vapor distribution controls the I_{org}. To conclude DALES is able to represent observed conditions to a high degree, both the vertical structure and the distribution of IWV and LWP, throughout the research flight studied.

Comparing the simulations against the observed conditions helped gain confidence in the LES's ability to represent the atmospheric conditions that were observed. This in turn helped gain confidence in the potential for using DALES to test how boundary layer clouds would respond to a change in climate, using an elevated moisture layer as a proxy. Using the composite simulation, built for the comparison with HAMP, a set of simulations, on a 25.6 x 25.6 km^2 grid, were generated with varying depths of the elevated moisture layer. The presence of an elevated moisture layer had an instantaneous impact on the profiles of liquid water potential temperature (Θ_l) and total water specific humidity (q_t) above the boundary layer, with limited impact within the boundary layer. The largest impact, of the elevated moisture layer, in the boundary layer was in relation to the cloud layer depth and magnitude of the cloud fraction. Aside from the impact on the vertical structure a significant impact is also found on the radiation fluxes. The largest impact on the longwave radiation occurs at altitudes above the boundary layer, while there is an impact on throughout the shortwave radiative flux profiles. To investigate the fast response of boundary layer clouds, in relation to changes in radiative flux, the cloud radiative effect at the top of the cloud layer is determined. The boundary layer clouds, produced in response to the EML, indicate a positive cloud feedback, which suggests a warming effect on the boundary layer. An increase in this warming effect on the boundary layer is seen with increasing EML depth.

Several studies have been conducted using LES models to investigate cloud responses to perturbations in CO_2 and sea surface temperature. In a number of these studies a positive cloud feedback is found in response to these perturbations. This gives confidence in the

potential use of EMLs as proxy cases for future climate simulations in LES models.

To conclude, the answer to the question about how boundary layer clouds respond to a change in climate, using an elevated moisture layer as a proxy for a future climate can now be answered. Boundary layer clouds will have a fast positive cloud feedback in response to a potential future climate, derived using elevated moisture layers.

7.3 Outlook

Based on the results of this study there is potential for further research to be conducted on the topic. Recent field campaigns, such as the second NARVAL campaign and the ongoing EUREC^{4}A campaign provide large datasets. In particular the circles flown by HALO during these campaigns is expected to assist in the measurement of divergence (Bony and Stevens, 2019), which is important for determining the boundary layer conditions. By obtaining measurements of the main prognostic variables, such as liquid water potential temperature (Θ_l), the total specific humidity (q_t), the wind speed in the u and v directions, along with the divergence, simulations generated using LES can potentially produce more accurate representations of the atmospheric conditions.

While it was seen in this study that by merging the dropsonde data into the large-scale forcings ,the representation of the vertical structure of the atmospheric boundary layer was improved. Aside from the values for divergence and additional measurements recorded, the EUREC^{4}A campaign also includes measurements from additional aircrafts and research vessels. This gives hope that the representation of observed conditions in LES models can potentially be greatly improved.

The use of elevated moisture layers as proxy cases for future climates are also a source of potential future investigation. In this study the strength of the elevated moisture layer was limited to a maximum of 50 % of the saturated specific water content. Additional studies could also focus on increasing or decreasing this elevated moisture layer strength. There is also an opportunity to test the impact of an elevated moisture layer at much higher altitudes. In the NARVAL campaign, elevated moisture layers were observed between 8 to 10 km. In this study the lower level of the elevated moisture layer was limited to 4 km, with the elevated moisture layer extending to a maximum altitude of 5 km. This was primarily to reduce computational time, but with increasing computational power it is a potential future study. Additional simulations can be generated to test the sensitivity of the boundary layer to the strength of the elevated moisture layer, and the altitude at which it occurs.

Acknowledgements

Throughout the time I have spent working on this project in Cologne, there have been several people that have supported me by helping when I had questions or simply being a good friend. Therefore, I would like to take this opportunity to thank you. Firstly, I would like to thank my supervisor Prof. Roel Neggers, who gave me the opportunity to investigate an interesting research topic, and who has always been willing to discuss ideas throughout different stages of the project. I would also like to take this opportunity to thank Prof. Susanne Crewell and Dr. Vera Schemann for their comments and suggestions as members of my Doctoral Committee.

None of this work would have been possible however without the second phase of the High Definition Cloud and Precipitation in Climate Prediction (HD(CP^2) project, funded by the German Federal Ministry of Education and Research under the project number 01LK1504C.

To the members of the InScAPE group, both past and present members, Jan, Philipp, Vera, Thirza, Sara, and Maren, I would like to thank you for all the feedback in our group meetings, for answering the numerous questions I had over the years, and for being wonderful friends. It has been such an honour to work along side you every day. I would like to thank Marek and Sabrina for the discussions on both the NARVAL and Barbados data, I know that I had several questions over the years regarding the measurements during the campaign.

I would also like to take this opportunity to thank my family, who have been so supportive of my move to Cologne and everything I have worked on over the past 3 and a half years. I would also like to thank you so much for listening whenever I randomly started talking about clouds and simulations when I was home to visit. Finally I would like to say a thank you to all my wonderful friends, both friends that I knew before moving to Cologne and to the friends that I have made here in Germany. You have all been so supportive of my work, thank you.

Bibliography

Abel, S. J. and Shipway, B. J.: A comparison of cloud-resolving model simulations of trade wind cumulus with aircraft observations taken during RICO, Quart. J. Roy. Meteor. Soc., 133, 781–794, doi:10.1002/qj.55, 2007.

Ackerman, A. S., vanZanten, M. C., Stevens, B., Savic-Jovcic, V., Bretherton, C. S., Chlond, A., Golaz, J.-C., Jiang, H., Khairoutdinov, M., Krueger, S. K., Lewellen, D. C., Lock, A., Moeng, C.-H., Nakamura, K., Petters, M. D., Snider, J. R., Weinbrecht, S., and Zulauf, M.: Large-Eddy Simulations of a Drizzling, Stratocumulus-Topped Marine Boundary Layer, Monthly Weather Review, 137, 1083–1110, doi:10.1175/2008mwr2582.1, 2009.

Albrecht, B., Ghate, V., Mohrmann, J., Wood, R., Zuidema, P., Bretherton, C., Schwartz, C., Eloranta, E., Glienke, S., Donaher, S., Sarkar, M., McGibbon, J., Nugent, A. D., Shaw, R. A., Fugal, J., Minnis, P., Paliknoda, R., Lussier, L., Jensen, J., Vivekanandan, J., Ellis, S., Tsai, P., Rilling, R., Haggerty, J., Campos, T., Stell, M., Reeves, M., Beaton, S., Allison, J., Stossmeister, G., Hall, S., and Schmidt, S.: Cloud System Evolution in the Trades (CSET): Following the Evolution of Boundary Layer Cloud Systems with the NSF–NCAR GV, Bulletin of the American Meteorological Society, 100, 93–121, doi:10.1175/bams-d-17-0180.1, 2019.

Albrecht, B. A., Betts, A. K., Schubert, W. H., and Cox, S. K.: Model of the Thermodynamic Structure of the Trade-Wind Boundary Layer: Part I. Theoretical Formulation and Sensitivity Tests, Journal of the Atmospheric Sciences, 36, 73–89, doi:10.1175/1520-0469(1979)036<0073:mottso>2.0.co;2, 1979.

Albrecht, B. A., Bretherton, C. S., Johnson, D., Scubert, W. H., and Frisch, A. S.: The Atlantic Stratocumulus Transition Experiment—ASTEX, Bulletin of the American Meteorological Society, 76, 889–904, doi:10.1175/1520-0477(1995)076<0889:taste>2.0.co;2, 1995.

American Meteorological Society: Stratus, Glossary of Meteorology, URL `http://glossary.ametsoc.org/wiki/Stratus`, cited 2020a.

American Meteorological Society: Stratocumulus, Glossary of Meteorology, URL `http://glossary.ametsoc.org/wiki/Stratus`, cited 2020b.

American Meteorological Society: Cumulus, Glossary of Meteorology, URL `http://glossary.ametsoc.org/wiki/Stratus`, cited 2020c.

Arking, A.: The Radiative Effects of Clouds and their Impact on Climate, Bulletin of the American Meteorological Society, 72, 795–813, doi:10.1175/1520-0477(1991)072<0795:treoca>2.0.co;2, 1991.

Augstein, E., Riehl, H., Ostapoff, F., and Wagner, V.: Mass and Energy Transports in an Undisturbed Atlantic Trade-Wind Flow, Monthly Weather Review, 101, 101–111, doi:10.1175/1520-0493(1973)101<0101:maetia>2.3.co;2, 1973.

Beare, R. J., Edwards, J. M., and Lapworth, A. J.: Simulation of the observed evening transition and nocturnal boundary layers: Large-eddy simulation, Quarterly Journal of the Royal Meteorological Society, 132, 81–99, doi:10.1256/qj.05.64, 2006a.

Beare, R. J., Macvean, M. K., Holtslag, A. A. M., Cuxart, J., Esau, I., Golaz, J.-C., Jimenez, M. A., Khairoutdinov, M., Kosovic, B., Lewellen, D., Lund, T. S., Lundquist, J. K., Mccabe, A., Moene, A. F., Noh, Y., Raasch, S., and Sullivan, P.: An Intercomparison of Large-Eddy Simulations of the Stable Boundary Layer, Boundary-Layer Meteorology, 118, 247–272, doi:10.1007/s10546-004-2820-6, 2006b.

Bellon, G. and Geoffroy, O.: Stratocumulus radiative effect, multiple equilibria of the well-mixed boundary layer and transition to shallow convection, Quarterly Journal of the Royal Meteorological Society, 142, 1685–1696, doi:10.1002/qj.2762, 2016.

Bellon, G. and Stevens, B.: Using the Sensitivity of Large-Eddy Simulations to Evaluate Atmospheric Boundary Layer Models, J. Atmos. Sci., 69, 1582–1601, doi:10.1175/jas-d-11-0160.1, 2012.

Betts, A. K.: A new convective adjustment scheme. Part I: Observational and theoretical basis, Quarterly Journal of the Royal Meteorological Society, 112, 677–691, doi:10.1002/qj.49711247307, 1986.

Betts, A. K. and Miller, M. J.: A new convective adjustment scheme. Part II: Single column tests using GATE wave, BOMEX, ATEX and arctic air-mass data sets, Quarterly Journal of the Royal Meteorological Society, 112, 693–709, doi:10.1002/qj.49711247308, 1986.

Blossey, P. N., Bretherton, C. S., Zhang, M., Cheng, A., Endo, S., Heus, T., Liu, Y., Lock, A. P., de Roode, S. R., and Xu, K.-M.: Marine low cloud sensitivity to an idealized climate change: The CGILS LES intercomparison, Journal of Advances in Modeling Earth Systems, 5, 234–258, doi:10.1002/jame.20025, 2013.

Blossey, P. N., Bretherton, C. S., Cheng, A., Endo, S., Heus, T., Lock, A. P., and van der Dussen, J. J.: CGILS Phase 2 LES intercomparison of response of subtropical marine low cloud regimes to CO2 quadrupling and a CMIP3 composite forcing change, Journal of Advances in Modeling Earth Systems, 8, 1714–1726, doi:10.1002/2016ms000765, 2016.

Bony, S. and Dufresne, J.-L.: Marine boundary layer clouds at the heart of tropical cloud feedback uncertainties in climate models, Geophys. Res. Lett., 32, doi:10.1029/2005gl023851, 2005.

Bony, S. and Stevens, B.: Measuring Area-Averaged Vertical Motions with Dropsondes, Journal of the Atmospheric Sciences, 76, 767–783, doi:10.1175/jas-d-18-0141.1, 2019.

Bony, S., Stevens, B., Frierson, D. M. W., Jakob, C., Kageyama, M., Pincus, R., Shepherd, T. G., Sherwood, S. C., Siebesma, A. P., Sobel, A. H., Watanabe, M., and Webb, M. J.: Clouds, circulation and climate sensitivity, Nature Geoscience, 8, 261–268, doi:10.1038/ngeo2398, 2015.

Bony, S., Stevens, B., Ament, F., Bigorre, S., Chazette, P., Crewell, S., Delanoë, J., Emanuel, K., Farrell, D., Flamant, C., Gross, S., Hirsch, L., Karstensen, J., Mayer, B., Nuijens, L., Ruppert, J. H., Sandu, I., Siebesma, P., Speich, S., Szczap, F., Totems, J., Vogel, R., Wendisch, M., and Wirth, M.: EUREC4A: A Field Campaign to Elucidate the Couplings Between Clouds, Convection and Circulation, Surveys in Geophysics, 38, 1529–1568, doi:10.1007/s10712-017-9428-0, 2017.

Bony, S., Schulz, H., Vial, J., and Stevens, B.: Sugar, Gravel, Fish and Flowers: Dependence of Mesoscale Patterns of Trade-wind Clouds on Environmental Conditions, Geophysical Research Letters, doi:10.1029/2019gl085988, 2020.

Boucher, O., Randall, D., Artaxo, P., Bretherton, C., Feingold, G., Forster, P., Kerminen, V.-M., Kondo, Y., Liao, H., Lohmann, U., Rasch, P., Satheesh, S., Sherwood, S., Stevens, B., and Zhang, X.: Clouds and Aerosols. In: Climate Change 2013: The Physical Science Basis. Contribution of Working Group I to the Fifth Assessment Report of the Intergovernmental Panel on Climate Change, Cambridge University Press, Cambridge, United Kingdom and New York, NY, USA, 2013.

Bretherton, C. S.: Insights into low-latitude cloud feedbacks from high-resolution models, Philosophical Transactions of the Royal Society A: Mathematical, Physical and Engineering Sciences, 373, 20140 415, doi:10.1098/rsta.2014.0415, 2015.

Bretherton, C. S. and Blossey, P. N.: Low cloud reduction in a greenhouse-warmed climate: Results from Lagrangian LES of a subtropical marine cloudiness transition, Journal of Advances in Modeling Earth Systems, 6, 91–114, doi:10.1002/2013ms000250, 2014.

Bretherton, C. S. and Blossey, P. N.: Understanding Mesoscale Aggregation of Shallow Cumulus Convection Using Large-Eddy Simulation, Journal of Advances in Modeling Earth Systems, 9, 2798–2821, doi:10.1002/2017ms000981, 2017.

Bretherton, C. S., Krueger, S. K., Wyant, M. C., Bechtold, P., Meijgaard, E. V., Stevens, B., and Teixeira, J.: A GCSS Boundary-Layer Cloud Model Intercomparison Study Of The First Astex Lagrangian Experiment, Boundary Layer Meteorology, 93, 341–380, doi:10.1023/a:1002005429969, 1999.

Bretherton, C. S., McCaa, J. R., and Grenier, H.: A New Parameterization for Shallow Cumulus Convection and Its Application to Marine Subtropical Cloud-Topped Boundary Layers. Part I: Description and 1D Results, Monthly Weather Review, 132, 864–882, doi:10.1175/1520-0493(2004)132<0864:anpfsc>2.0.co;2, 2004.

Bretherton, C. S., Blossey, P. N., and Khairoutdinov, M.: An Energy-Balance Analysis of Deep Convective Self-Aggregation above Uniform SST, Journal of the Atmospheric Sciences, 62, 4273–4292, doi:10.1175/jas3614.1, 2005.

Bretherton, C. S., Blossey, P. N., and Jones, C. R.: Mechanisms of marine low cloud sensitivity to idealized climate perturbations: A single-LES exploration extending the CGILS cases, Journal of Advances in Modeling Earth Systems, 5, 316–337, doi:10.1002/jame.20019, 2013.

Brown, A. R., Cederwall, R. T., Chlond, A., Duynkerke, P., Golaz, J.-C., Khairoutdinov, M., Lewellen, D. C., Lock, A. P., MacVean, M. K., Moeng, C.-H., Neggers, R. A. J., Siebesma, A. P., and Stevens, B.: Large-eddy simulation of the diurnal cycle of shallow cumulus convection over land, Quarterly Journal of the Royal Meteorological Society, 128, 1075–1093, doi:10.1256/003590002320373210, 2002.

Ceppi, P., Brient, F., Zelinka, M. D., and Hartmann, D. L.: Cloud feedback mechanisms and their representation in global climate models, Wiley Interdisciplinary Reviews: Climate Change, 8, e465, doi:10.1002/wcc.465, 2017.

Cess, R. D., Zhang, M. H., Minnis, P., Corsetti, L., Dutton, E. G., Forgan, B. W., Garber, D. P., Gates, W. L., Hack, J. J., Harrison, E. F., Jing, X., Kiehi, J. T., Long, C. N., Morcrette, J. J., Potter, G. L., Ramanathan, V., Subasilar, B., Whitlock, C. H., Young,

D. F., and Zhou, Y.: Absorption of Solar Radiation by Clouds: Observations Versus Models, Science, 267, 496–499, doi:10.1126/science.267.5197.496, 1995.

Cuijpers, J. W. M. and Duynkerke, P. G.: Large Eddy Simulation of Trade Wind Cumulus Clouds, Journal of the Atmospheric Sciences, 50, 3894–3908, doi:10.1175/1520-0469(1993)050<3894:lesotw>2.0.co;2, 1993.

Dal Gesso, S. and Neggers, R. A. J.: Can We Use Single-Column Models for Understanding the Boundary Layer Cloud-Climate Feedback?, Journal of Advances in Modeling Earth Systems, 10, 245–261, doi:10.1002/2017ms001113, 2018.

Davidson, B.: The Barbados Oceanographic and Meteorological Experiment, Bulletin of the American Meteorological Society, 49, 928–935, doi:10.1175/1520-0477-49.9.928, 1968.

Deardorff, J. W.: Theoretical expression for the countergradient vertical heat flux, Journal of Geophysical Research, 77, 5900–5904, doi:10.1029/jc077i030p05900, 1972a.

Deardorff, J. W.: Numerical Investigation of Neutral and Unstable Planetary Boundary Layers, Journal of the Atmospheric Sciences, 29, 91–115, doi:10.1175/1520-0469(1972)029<0091:nionau>2.0.co;2, 1972b.

Deardorff, J. W.: Three-dimensional numerical modeling of the planetary boundary layer in: Workshop on Meteorology (edit. Haugen, D. A.), American Meteorological Society, pp. 271–311, 1973.

Duynkerke, P. G., Jonker, P. J., Chlond, A., Zanten, M. C. V., Cuxart, J., Clark, P., Sanchez, E., Martin, G., Lenderink, G., and Teixeira, J.: Intercomparison of Three- and One-Dimensional Model Simulations and Aircraft Observations of Stratocumulus, Boundary-Layer Meteorology, 92, 453–487, doi:10.1023/a:1002006919256, 1999.

Duynkerke, P. G., de Roode, S. R., van Zanten, M. C., Calvo, J., Cuxart, J., Cheinet, S., Chlond, A., Grenier, H., Jonker, P. J., Köhler, M., Lenderink, G., Lewellen, D., Lappen, C.-L., Lock, A. P., Moeng, C.-H., Müller, F., Olmeda, D., Piriou, J.-M., Sánchez, E., and Sednev, I.: Observations and numerical simulations of the diurnal cycle of the EUROCS stratocumulus case, Quarterly Journal of the Royal Meteorological Society, 130, 3269–3296, doi:10.1256/qj.03.139, 2004.

Eastman, R., Warren, S. G., and Hahn, C. J.: Variations in Cloud Cover and Cloud Types over the Ocean from Surface Observations, 1954–2008, Journal of Climate, 24, 5914–5934, doi:10.1175/2011jcli3972.1, 2011.

EURECA: EUREC4A Overview: EUREC4A, URL `http://eurec4a.eu/index.php?id=4201#c17740`, 2020.

Fu, Q. and Liou, K. N.: On the Correlated k-Distribution Method for Radiative Transfer in Nonhomogeneous Atmospheres, Journal of the Atmospheric Sciences, 49, 2139–2156, doi:10.1175/1520-0469(1992)049<2139:otcdmf>2.0.co;2, 1992.

Fu, Q., Liou, K. N., Cribb, M. C., Charlock, T. P., and Grossman, A.: Multiple Scattering Parameterization in Thermal Infrared Radiative Transfer, Journal of the Atmospheric Sciences, 54, 2799–2812, doi:10.1175/1520-0469(1997)054<2799:mspiti>2.0.co;2, 1997.

Gentine, P., Bellon, G., and van Heerwaarden, C. C.: A Closer Look at Boundary Layer Inversion in Large-Eddy Simulations and Bulk Models: Buoyancy-Driven Case, Journal of the Atmospheric Sciences, 72, 728–749, doi:10.1175/jas-d-13-0377.1, 2015.

Gustafson, W. I., , Vogelmann, A. M., Cheng, X., Endo, S., Krishna, B., Li, Z., Toto, T., and and, H. X.: Description of the LASSO Alpha 1 Release, Tech. rep., DOE ARM Climate Research Facility. DOE/SC-ARM-TR-194, doi:10.2172/1373564, 2017.

Hahn, C. and Warren, S.: A Gridded Climatology of Clouds over Land (1971-1996) and Ocean (1954-2008) from Surface Observations Worldwide (NDP-026E)*, doi: 10.3334/CDIAC/CLI.NDP026E, 2007.

Hartmann, D. L., Ockert-Bell, M. E., and Michelsen, M. L.: The Effect of Cloud Type on Earth's Energy Balance: Global Analysis, Journal of Climate, 5, 1281–1304, doi: 10.1175/1520-0442(1992)005<1281:teocto>2.0.co;2, 1992.

Henderson, D. S., L'Ecuyer, T., Stephens, G., Partain, P., and Sekiguchi, M.: A Multisensor Perspective on the Radiative Impacts of Clouds and Aerosols, Journal of Applied Meteorology and Climatology, 52, 853–871, doi:10.1175/jamc-d-12-025.1, 2013.

Heus, T., van Heerwaarden, C. C., Jonker, H. J. J., Siebesma, A. P., Axelsen, S., van den Dries, K., Geoffroy, O., Moene, A. F., Pino, D., de Roode, S. R., and de Arellano, J. V.-G.: Formulation of the Dutch Atmospheric Large-Eddy Simulation (DALES) and overview of its applications, Geoph. Model Dev., 3, 415–444, doi:10.5194/gmd-3-415-2010, 2010.

Hock, T. F. and Franklin, J. L.: The NCAR GPS Dropwindsonde, Bulletin of the American Meteorological Society, 80, 407–420, doi:10.1175/1520-0477(1999)080<0407:tngd>2.0.co;2, 1999.

Holland, J. Z.: Preliminary Report on the BOMEX Sea-Air Interaction Program, Bulletin of the American Meteorological Society, 51, 809–820, doi:10.1175/1520-0477(1970)051<0809:protbs>2.0.co;2, 1970.

Holland, J. Z. and Rasmusson, E. M.: Measurements of the Atmospheric Mass, Energy, and Momentum Budgets Over a 500-Kilometer Square of Tropical Ocean, Monthly Weather Review, 101, 44–55, doi:10.1175/1520-0493(1973)101<0044:motame>2.3.co;2, 1973.

Hundsdorfer, W., Koren, B., vanLoon, M., and Verwer, J.: A Positive Finite-Difference Advection Scheme, Journal of Computational Physics, 117, 35–46, doi: 10.1006/jcph.1995.1042, 1995.

Jacob, M., Ament, F., Gutleben, M., Konow, H., Mech, M., Wirth, M., and Crewell, S.: Investigating the liquid water path over the tropical Atlantic with synergistic airborne measurements, Atmospheric Measurement Techniques Discussions, pp. 1–27, doi: 10.5194/amt-2019-18, 2019.

Jiang, H. and Cotton, W. R.: Large Eddy Simulation of Shallow Cumulus Convection during BOMEX: Sensitivity to Microphysics and Radiation, Journal of the Atmospheric Sciences, 57, 582–594, doi:10.1175/1520-0469(2000)057<0582:lesosc>2.0.co;2, 2000.

Johnson, R. H., Rickenbach, T. M., Rutledge, S. A., Ciesielski, P. E., and Schubert, W. H.: Trimodal Characteristics of Tropical Convection, Journal of Climate, 12, 2397–2418, doi: 10.1175/1520-0442(1999)012<2397:tcotc>2.0.co;2, 1999.

Joseph, J. H. and Cahalan, R. F.: Nearest Neighbor Spacing of Fair Weather Cumulus Clouds, Journal of Applied Meteorology, 29, 793–805, doi:10.1175/1520-0450(1990)029<0793:nnsofw>2.0.co;2, 1990.

Joseph, J. H., Wiscombe, W. J., and Weinman, J. A.: The Delta-Eddington Approximation for Radiative Flux Transfer, Journal of the Atmospheric Sciences, 33, 2452–2459, doi: 10.1175/1520-0469(1976)033<2452:tdeafr>2.0.co;2, 1976.

Khairoutdinov, M. and Kogan, Y.: A New Cloud Physics Parameterization in a Large-Eddy Simulation Model of Marine Stratocumulus, Monthly Weather Review, 128, 229–243, doi:10.1175/1520-0493(2000)128<0229:ancppi>2.0.co;2, 2000.

Klein, S. A. and Hartmann, D. L.: The Seasonal Cycle of Low Stratiform Clouds, Journal of Climate, 6, 1587–1606, doi:10.1175/1520-0442(1993)006<1587:tscols>2.0.co;2, 1993.

Klein, S. A., Hall, A., Norris, J. R., and Pincus, R.: Low-Cloud Feedbacks from Cloud-Controlling Factors: A Review, Surveys in Geophysics, 38, 1307–1329, doi: 10.1007/s10712-017-9433-3, 2017.

Klepp, C., Ament, F., Bakan, S., Hirsch, L., and Stevens, B.: NARVAL Campaign Report, 2014.

Konow, H., Jacob, M., Ament, F., Crewell, S., Ewald, F., Hagen, M., Hirsch, L., Jansen, F., Mech, M., and Stevens, B.: A unified data set of airborne cloud remote sensing using the HALO Microwave Package (HAMP), Earth System Science Data Discussions, pp. 1–21, doi:10.5194/essd-2018-116, 2018.

Kuettner, J. P. and Holland, J.: The BOMEX Project, Bulletin of the American Meteorological Society, 50, 394–403, doi:10.1175/1520-0477-50.6.394, 1969.

Lamer, K., Kollias, P., and Nuijens, L.: Observations of the variability of shallow trade wind cumulus cloudiness and mass flux, Journal of Geophysical Research: Atmospheres, 120, 6161–6178, doi:10.1002/2014jd022950, 2015.

Larson, V. E., Kotenberg, K. E., and Wood, N. B.: An Analytic Longwave Radiation Formula for Liquid Layer Clouds, Monthly Weather Review, 135, 689–699, doi: 10.1175/mwr3315.1, 2007.

Lilly, D.: The representation of small-scale turbulence in numerical simulation experiments, H. H. Goldstine, Ed., Proceedings of IBM Scientific Computing Symposium on Environmental Sciences, Yorktown Heights, New York, pp. 195–210, doi:10.5065/d62r3pmm, 1966.

Lock, A. P.: Factors influencing cloud area at the capping inversion for shallow cumulus clouds, Quarterly Journal of the Royal Meteorological Society, 135, 941–952, doi: 10.1002/qj.424, 2009.

Lohmann, U., Luond, F., and Mahrt, F.: An Introduction to Clouds from the Microscale to Climate, Cambridge Universtiy Press, 2016.

Markowski, P.: An Overview of Atmospheric Convection, in: Atmospheric Convection: Research and Operational Forecasting Aspects. CISM International Centre for Mechanical Sciences, edited by B., G. D., R., S., and F., S., vol. 475, pp. 1–6, Springer Vienna, doi:10.1007/978-3-211-69291-2_1, 2007.

Mason, B. J.: The GARP Atlantic tropical experiment, Nature, 255, 17–20, doi: 10.1038/255017a0, 1975.

Mason, P. J.: Large-eddy simulation: A critical review of the technique, Quarterly Journal of the Royal Meteorological Society, 120, 1–26, doi:10.1002/qj.49712051503, 1994.

Matheou, G., Chung, D., Nuijens, L., Stevens, B., and Teixeira, J.: On the Fidelity of Large-Eddy Simulation of Shallow Precipitating Cumulus Convection, Monthly Weather Review, 139, 2918–2939, doi:10.1175/2011mwr3599.1, 2011.

McGibbon, J. and Bretherton, C. S.: Skill of ship-following large-eddy simulations in reproducing MAGIC observations across the northeast Pacific stratocumulus to cumulus transition region, Journal of Advances in Modeling Earth Systems, 9, 810–831, doi:10.1002/2017ms000924, 2017.

Mech, M., Orlandi, E., Crewell, S., Ament, F., Hirsch, L., Hagen, M., Peters, G., and Stevens, B.: HAMP – the microwave package on the High Altitude and LOng range research aircraft (HALO), Atmospheric Measurement Techniques, 7, 4539–4553, doi:10.5194/amt-7-4539-2014, 2014.

Melchionna, S., Bauer, M., and Peters, G.: A new algorithm for the extraction of cloud parameters using multipeak analysis of cloud radar data First application and preliminary results, Meteorologische Zeitschrift, 17, 613–620, doi:10.1127/0941-2948/2008/0322, 2008.

Mitchell, D. L. and Finnegan, W.: Modification of cirrus clouds to reduce global warming, Environmental Research Letters, 4, 045 102, doi:10.1088/1748-9326/4/4/045102, 2009.

Mlawer, E. J., Taubman, S. J., Brown, P. D., Iacono, M. J., and Clough, S. A.: Radiative transfer for inhomogeneous atmospheres: RRTM, a validated correlated-k model for the longwave, Journal of Geophysical Research: Atmospheres, 102, 16 663–16 682, doi:10.1029/97jd00237, 1997.

Moeng, C.-H., Cotton, W. R., Stevens, B., Bretherton, C., Rand, H. A., Chlond, A., Khairoutdinov, M., Krueger, S., Lewellen, W. S., MacVean, M. K., Pasquier, J. R. M., Siebesma, A. P., and Sykes, R. I.: Simulation of a Stratocumulus-Topped Planetary Boundary Layer: Intercomparison among Different Numerical Codes, Bulletin of the American Meteorological Society, 77, 261–278, doi:10.1175/1520-0477(1996)077<0261:soastp>2.0.co;2, 1996.

Muller, C. J. and Held, I. M.: Detailed Investigation of the Self-Aggregation of Convection in Cloud-Resolving Simulations, Journal of the Atmospheric Sciences, 69, 2551–2565, doi:10.1175/jas-d-11-0257.1, 2012.

Myers, T. A. and Norris, J. R.: Reducing the uncertainty in subtropical cloud feedback, Geophysical Research Letters, 43, 2144–2148, doi:10.1002/2015gl067416, 2016.

Nair, U. S., Weger, R. C., Kuo, K. S., and Welch, R. M.: Clustering, randomness, and regularity in cloud fields: 5. The nature of regular cumulus cloud fields, Journal of Geophysical Research: Atmospheres, 103, 11 363–11 380, doi:10.1029/98jd00088, 1998.

Nam, C., Kühne, P., Salzmann, M., and Quaas, J.: A Prospectus for Constraining Rapid Cloud Adjustments in General Circulation Models, Journal of Advances in Modeling Earth Systems, 10, 2080–2094, doi:10.1029/2017ms001153, 2018.

Naumann, A. K. and Kiemle, C.: The vertical Structure and spatial Variability of lower tropospheric Water Vapor and Clouds in the Trades, Atmospheric Chemistry and Physics, doi:10.5194/acp-2019-1015, 2019.

Neggers, R., Stevens, B., and Neelin, J. D.: A simple equilibrium model for shallow-cumulus-topped mixed layers, Theoretical and Computational Fluid Dynamics, 20, 305–322, doi:10.1007/s00162-006-0030-1, 2006.

Neggers, R. A. J.: Attributing the behavior of low-level clouds in large-scale models to subgrid-scale parameterizations, Journal of Advances in Modeling Earth Systems, 7, 2029–2043, doi:10.1002/2015ms000503, 2015.

Neggers, R. A. J., Neelin, J. D., and Stevens, B.: Impact Mechanisms of Shallow Cumulus Convection on Tropical Climate Dynamics, Journal of Climate, 20, 2623–2642, doi:10.1175/jcli4079.1, 2007.

Neggers, R. A. J., Köhler, M., and Beljaars, A. C. M.: A Dual Mass Flux Framework for Boundary Layer Convection. Part I: Transport, Journal of the Atmospheric Sciences, 66, 1465–1487, doi:10.1175/2008jas2635.1, 2009.

Neggers, R. A. J., Siebesma, A. P., and Heus, T.: Continuous Single-Column Model Evaluation at a Permanent Meteorological Supersite, Bulletin of the American Meteorological Society, 93, 1389–1400, doi:10.1175/bams-d-11-00162.1, 2012.

Neggers, R. A. J., Ackerman, A. S., Angevine, W. M., Bazile, E., Beau, I., Blossey, P. N., Boutle, I. A., de Bruijn, C., Cheng, A., van der Dussen, J., Fletcher, J., Gesso, S. D., Jam, A., Kawai, H., Cheedela, S. K., Larson, V. E., Lefebvre, M.-P., Lock, A. P., Meyer, N. R., de Roode, S. R., de Rooy, W., Sandu, I., Xiao, H., and Xu, K.-M.: Single-Column Model Simulations of Subtropical Marine Boundary-Layer Cloud Transitions Under Weakening Inversions, Journal of Advances in Modeling Earth Systems, 9, 2385–2412, doi:10.1002/2017ms001064, 2017.

Neggers, R. A. J., Griewank, P. J., and Heus, T.: Power-Law Scaling in the Internal Variability of Cumulus Cloud Size Distributions due to Subsampling and Spatial Organization, Journal of the Atmospheric Sciences, 76, 1489–1503, doi:10.1175/jas-d-18-0194.1, 2019.

Nicholls, S. and Lemone, M. A.: The Fair Weather Boundary Layer in GATE: The Relationship of Subcloud Fluxes and Structure to the Distribution and Enhancement of Cumulus Clouds, Journal of the Atmospheric Sciences, 37, 2051–2067, doi:10.1175/1520-0469(1980)037<2051:tfwbli>2.0.co;2, 1980.

Nieuwstadt, F. T. M. and Brost, R. A.: The Decay of Convective Turbulence, Journal of the Atmospheric Sciences, 43, 532–546, doi:10.1175/1520-0469(1986)043<0532:tdoct>2.0.co;2, 1986.

Nitta, T. and Esbensen, S.: Heat and Moisture Budget Analyses Using BOMEX Data, Monthly Weather Review, 102, 17–28, doi:10.1175/1520-0493(1974)102<0017:hambau>2.0.co;2, 1974.

NOAA: Atlantic Tradewind Ocean-Atmosphere Mesoscale Interaction Campaign, URL `https://www.esrl.noaa.gov/psd/atomic/`, 2020.

Nuijens, L. and Stevens, B.: The Influence of Wind Speed on Shallow Marine Cumulus Convection, Journal of the Atmospheric Sciences, 69, 168–184, doi:10.1175/jas-d-11-02.1, 2012.

Nuijens, L., Serikov, I., Hirsch, L., Lonitz, K., and Stevens, B.: The distribution and variability of low-level cloud in the North Atlantic trades, Quarterly Journal of the Royal Meteorological Society, 140, 2364–2374, doi:10.1002/qj.2307, 2014.

Organization, W. M.: International Cloud Atlas, Vol. 1, Secretariat of the World Meteorological Organization, 1975.

Pincus, R. and Stevens, B.: Monte Carlo Spectral Integration: a Consistent Approximation for Radiative Transfer in Large Eddy Simulations, Journal of Advances in Modeling Earth Systems, 1, 1, doi:10.3894/james.2009.1.1, 2009.

Piomelli, U.: Large-eddy simulation: achievements and challenges, Progress in Aerospace Sciences, 35, 335–362, doi:10.1016/s0376-0421(98)00014-1, 1999.

Rauber, R. M., Ochs, H. T., Girolamo, L. D., Göke, S., Snodgrass, E., Stevens, B., Knight, C., Jensen, J. B., Lenschow, D. H., Rilling, R. A., Rogers, D. C., Stith, J. L., Albrecht, B. A., Zuidema, P., Blyth, A. M., Fairall, C. W., Brewer, W. A., Tucker, S., Lasher-Trapp, S. G., Mayol-Bracero, O. L., Vali, G., Geerts, B., Anderson, J. R., Baker, B. A., Lawson, R. P., Bandy, A. R., Thornton, D. C., Burnet, E., Brenguier, J.-L., Gomes, L., Brown, P. R. A., Chuang, P., Cotton, W. R., Gerber, H., Heikes, B. G., Hudson, J. G., Kollias, P., Krueger, S. K., Nuijens, L., O'Sullivan, D. W., Siebesma, A. P., and Twohy, C. H.: A Supplement to Rain in Shallow Cumulus Over the Ocean: The RICO Campaign, Bulletin of the American Meteorological Society, 88, S12–S18, doi:10.1175/bams-88-12-rauber, 2007a.

Rauber, R. M., Stevens, B., Ochs, H. T., Knight, C., Albrecht, B. A., Blyth, A. M., Fairall, C. W., Jensen, J. B., Lasher-Trapp, S. G., Mayol-Bracero, O. L., Vali, G., Anderson, J. R., Baker, B. A., Bandy, A. R., Burnet, E., Brenguier, J.-L., Brewer, W. A., Brown, P. R. A., Chuang, R., Cotton, W. R., Girolamo, L. D., Geerts, B., Gerber, H., Göke, S., Gomes, L., Heikes, B. G., Hudson, J. G., Kollias, P., Lawson, R. R., Krueger, S. K., Lenschow, D. H., Nuijens, L., O'Sullivan, D. W., Rilling, R. A., Rogers, D. C., Siebesma, A. P., Snodgrass, E., Stith, J. L., Thornton, D. C., Tucker, S., Twohy, C. H., and Zuidema, P.: Rain in Shallow Cumulus Over the Ocean: The RICO Campaign, Bulletin of the American Meteorological Society, 88, 1912–1928, doi:10.1175/bams-88-12-1912, 2007b.

Reilly, S., Gesso, S. D., and Neggers, R.: Configuring LES based on dropsonde data in sparsely sampled areas in the subtropical Atlantic, Journal of Applied Meteorology and Climatology, doi:10.1175/jamc-d-19-0013.1, 2019.

Rieck, M., Nuijens, L., and Stevens, B.: Marine Boundary Layer Cloud Feedbacks in a Constant Relative Humidity Atmosphere, Journal of the Atmospheric Sciences, 69, 2538–2550, doi:10.1175/jas-d-11-0203.1, 2012.

Rossow, W. B. and Schiffer, R. A.: Advances in Understanding Clouds from ISCCP, Bulletin of the American Meteorological Society, 80, 2261–2287, doi:10.1175/1520-0477(1999)080<2261:aiucfi>2.0.co;2, 1999.

Schalkwijk, J., Jonker, H. J. J., Siebesma, A. P., and Bosveld, F. C.: A Year-Long Large-Eddy Simulation of the Weather over Cabauw: An Overview, Monthly Weather Review, 143, 828–844, doi:10.1175/mwr-d-14-00293.1, 2015.

Schneider, S. H., Washington, W. M., and Chervin, R. M.: Cloudiness as a Climatic Feedback Mechanism: Effects on Cloud Amounts of Prescribed Global and Regional Surface Temperature Changes in the NCAR GCM, Journal of the Atmospheric Sciences, 35, 2207–2221, doi:10.1175/1520-0469(1978)035<2207:caacfm>2.0.co;2, 1978.

Schnitt, S., Orlandi, E., Mech, M., Ehrlich, A., and Crewell, S.: Characterization of Water Vapor and Clouds During the Next-Generation Aircraft Remote Sensing for Validation (NARVAL) South Studies, IEEE Journal of Selected Topics in Applied Earth Observations and Remote Sensing, 10, 3114–3124, doi:10.1109/jstars.2017.2687943, 2017.

Seifert, A. and Beheng, K. D.: A double-moment parameterization for simulating autoconversion, accretion and selfcollection, Atmospheric Research, 59-60, 265–281, doi: 10.1016/s0169-8095(01)00126-0, 2001.

Seifert, A. and Beheng, K. D.: A two-moment cloud microphysics parameterization for mixed-phase clouds. Part 1: Model description, Meteorology and Atmospheric Physics, 92, 45–66, doi:10.1007/s00703-005-0112-4, 2005.

Seifert, A. and Heus, T.: Large-eddy simulation of organized precipitating trade wind cumulus clouds, Atmospheric Chemistry and Physics, 13, 5631–5645, doi:10.5194/acp-13-5631-2013, 2013.

Siebert, H., Beals, M., Bethke, J., Bierwirth, E., Conrath, T., Dieckmann, K., Ditas, F., Ehrlich, A., Farrell, D., Hartmann, S., Izaguirre, M. A., Katzwinkel, J., Nuijens, L., Roberts, G., Schäfer, M., Shaw, R. A., Schmeissner, T., Serikov, I., Stevens, B., Stratmann, F., Wehner, B., Wendisch, M., Werner, F., and Wex, H.: The fine-scale structure of the trade wind cumuli over Barbados - an introduction to the CARRIBA project, Atmospheric Chemistry and Physics, 13, 10 061–10 077, doi:10.5194/acp-13-10061-2013, 2013.

Siebesma, A. P. and Cuijpers, J. W. M.: Evaluation of Parametric Assumptions for Shallow Cumulus Convection, Journal of the Atmospheric Sciences, 52, 650–666, doi: 10.1175/1520-0469(1995)052<0650:eopafs>2.0.co;2, 1995.

Siebesma, A. P. and Holtslag, A. A. M.: Model Impacts of Entrainment and Detrainment Rates in Shallow Cumulus Convection, Journal of the Atmospheric Sciences, 53, 2354–2364, doi:10.1175/1520-0469(1996)053<2354:mioead>2.0.co;2, 1996.

Siebesma, A. P., Bretherton, C. S., Brown, A., Chlond, A., Cuxart, J., Duynkerke, P. G., Jiang, H., Khairoutdinov, M., Lewellen, D., Moeng, C.-H., Sanchez, E., Stevens, B., and Stevens, D. E.: A Large Eddy Simulation Intercomparison Study of Shallow Cumulus Convection, Journal of the Atmospheric Sciences, 60, 1201–1219, doi:10.1175/1520-0469(2003)60<1201:alesis>2.0.co;2, 2003.

Smagorinsky, J.: General circulation experiments with the primitive equations, Monthly Weather Review, 91, 99–164, doi:10.1175/1520-0493(1963)091<0099:gcewtp>2.3.co;2, 1963.

Sommeria, G.: Three-Dimensional Simulation of Turbulent Processes in an Undisturbed Trade Wind Boundary Layer, Journal of the Atmospheric Sciences, 33, 216–241, doi: 10.1175/1520-0469(1976)033<0216:tdsotp>2.0.co;2, 1976.

Stevens, B.: On the Growth of Layers of Nonprecipitating Cumulus Convection, Journal of the Atmospheric Sciences, 64, 2916–2931, doi:10.1175/jas3983.1, 2007.

Stevens, B., Moeng, C.-H., and Sullivan, P. P.: Large-Eddy Simulations of Radiatively Driven Convection: Sensitivities to the Representation of Small Scales, Journal of the Atmospheric Sciences, 56, 3963–3984, doi:10.1175/1520-0469(1999)056<3963:lesord>2.0.co;2, 1999.

Stevens, B., Ackerman, A. S., Albrecht, B. A., Brown, A. R., Chlond, A., Cuxart, J., Duynkerke, P. G., Lewellen, D. C., Macvean, M. K., Neggers, R. A. J., Sánchez, E., Siebesma, A. P., and Stevens, D. E.: Simulations of Trade Wind Cumuli under a Strong Inversion, Journal of the Atmospheric Sciences, 58, 1870–1891, doi:10.1175/1520-0469(2001)058<1870:sotwcu>2.0.co;2, 2001.

Stevens, B., Farrell, D., Hirsch, L., Jansen, F., Nuijens, L., Serikov, I., Brügmann, B., Forde, M., Linne, H., Lonitz, K., and Prospero, J. M.: The Barbados Cloud Observatory: Anchoring Investigations of Clouds and Circulation on the Edge of the ITCZ, Bulletin of the American Meteorological Society, 97, 787–801, doi:10.1175/bams-d-14-00247.1, 2016.

Stevens, B., Ament, F., Bony, S., Crewell, S., Ewald, F., Gross, S., Hansen, A., Hirsch, L., Jacob, M., Kölling, T., Konow, H., Mayer, B., Wendisch, M., Wirth, M., Wolf, K., Bakan, S., Bauer-Pfundstein, M., Brueck, M., Delanoë, J., Ehrlich, A., Farrell, D., Forde, M., Gödde, F., Grob, H., Hagen, M., Jäkel, E., Jansen, F., Klepp, C., Klingebiel, M., Mech, M., Peters, G., Rapp, M., Wing, A. A., and Zinner, T.: A High-Altitude Long-Range Aircraft Configured as a Cloud Observatory: The NARVAL Expeditions, Bulletin of the American Meteorological Society, 100, 1061–1077, doi:10.1175/bams-d-18-0198.1, 2019a.

Stevens, B., Bony, S., Brogniez, H., Hentgen, L., Hohenegger, C., Kiemle, C., L'Ecuyer, T. S., Naumann, A. K., Schulz, H., Siebesma, P. A., Vial, J., Winker, D. M., and Zuidema, P.: Sugar, gravel, fish and flowers: Mesoscale cloud patterns in the trade winds, Quarterly Journal of the Royal Meteorological Society, 146, 141–152, doi:10.1002/qj.3662, 2019b.

Stocker, T. F. e. a. e.: Summary for Policymakers in Climate Change 2013: The Physical Science Basis, 129pp, Cambridge University Press, 2013.

Stull, R. B.: An Introduction to Boundary Layer Meteorology (Atmospheric Sciences Library), Springer, 1988.

Tan, Z., Schneider, T., Teixeira, J., and Pressel, K. G.: Large-eddy simulation of subtropical cloud-topped boundary layers: 1. A forcing framework with closed surface energy balance, J. Adv. Model. Earth Sys., 8, 1565–1585, doi:10.1002/2016ms000655, 2016.

Tan, Z., Schneider, T., Teixeira, J., and Pressel, K. G.: Large-eddy simulation of subtropical cloud-topped boundary layers: 2. Cloud response to climate change, Journal of Advances in Modeling Earth Systems, 9, 19–38, doi:10.1002/2016ms000804, 2017.

Teixeira, J., Stevens, B., Bretherton, C. S., Cederwall, R., Doyle, J. D., Golaz, J. C. ., Holtslag, A. A. M., Klein, S. A. ., Lundquist, J. K., Randall, D. A., Siebesma, A. P., and Soares, P. M. M.: Parameterization of the Atmospheric Boundary Layer: A View from Just Above the Inversion, Bulletin of the American Meteorological Society, 89, 453–458, doi:10.1175/bams-89-4-453, 2008.

Tiedtke, M., Heckley, W. A., and Slingo, J.: Tropical forecasting at ECMWF: The influence of physical parametrization on the mean structure of forecasts and analyses, Quarterly Journal of the Royal Meteorological Society, 114, 639–664, doi:10.1002/qj.49711448106, 1988.

Tompkins, A. M.: Organization of Tropical Convection in Low Vertical Wind Shears: The Role of Cold Pools, Journal of the Atmospheric Sciences, 58, 1650–1672, doi:10.1175/1520-0469(2001)058<1650:ootcil>2.0.co;2, 2001.

Tompkins, A. M. and Semie, A. G.: Organization of tropical convection in low vertical wind shears: Role of updraft entrainment, Journal of Advances in Modeling Earth Systems, 9, 1046–1068, doi:10.1002/2016ms000802, 2017.

van der Dussen, J. J., de Roode, S. R., Ackerman, A. S., Blossey, P. N., Bretherton, C. S., Kurowski, M. J., Lock, A. P., Neggers, R. A. J., Sandu, I., and Siebesma, A. P.: The GASS/EUCLIPSE model intercomparison of the stratocumulus transition as observed during ASTEX: LES results, Journal of Advances in Modeling Earth Systems, 5, 483–499, doi:10.1002/jame.20033, 2013.

van Laar, T.: Spatial patterns in shallow cumulus cloud populations over a heterogeneous surface, Ph.D. thesis, University of Cologne, Institute for Geophysics and Meteorology, 2019.

van Laar, T. W., Schemann, V., and Neggers, R. A. J.: Investigating the Diurnal Evolution of the Cloud Size Distribution of Continental Cumulus Convection Using Multiday LES, Journal of the Atmospheric Sciences, 76, 729–747, doi:10.1175/jas-d-18-0084.1, 2019.

vanZanten, M. C., Stevens, B., Nuijens, L., Siebesma, A. P., Ackerman, A. S., Burnet, F., Cheng, A., Couvreux, F., Jiang, H., Khairoutdinov, M., Kogan, Y., Lewellen, D. C., Mechem, D., Nakamura, K., Noda, A., Shipway, B. J., Slawinska, J., Wang, S., and Wyszogrodzki, A.: Controls on precipitation and cloudiness in simulations of trade-wind cumulus as observed during RICO, Journal of Advances in Modeling Earth Systems, 3, M06 001, doi:10.1029/2011ms000056, 2011.

Vial, J., Dufresne, J.-L., and Bony, S.: On the interpretation of inter-model spread in CMIP5 climate sensitivity estimates, Climate Dynamics, 41, 3339–3362, doi:10.1007/s00382-013-1725-9, 2013.

Vogel, R., Nuijens, L., and Stevens, B.: The role of precipitation and spatial organization in the response of trade-wind clouds to warming, Journal of Advances in Modeling Earth Systems, 8, 843–862, doi:10.1002/2015ms000568, 2016.

Weger, R. C., Lee, J., Zhu, T., and Welch, R. M.: Clustering, randomness and regularity in cloud fields: 1. Theoretical considerations, Journal of Geophysical Research, 97, 20 519, doi:10.1029/92jd02038, 1992.

Wing, A. A.: Self-Aggregation of Deep Convection and its Implications for Climate, Current Climate Change Reports, 5, 1–11, doi:10.1007/s40641-019-00120-3, 2019.

Wing, A. A., Emanuel, K., Holloway, C. E., and Muller, C.: Convective Self-Aggregation in Numerical Simulations: A Review, Surveys in Geophysics, 38, 1173–1197, doi:10.1007/s10712-017-9408-4, 2017.

Wood, R. and Bretherton, C. S.: Boundary Layer Depth, Entrainment, and Decoupling in the Cloud-Capped Subtropical and Tropical Marine Boundary Layer, Journal of Climate, 17, 3576–3588, doi:10.1175/1520-0442(2004)017<3576:bldead>2.0.co;2, 2004.

Wyngaard, J. C. and Brost, R. A.: Top-Down and Bottom-Up Diffusion of a Scalar in the Convective Boundary Layer, Journal of the Atmospheric Sciences, 41, 102–112, doi:10.1175/1520-0469(1984)041<0102:tdabud>2.0.co;2, 1984.

Xu, K.-M., Cheng, A., and Zhang, M.: Cloud-Resolving Simulation of Low-Cloud Feedback to an Increase in Sea Surface Temperature, Journal of the Atmospheric Sciences, 67, 730–748, doi:10.1175/2009jas3239.1, 2010.

Zelinka, M. D., Klein, S. A., and Hartmann, D. L.: Computing and Partitioning Cloud Feedbacks Using Cloud Property Histograms. Part I: Cloud Radiative Kernels, Journal of Climate, 25, 3715–3735, doi:10.1175/jcli-d-11-00248.1, 2012.

Zhang, M., Bretherton, C. S., Blossey, P. N., Bony, S., Brient, F., and Golaz, J.-C.: The CGILS experimental design to investigate low cloud feedbacks in general circulation models by using single-column and large-eddy simulation models, Journal of Advances in Modeling Earth Systems, 4, M12 001, doi:10.1029/2012ms000182, 2012.

Zhang, M., Bretherton, C. S., Blossey, P. N., Austin, P. H., Bacmeister, J. T., Bony, S., Brient, F., Cheedela, S. K., Cheng, A., Genio, A. D. D., Roode, S. R. D., Endo, S., Franklin, C. N., Golaz, J.-C., Hannay, C., Heus, T., Isotta, F. A., Dufresne, J.-L., Kang, I.-S., Kawai, H., Köhler, M., Larson, V. E., Liu, Y., Lock, A. P., Lohmann, U., Khairoutdinov, M. F., Molod, A. M., Neggers, R. A. J., Rasch, P., Sandu, I., Senkbeil, R., Siebesma, A. P., Drian, C. S.-L., Stevens, B., Suarez, M. J., Xu, K.-M., von Salzen, K., Webb, M. J., Wolf, A., and Zhao, M.: CGILS: Results from the first phase of an international project to understand the physical mechanisms of low cloud feedbacks in single column models, Journal of Advances in Modeling Earth Systems, 5, 826–842, doi:10.1002/2013ms000246, 2013.

Zhang, Y., Klein, S. A., Fan, J., Chandra, A. S., Kollias, P., Xie, S., and Tang, S.: Large-Eddy Simulation of Shallow Cumulus over Land: A Composite Case Based on ARM Long-Term Observations at Its Southern Great Plains Site, Journal of the Atmospheric Sciences, 74, 3229–3251, doi:10.1175/jas-d-16-0317.1, 2017.

Zhao, M. and Austin, P. H.: Life Cycle of Numerically Simulated Shallow Cumulus Clouds. Part I: Transport, Journal of the Atmospheric Sciences, 62, 1269–1290, doi:10.1175/jas3414.1, 2005.

Zhu, T., Lee, J., Weger, R. C., and Welch, R. M.: Clustering, randomness, and regularity in cloud fields: 2. Cumulus cloud fields, Journal of Geophysical Research, 97, 20 537, doi:10.1029/92jd02022, 1992.

Erklärung

Ich versichere, daß ich die von mir vorgelegte Dissertation selbständig angefertigt, die benutzten Quellen und Hilfsmittel vollständig angegeben und die Stellen der Arbeit – einschließlich Tabellen, Karten und Abbildungen –, die anderen Werken im Wortlaut oder dem Sinn nach entnommen sind, in jedem Einzelfall als Entlehnung kenntlich gemacht habe; daß diese Dissertation noch keiner anderen Fakultät oder Universität zur Prüfung vorgelegen hat; daß sie – abgesehen von unten angegebenen Teilpublikationen – noch nicht veröffentlicht worden ist sowie, daß ich eine solche Veröffentlichung vor Abschluß des Promotionsverfahrens nicht vornehmen werde. Die Bestimmungen dieser Promotionsordnung sind mir bekannt. Die von mir vorgelegte Dissertation ist von Prof. Dr. Roel A.J. Neggers betreut worden.

Köln, February 2021

SIGNATURE

Teilpublikationen

Reilly, S., S. Dal Gesso, and R. Neggers (2019) Configuring LES based on dropsonde data in sparsely sampled areas in the subtropical Atlantic, Journal of Applied Meteorology and Climatology, doi: 10.1175/JAMC-D-19-0013.1